Transition processes of electrons and holes in AlGaInP crystals studied by spectroscopic measurements

Yoshihiro Ishitani

1999

Transition processes of electrons and holes in AlGaInP crystals studied by spectroscopic measurements

Yoshihiro Ishitani

1999

Preface

When I was a student of Professor Fujimoto's laboratory at Department of Engineering Science of Kyoto University, I studied atomic processes in plasmas using laser induced fluorescence spectroscopy (LIFS). The experience on LIFS leads my interest to spectroscopic measurements on crystals in Central Research Laboratory of Hitachi Ltd. (HCRL). This thesis is the summary of the spectroscopic studies on AlGaInP crystals, which have been mainly carried out for five and a half years in HCRL. I am indebted to Professor Takashi Fujimoto for his sincere guidance and encouragement throughout my research life and for giving me the chance to transform the studies I have done into the form presented here.

I am also grateful to Professor Shigeo Fujita, Professor Akitomo Tachibana, Professor Ryuichi Ohtani, and Professor Kenji Kimura of Kyoto University for their valuable suggestions and advices on my thesis.

The studies presented here have started from my questions in the growth and characterization of the crystals for the research and development of red-light emitting laser diodes in HCRL. I am grateful to Shigekazu Minagawa of HCRL (now an engineering consultant of Samsung Electronics) for having introduced me to the study on III-V compounds and for the valuable suggestions and discussion, and also to Shin-ichiro Yano, the manager of my group, for the continuous encouragement throughout these studies. Thanks are also to the members of HCRL, especially, Etsuko Nomoto and Hiroshi Hamada for the friendly collaboration or stimulating discussion on the crystal growth and Toshiaki Tanaka for many fruitful suggestions in view of laser devices. Photoreflectance and photoluminescence excitation measurements were carried out at Research Center for Advanced Science and Technology of Tokyo University. I would like to express my sincere thanks to Professor Yasuhiro Shiraki and Hiroyuki Yaguchi of Tokyo University for providing me with the experimental apparatus and for giving me many advices on measurements. The time resolved photoluminescence measurement in Chap. V was conducted at Kobe University. I would like to express my sincere thanks to Professor Taneo Nishino and Takashi Kita for providing me with the measurement system and for the fruitful discussion on the AlGaInP alloys. The experimental result in Chap. IV was partly analyzed at Hiroshima University. This thesis was summarized after I had moved to Hiroshima University. I wish to acknowledge to Professor Yoshihiro Kikuchi, Professor Shiro Taki, and Associate-professor Nobuhiro Nishino of Hiroshima University for their sincere encouragement.

Finally thanks to my wife, for her continuous support throughout my busy days in research and development.

Hiroshima, 1999
Yoshihiro Ishitani

The present thesis is based on the contents of the following papers or presentations in international conferences.

Papers

I. "Temperature dependence of the band-gap energy of disordered GaInP"
Y.Ishitani, S.Minagawa, and T.Tanaka
J. Appl. Phys. 75 (10), 5326 (1994)

II. "The band lineup of AlGaInP/AlInP indirect semiconductors"
Y.Ishitani, E.Nomoto, T.Tanaka, and S.Minagawa
Inst. Phys. Conf. Ser. No 145: Chapter 3, 381 (1996), IOP publishing Ltd.
Paper presented at 22nd Int. Symp. Compound Semiconductors, Cheju Island Korea, 1995

III. "The optical process in AlInP/GaInP/AlInP quantum wells"
Y.Ishitani, S.Minagawa, T.Kita, T.Nishino, H.Yaguchi, and Y.Shiraki
J. Appl. Phys. 80 (8), 4592 (1996)

IV. "The energy band alignment of X_c, Γ_c, and Γ_v points in $(Al_{0.7}Ga_{0.3})_{0.5}In_{0.5}P/Al_xIn_{1-x}P$ heterostructures"
Y.Ishitani, E.Nomoto, T.Tanaka, and S.Minagawa
J. Appl. Phys. 81 (4), 1763 (1997)

V. "Temperature dependence of photoluminescence intensity from AlGaInP/GaInP-quantum well structures"
Y.Ishitani, S.Minagawa, H.Hamada, and T.Tanaka
J. Appl. Phys. 82 (3), 1336 (1997)

VI. "The Γ_c-Γ_v transition energies of strained $Al_xIn_{1-x}P$ alloys"
Y.Ishitani, H.Hamada, S.Minagawa, H.Yaguchi, and Y.Shiraki
Jpn. J. Appl. Phys. 36 (11), 6607 (1997)

International conferences

I. "The band lineup of AlGaInP/AlInP indirect semiconductors"
Y.Ishitani, E.Nomoto, T.Tanaka, and S.Minagawa
22nd Int. Symp. Compound Semiconductors, Cheju Island, Korea, 1995

II. "The interpretation of the temperature dependence of photoluminescence intensity for MQW structures"
Y.Ishitani, H.Hamada, E.Nomoto, T.Tanaka, and S.Minagawa
First Optoelectronics and Communications Conference, Chiba, Japan, 1996

CONTENTS

List of symbols

A_i^0: radiative recombination rate for an electron-hole pair in state i

A_i^1: rate of a carrier extinction process of an electron-hole pair in state i except for the radiative recombination

a_i: lattice constant of layer i

a_0: lattice constant of the substrate

C_{ij}: elastic stiffness; i and j denote the cartesian coordinates

D_{ij}: deformation potential of the electron-phonon interaction for intervalley scattering; i and j denote the cartesian coordinates

D_{2d}^*: Schoenflie's notation of the double space group

D_{nk}: electron-optical phonon deformation potential for the electrons with wavevector $\boldsymbol{k}$ in the band n

d: distance of the lattice faces

e: charge of an electron (1.602×10^{-19} C)

E_{cv}^{Γ}: Γ_c - Γ_v transition energy

E_{ij}: transition energy between level i and j

$E_v(T)$: shift of E_{cv}^{Γ} due to the thermal expansion of lattices from 0 K to temperature T (K)

E_u : Γ_{6c} - Γ_{8v} transition energy for an unstrained zinc blende type crystal

E_s^{hh}: Γ_{6c} - Γ_{7v} (electron - heavy hole) transition energy for the tetragonally deformed crystal

E_s^{lh}: Γ_{6c} - $\Gamma_{6v(2)}$ (electron - light hole) transition energy for the tetragonally deformed crystal

F_{ij}: rate of the transition of an electron - hole pair from state i to state j

I_{PL}: PL intensity as photon number

I_R: intensity of the reflected probing light in photoreflectance measurements

J: total angular momentum of an atom

$\boldsymbol{k}$: wavevector of an electron

k_b: Boltzman constant

L: superlattice period

L_c: bottom of the L-conduction band

M_γ: mass of the γth atom in an unit lattice

m_J: magnetic sub-quantum number of an atom with total angular momentum J

N_i: numbers of unit lattices of layer i in the crystal growth direction

n_{qi}: Bose-Einstein factor of the phonon with the wavevector $\boldsymbol{q}$ and mode i

$\boldsymbol{p}$: phonon polarization vector

$\boldsymbol{q}$: wavevector of phonons

R: optical reflectivity

$\boldsymbol{R}(l,\gamma)$: position of an atom of species γ in the unit lattice labeled l

T: crystal temperature

T_g: crystal growth temperature

$\boldsymbol{u}$ (r,γ): displacement of an atom of species γ from the equilibrium position in the unit lattice labeled l

V_a: hydrostatic deformation potential

V_b: shear deformation potential

X_c: bottom of the X-conduction band

X_{ic}: bottom of the X-conduction band characterized by X_i symmetry in the Bethe notation

$\alpha(T)$: thermal expansion coefficient at T K

α_m: misorientation angle of the surface orientation of a wafer from (100)

$\Delta a_i/a_0$: degree of the lattice mismatch of epitaxial layer i against the substrate

Δ_c: bottom of the Δ-conduction band

ΔE_c^{Γ}: band offset at the Γ_c point of a heterostructure

ΔE_v^{Γ}: band offset at the Γ_v point of a heterostructure

ΔE_c^{X}: band offset at the X_c point of a heterostructure

ΔE_{cv}^{Γ}: sum of the band offset at the Γ_c point and that of the Γ_v point at a heterostructure

ΔE_{lh}: energy difference between a light hole state and a heavy hole state

$\Delta E^{l}(\varepsilon)$: energy shift of a light hole state due to strain ε

$\Delta E^{h}(\varepsilon)$: energy shift of a heavy hole state due to strain ε

ΔE_v^{bw}: energy difference between the vertex level of the valence band of the barrier layer and the heavy hole level in a quantum well

ΔI_R: modulated component of the reflected probing light intensity in photoreflectance measurements

δn_i: density of the electron-hole pairs in state i

ΔR: modulated component of the optical reflectivity

ε: elastic strain

ε_r: real part of a dielectric function

ε_i: imaginary part of a dielectric function

ε_0: static dielectric function

ε_∞: dielectric function for the infinite frequency

Γ_c: bottom of the Γ-conduction band

Γ_{ic}: bottom of the Γ-conduction band characterized by the Γ_i symmetry in the Bethe notation

Γ_v: bottom of the Γ-valence band

Γ_{iv}: bottom of the Γ-valence band characterized by the Γ_i symmetry in the Bethe notation

Γ_{ij}: broadening parameter of the spectral line for the electron transition from level i to j

λ_o: wavelength of the incident x-ray in an x-ray diffraction measurement

θ : angle between the incident and the diffracted x-rays in an x-ray diffraction measurement

θ_{in}: incident angle of an x-ray in an x-ray diffraction measurement

θ_d: diffraction angle of an x-ray in an x-ray diffraction measurement

θ_d^0: diffraction angle of the main interference peak in an x-ray diffraction pattern

θ_m: diffraction angle of the mth satellite peak in an x-ray diffraction pattern

θ_v: Debye temperature

τ_γ: position of the γth atom in an unit lattice

Chapter I

General introduction

AlGaInP alloys are III-V compounds used as materials for visible light emitting diodes (LEDs) and laser diodes (LDs) in the visible region. The LD emitting the light in the 0.6 μm wavelength region has been developed in the 1980's on the basis of the advances in epitaxial growth techniques of organometallic vapor phase epitaxy (OMVPE) or molecular beam epitaxy (MBE),[1) 2)] which reduced the impurity level of carbon or oxygen, in particular in the compounds with aluminum.[3)] Now, LDs with the wavelength of 630 - 690 nm region and those with the output power of 35 mW at 650 - 690 nm at room temperature (RT) are commercially available.

When an AlGaInP alloy is grown by OMVPE or MBE, a natural superlattice (SL) structure or Long-Range-Ordering (LRO) usually develops.[4) - 21)] The majority of the LDs in the 660 - 690 nm range are of alloys with this structure. When LRO is absent, or the alloy is disordered, the transition energy tends to be high, which is favorable for shorter wavelength LDs. I will be concerned in this thesis with disordered alloys.

Disordered $(Al_zGa_{1-z})_xIn_{1-x}P$ ($0 \le z \le 1$, $0 \le x \le 1$) alloys have a zincblende crystal structure and various lattice constants as shown in Fig. 1.1.[22)] The alloy compositions which lattice match to a GaAs substrate is schematically illustrated with the thick solid line. $Ga_xIn_{1-x}P$ and $Al_yIn_{1-y}P$ lattices match to this substrate at $x = 0.52$ and at $y = 0.53$, respectively. These alloys are sometimes denoted as $Ga_{0.5}In_{0.5}P$ and $Al_{0.5}In_{0.5}P$ conventionally. The lattice matched quaternary alloy is $(Al_{0.53}In_{0.47}P)_z(Ga_{0.52}In_{0.48}P)_{1-z}$, which is conventionally denoted as $(Al_zGa_{1-z})_{0.5}In_{0.5}P$. Figure 1.2 shows the band structure of disordered $Ga_{0.52}In_{0.48}P$[23)] as an example, in which the Γ_{6c} point is the lowest energy level in the conduction band: the direct transition nature. $Ga_xIn_{1-x}P$ alloys with $x > 0.73$ are found to have the X_{6c} point as the lowest energy level in the conduction band at 300 K as determined from the absorption spectra: the indirect transition nature.[24)] The strain effects on the electronic transition energy has been obtained.[25)] Although the $Al_yIn_{1-y}P$ alloy has the largest band gap and Γ_{6c} - Γ_{8v} transition energy among the AlGaInP alloys with a particular lattice constant, there is only one report on the transition energies of disordered alloys.[26)] From the cathode luminescence (CL) spectra the X_{6c} energy for $y > 0.44$ is found to be lower than the Γ_{6c} energy at 300 K. The strain effects on the transition energies are not known. In Fig. 1.3 the Γ_{6c} - Γ_{8v} and X_{6c} - Γ_{8v} transition energies of AlGaInP alloys at 300 K are illustrated as a function of alloy composition.[25) - 28)]

$Ga_{0.52}In_{0.48}P$ with LRO is of the Cu-Pt type: $Ga_{0.5+\delta}In_{0.5-\delta}P$/ $Ga_{0.5-\delta}In_{0.5+\delta}P$-SLs ($0 \le \delta \le 0.5$) in the direction of $[\bar{1}\,11]$ or $[1\bar{1}1]$. The period of the lattice is found to be twice that of $Ga_{0.52}In_{0.48}P$ from the tunneling electron diffraction (TED) spots appearing at

$(\overline{1/2}\ 1/2\ 1/2)$ or $(1/2\ \overline{1/2}\ 1/2)$.[6)-9)] The model of this SL is illustrated in Fig. 1.4. LRO is also observed in other AlGaInP alloys such as $Al_{0.5}In_{0.5}P$ [10)] grown on a GaAs substrate and $Ga_{0.7}In_{0.3}P$ [11)] grown on a $GaAs_{0.61}P_{0.39}$ substrate. The band structure is affected by the SLs. The polarization in photoluminescence (PL) spectra between [1 1 0] and [1 $\bar{1}$ 0] polarization directions was observed, and was attributed to the reduction of the symmetry of the crystal. [12)] Γ_c - Γ_v transition energy (E_{cv}^{Γ}) of ordered $Ga_{0.52}In_{0.48}P$ is found to be smaller than that of the disordered alloy by 50 - 100 meV from PL or electroreflectance (ER) spectra.[4) 13)-17)] The decay time of the intensity of time resolved PL (TRPL) was measured on strongly ordered and weakly ordered $(Al_{0.5}Ga_{0.5})_{0.5}In_{0.5}P$ at 15 K.[18)] It is found that PL from the strongly ordered alloy has the direct transition nature and the weakly ordered one is of the indirect transition nature. The theoretical study showed that the presence of the Cu - Pt type SL folds the energy level of L_c point to Γ_c point ($\Gamma_c(L_c)$), and that the repulsive interaction between these levels lowers the bottom of the Γ_c point.[19)-21)] In theoretical studies the energy levels of the ordered ternary alloys are compared with the band energy alignment of the binary compounds. Although δ mentioned above is found to be about 0.17 for the ordered GaInP with E_{cv}^{Γ} of 1.882 eV at 13 K,[17)] the alignment for the disordered ternary alloys is not known.

Transition energies of electrons vary with crystal temperature. An empirical formula [29)] and a theoretical formula [30)] of E_{cv}^{Γ} have been proposed. The latter formula is based on the effects of the interaction between electrons and phonons with an apparent phonon temperature. In these studies distinction is not made between the effects of the volume-thermal expansion and the electron-phonon interaction.

The development of LDs using AlGaInP alloys continues toward a shorter wavelength, a higher output power, a higher operating temperature, and so forth. In attempts toward a shorter wavelength, alloys with a larger energy gap, quantum well (QW) structures, and short period SL structures consisting of materials with the indirect transition nature have been studied as the active layer. The LDs emitting 577 nm at 77 K are obtained using $Ga_{0.7}In_{0.3}P$ alloy as the active layer on a $GaAs_{0.61}P_{0.39}$ substrate.[31) 32)] The LDs with 615 nm emission at 293 K was obtained with a strained AlGaInP single QW on a GaAs substrate.[33)] The share of the band offset at the conduction band in the total band offset (the sum of the band offsets at the conduction and the valence bands) at the Γ point ($\Delta E_c^{\Gamma}/\Delta E_{cv}^{\Gamma}$) for the heterojunction of bulk alloys is a parameter to determine the transition energies of QW structures. Several values are reported so far: 0.44 - 0.65 for $(Al_zGa_{1-z})_{0.5}In_{0.5}P$/ $Ga_{0.5}In_{0.5}P$-heterostructures (z: 0.5 - 0.6),[34)-36)] 0.67 and 0.85 for

$(Al_{0.7}Ga_{0.3})_{0.5}In_{0.5}P$/ $Ga_xIn_{1-x}P$-heterostructures (x: 0.41 and 0.44, respectively), [37] and 0.39 [38] and 0.52 [39] for $Al_{0.5}In_{0.5}P$/ $Ga_{0.5}In_{0.5}P$-heterostructure. The disagreements may be ascribed to the different measurement methods, *e.g.*, PL measurements, [36) 38) 39)] photoluminescence excitation (PLE) measurements, [34) 37)] capacitance-voltage measurements. [35)] The value for the disordered $Al_{0.5}In_{0.5}P/Ga_{0.5}In_{0.5}P$ has yet to be obtained. Short period or disordered-period SLs consisting of AlP/GaP [40) - 42)] or AlAs/GaAs [43) 44)] are studied with respect to the band folding effects. It is found that radiative electron-hole recombination rates in these SLs are larger than those in the alloys with the indirect transition nature.

For the purpose of obtaining a higher output power and a higher operating temperature, AlInP/GaInP multi quantum barrier (MQB) in cladding layers is found to be effective for the carrier confinement in the active region. [46) 47)] In these structures the band offsets at the conduction and the valence bands at heterojunctions are the important parameters for the carrier confinement. Although $(Al_zGa_{1-z})_{0.5}In_{0.5}P$ with z around 0.7 used as a material of the cladding layer and AlInP are of the indirect transition nature, the band alignment at the X_c point is not known. Temperature dependence of the PL intensity has been studied for the multi-QW (MQW) structures consisting of alloys with the direct transition nature. [48) 49)] The decrease in the PL intensity with temperature was ascribed to the carrier leak from the QW layers. In these studies the mechanism of the leak of electrons to the X_c points in the barrier layers has not been investigated.

In chapter II I describe the OMVPE system and the measurement systems of x-ray diffraction (XRD), PL, TRPL, PLE, and photoreflectance (PR), which is a modulation-reflectance technique.

In chapter III the procedure of the sample growth is described; the control methods for layer thickness and alloy composition are explained. The growth rate and the local fluctuation of layer thickness are obtained by XRD measurements of the SLs which have the periodic structure of two kinds of layers. The uniformity of the layer thickness and the alloy composition in a wafer is demonstrated. The growth condition for disordered alloys are established on the basis of the temperature dependence of the PL peak energy or the polarization spectra of PL.

In chapter IV the temperature dependence of E_{cv}^{Γ} for disordered $Ga_xIn_{1-x}P$ (x=0.0, 0.52, 0.70, and 1.0) crystals is obtained from PR or PLE spectra in the temperature (T) range of 20 - 300 K. The obtained $E_{cv}^{\Gamma}(T)$ is fitted to a function consisting of a volume-thermal expansion term and an electron-phonon interaction term. The obtained apparent phonon temperature is in the acoustic phonon temperature range, which is lower

than the optical phonon temperature range. The contribution of single phonon coupling to the shift of E_{cv}^{Γ} is found to increase as the GaP mole fraction increases. The effect of the interaction of electrons with optical phonons is investigated for the $Ga_{0.70}In_{0.30}P$ alloy.

In chapter V PL, PLE, and PR measurements are conducted on the disordered $Al_{0.53}In_{0.47}P/Ga_{0.52}In_{0.48}P$(5.9 nm or 2.0 nm-thick) $/Al_{0.53}In_{0.47}P$-QWs in the temperature range of 11 - 300 K. The difference between the transition energy obtained from a PR spectrum and from the PL peak energy is ascribed to the local variation of the well width by about one molecular layer on the basis of the comparison of the experimental and theoretical E_{cv}^{Γ} values. From the PL peak energies for X_c - Γ_v transitions and E_{cv}^{Γ}s on the sample with 2 nm well width, the relative energy levels of the Γ_c, Γ_v, and X_c points are obtained. From the comparison of this energy alignment and the theoretical results, with the consideration of the local fluctuation of QW width, $\Delta E_c^{\Gamma}/\Delta E_{cv}^{\Gamma}$ of the bulk disordered $Al_{0.53}In_{0.47}P/Ga_{0.52}In_{0.48}P$-heterostructure is determined to be 0.73 (+0.08,-0.05).

Chapter VI is devoted to the band energy alignment for alloys with the indirect transition nature. X_c - Γ_v transition energies in $(Al_{0.71}Ga_{0.29})_{0.5}In_{0.5}P/ Al_yIn_{1-y}P$ ($0.47 \le y \le 0.61$) SLs, and $(Al_zGa_{1-z})_{0.5}In_{0.5}P$ / $Al_yIn_{1-y}P$ / $(Al_zGa_{1-z})_{0.5}In_{0.5}P$ double heterostructures (y = 0.33 to 0.39, z = 0.7 to 1.0) are obtained from PL spectra at 12 K. From the results of PL, PLE, and PR measurements the X_c - Γ_v and Γ_c - Γ_v transition energies of strained and disordered $Al_yIn_{1-y}P$ alloys are obtained. The relative energy positions of the Γ_c, Γ_v, and X_c points in bulk $Al_yIn_{1-y}P$ and $(Al_{0.71}Ga_{0.29})_{0.5}In_{0.5}P$ are derived from the $Al_yIn_{1-y}P$ X_c - $(Al_{0.71}Ga_{0.29})_{0.5}In_{0.5}P$ Γ_v transition energies. This band energy alignment shows that an $Al_yIn_{1-y}P$ layer ($0.47 \le y \le 0.61$) in $(Al_{0.71}Ga_{0.29})_{0.5}In_{0.5}P$ cladding layers of LDs serves as an effective barrier for the Γ points, not for the X_c points. The deformation potentials of $Al_{0.53}In_{0.47}P$ is shown in the appendix.

In chapter VII PL spectra of $(Al_zGa_{1-z})_{0.5}In_{0.5}P/Ga_xIn_{1-x}P/(Al_zGa_{1-z})_{0.5}In_{0.5}P$-QW structures are obtained in the temperature range of 10 - 450 K. The measurements are conducted under the condition of excitation of only the well layers and a constant carrier generation rate over the entire range of measurement temperatures. It is assumed that the carrier extinction rate is determined by the radiative recombination, the carrier leak from the well layer to the barrier or cladding layers, and a non-radiative carrier recombination process. The temperature dependence of the PL intensity is analyzed by a fit of a model function to the experimental results. The effective barrier heights obtained from the fitting agree with the energy band alignment schemes at Γ points obtained in chapter VI. The presence of the $Al_yIn_{1-y}P$ (y = 0.47,0.53, or 0.60) barrier layers located just beside the QW layer is found to be effective for the carrier confinement in the QW layers.

References

1) T.Suzuki, I.Hino, A.Gomyo, and K.Nishida, Jpn.J.Appl.Phys. 21, L731 (1092)
2) H.Asahi, Y.Kawamura, H.Nagai, and T.Ikegami, Electron. Lett. 19, 163 (1982)
3) K.Sugiura, K.Domen, M.Sugawara, M.Kondo, T.Tanaka, and N.Nakajima, J.Appl.Phys. 70, 4946 (1991)
4) T.Suzuki, A.Gomyo, S.Iijima, K.Kobayashi, S.Kawata, I.Hino, and T.Yuasa, Jpn.J.Appl.Phys. 27, 2098 (1988)
5) S.Minagawa and M.Kondow, Electron.Lett. 25, 758 (1989)
6) A.Gomyo, T.Suzuki, and S.Iijima, Phys.Rev.Lett. 60, 2645(1988)
7) A.Gomyo, T.Suzuki, and S.Iijima, J.Cryst.Growth 93, 396(1986)
8) P.Bellon, J.Chevalier, G.P.Martin, E.Dupont-Nivert, C.Thiebaut, and J.P.Andre, Appl.Phys.Lett. 52, 567 (1988)
9) S.Minagawa, M.Kondow, and H.Kakibayashi, Electron.Lett. 25, 1439 (1989)
10) M.Kondow, H.Kakibayashi, and S.Minagawa, Phys.Rev.B 40, 1159 (1989)
11) M.Kondow, H.Kakibayashi, Tanaka, and S.Minagawa, Phys.Rev.Lett 63, 884(1989)
12) A.Mascarenhas, S.Kurtz, A.Kibbler, and J.M.Olson, Phys.Rev.Lett. 63, 2108 (1989)
13) M.Kondow, S.Minagawa, Y.Inoue, T.Nishino, and Y.Hamakawa, Appl.Phys.Lett. 54, 1760 (1989)
14) M.Kondow, H.Kakibayashi, S.Minagawa, Y.Inoue, T.Nishino, and Y.Hamakawa, J.Cryst.Growth 93, 412 (1988)
15) Y.Inoue, T.Nishino, Y.Hamakawa, M.Kondow, and S.Minagawa, Optoelectronics 3, 61 (1988)
16) T.Nishino, Y.Inoue, Y.Hamakawa, M.Kondow, and S.Minagawa, Appl.Phys.Lett 53, 583 (1988)
17) T.Kanata, M.Nishimoto, H.Nakayama, and T.Nishino, Phys.Rev.B 45, 6637 (1992)
18) K.Yamashita, T.Kita, H.Nakayama, and T.Nishino, Phys.Rev.B 23, 15713 (1996)
19) S.-H. Wei and A. Zunger, Appl.Phys.Lett. 56, 662 (1990)
20) S.-H. Wei and A. Zunger, Phys.Rev.B 39, 3279 (1989)
21) M.E.Lazzouni and L.J.Sham. Appl.Phys.Lett. 63, 3253 (1993)
22) M.Neubuerger, Handbook of electronic materials vol.2, Electric properties information center, New York, 1971
23) T.Nishino, J.Cryst.Growth 98, 44 (1989)
24) R.J.Nelson and N.Holonyak,Jr., J.Phys.Chem.Solids 37 629 (1976)
25) H.Asai and K.Oe, J.Appl.Phys. 54, 2052 (1983)
26) A. Onton and R.J.Chicotka, J.Appl.Phys. 41, 4205 (1970)
27) H.Asahi, Y.Kawamura, H.Nagai, J.Appl.Phys. 53, 4928(1982)

28) M.C.Wu and C.W.Chen, J.Appl.Phys. 71, 1901 (1992)
29) Y.P.Virshni, Physica 34, 149 (1967)
30) P.B.Allen, and M.Cardona, Phys.Rev.B 27, 4760 (1983)
31) S.Minagawa, Y.Ishitani, and T.Tanaka, J.Cryst.Growth 126, 539 (1993)
32) T.Tanaka, K.Uchida, Y.Ishitani, and S.Minagawa, Appl.Phys.Lett. 66, 783 (1995)
33) T.Tanaka, H.Yanagisawa, and S.Minagawa, Electron.Lett. 30, 566 (1994)
34) C.T.H.F.Liedenbaum, A.Valster, A.L.G.J.Severens, and G.W.`tHooft, Appl. Phys. Lett. 57 2698(1990)
35) M.O.Watanabe and Y.Ohba, Appl.Phys.Lett. 50, 906 (1987)
36) T.Katsuyama, I.Yoshida, and H.Hatakoshi, Inst.Phys.Conf. No.106 Chap.3, 129 (1989)
37) M.D.Dawson and G.Duggan, Appl.Phys.Lett. 64, 892 (1994)
38) T.Hayakawa, K.Takahashi, M.Hosoda, S.Yamamoto, and T.Hijikata, Jpn.J.Appl. Phys. 27 L1553 (1988)
39) D.Patel, M.J.Hafich, G.Y.Robinson, and C.S.Mononi, Phys.Rev.B 48, 18031 (1993)
30) M.Kumagai, T.Takagahara, and E.Hanamura, Phys.Rev.B 37, 898 (1988)
41) K.Asami, H.Asahi, S.G.Kim, J.H.Kim, A.Ishida, S.Takamuku, S.Gonda, and Sg.Fujita, Appl.Phy.Lett. 62,81 (1993)
42) X.L.Wang, A.Wakahara, and A.Sasaki, Twelfth Record of Alloy Semiconductor Physics and Electronics Symposium II-3, 33 (1993)
43) K.Takahashi, T.Hayama,T.Sayama, M.Kondo, S.Yamamoto, and T.Hijikata, J.Appl.Phys. 63, 1729 (1988)
44) M.Kasu, T.Yamamoto, S.Noda, and A.Sasaki, Appl.Phys.Lett. 59, 800, (1991)
45) K.Kishino, A.Kikuchi, Y.Kaneko, and I.Nomura, Appl. Phys.Lett. 58, 1822 (1991)
46) J.Rennie, M.Okajima, M.Watanabe, and G.Hatakoshi, Electron. Lett. 28, 1950(1992)
47) K.Iga, H.Uenohara, and F.Koyama, Electronic Lett. 22 1008 (1986)
48) M. Gurioli, A. Vinattieri, M. Colocci, C. Deparis, J. Massies, G. Neu, A. Bosacchi, and S. Franchi, Phys.Rev.B 44, 3115 (1991)
49) G. Bacher, H. Schweizer, J. Kovac, A. Forchel, H. Nickel, W. Schlapp, and R. Losch, Phys.Rev.B 43, 9312 (1991)

Figure captions

Fig. 1.1 Lattice constants of AlGaInP alloys as a function of alloy composition.

Fig.1.2 Band structure of disordered $Ga_{0.5}In_{0.5}P$ crystallizing in the zincblende structure.
E_{cv}^{Γ} is denoted as E_0.

Fig. 1.3 Γ_{6c} - Γ_{8v} and X_{6c} - Γ_{8v} transition energies as functions of alloy composition at 300 K.

Fig. 1.4 Configuration of atoms in completely ordered $Ga_{0.52}In_{0.48}P$. This figure illustrates the cross section of a crystal vertical to [110].

Fig. 1.5 Band structures around the Γ point for disordered and ordered alloys.

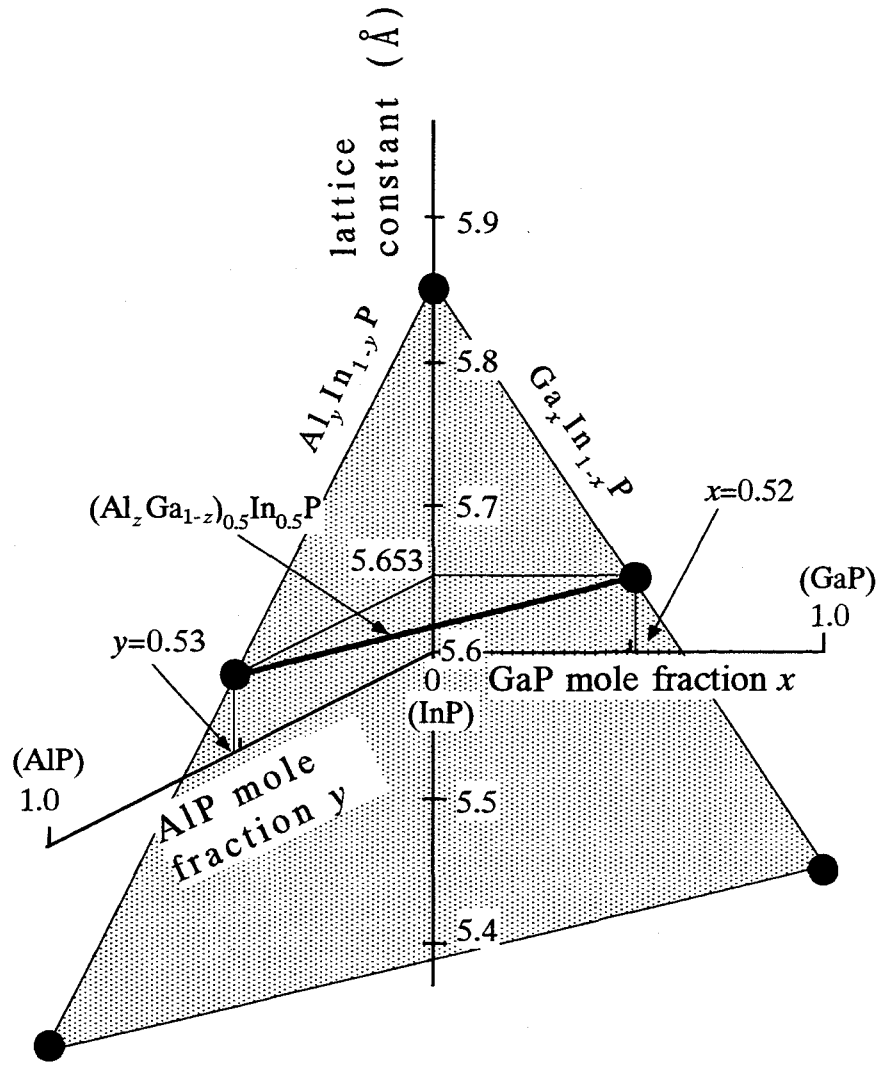
lattice constant (Å)
5.9
5.8
5.7
5.653
5.6
5.5
5.4
$Al_yIn_{1-y}P$
$Ga_xIn_{1-x}P$
$(Al_zGa_{1-z})_{0.5}In_{0.5}P$
x=0.52
y=0.53
(GaP)
1.0
0
GaP mole fraction x
(InP)
(AlP)
1.0
AlP mole fraction y

Fig. 1.1

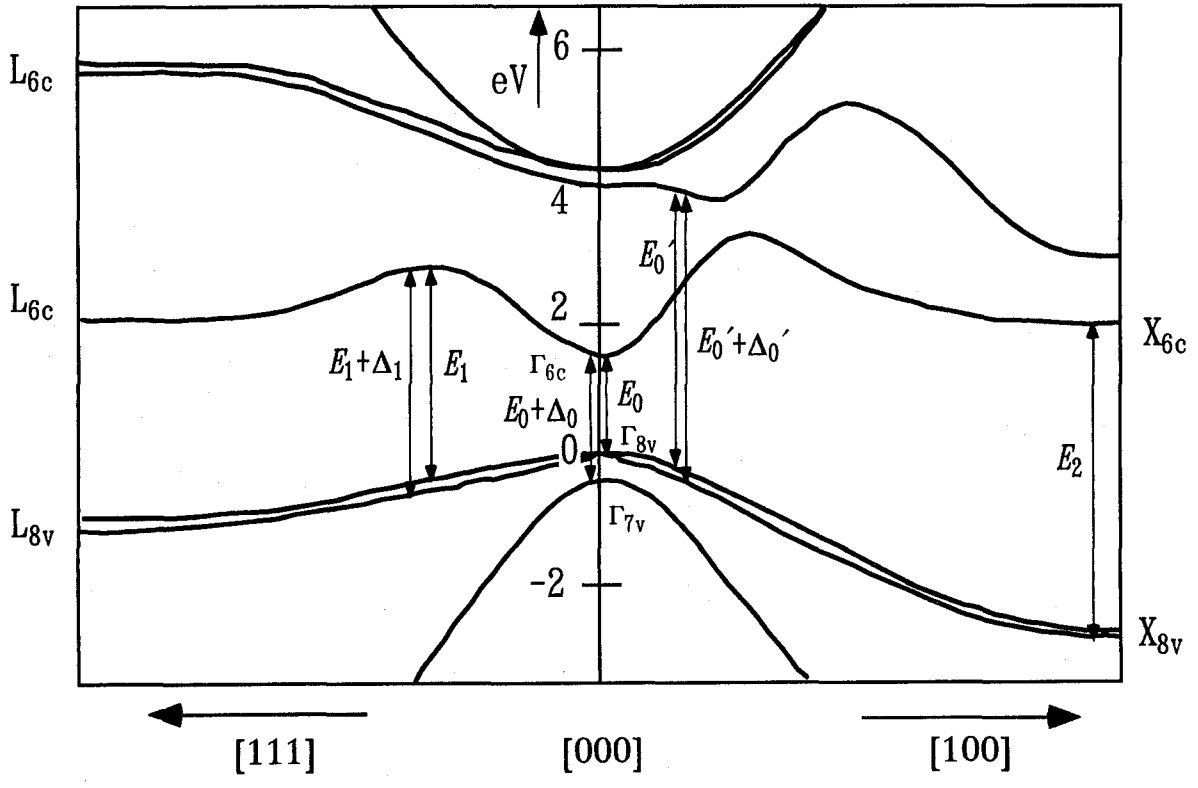
eV
6
4
2
0
-2
L_{6c}
L_{6c}
L_{8v}
X_{6c}
X_{8v}
$E_1+\Delta_1$
E_1
Γ_{6c}
$E_0+\Delta_0$
E_0
Γ_{8v}
Γ_{7v}
E_0'
$E_0'+\Delta_0'$
E_2
[111]
[000]
[100]

Fig. 1.2

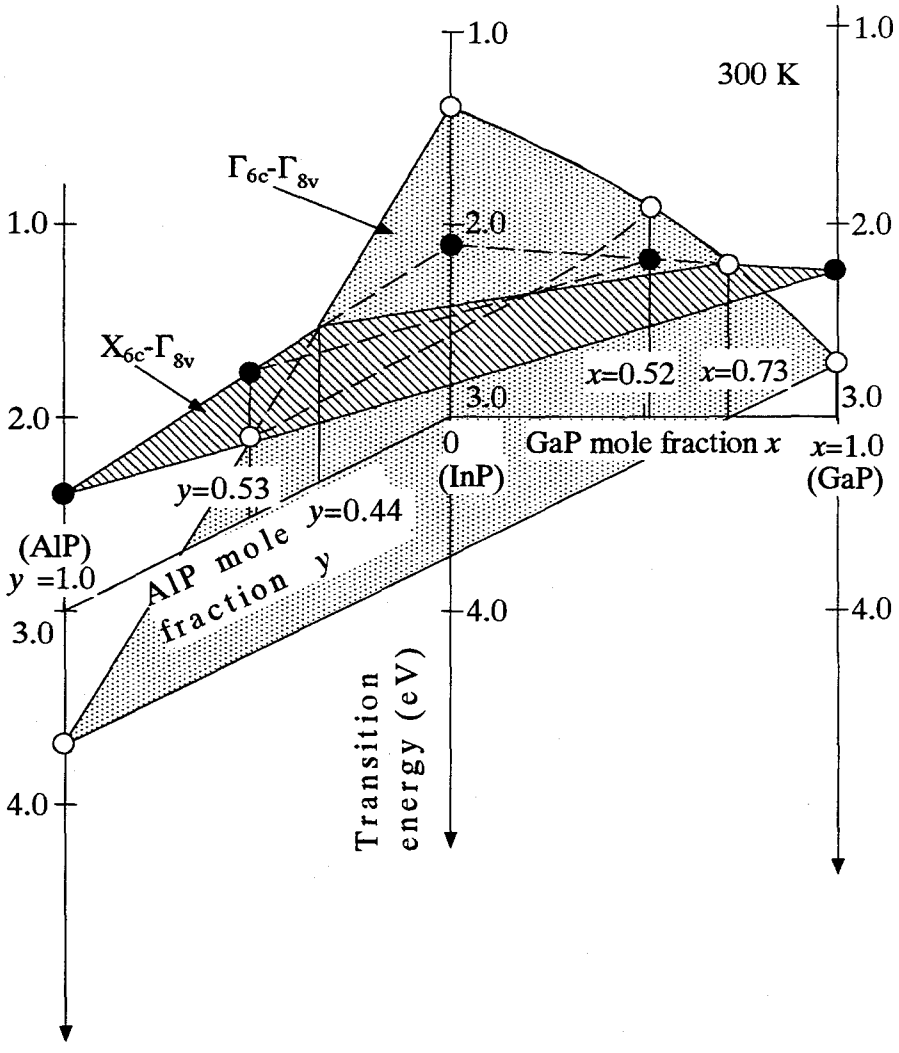
1.0
300 K
1.0
Γ_{6c}-Γ_{8v}
2.0
1.0
2.0
X_{6c}-Γ_{8v}
x=0.52
x=0.73
3.0
3.0
2.0
0
GaP mole fraction x
x=1.0
(GaP)
(InP)
y=0.53
y=0.44
(AlP)
y =1.0
AlP mole fraction y
3.0
4.0
4.0
Transition energy (eV)
4.0

Fig. 1.3

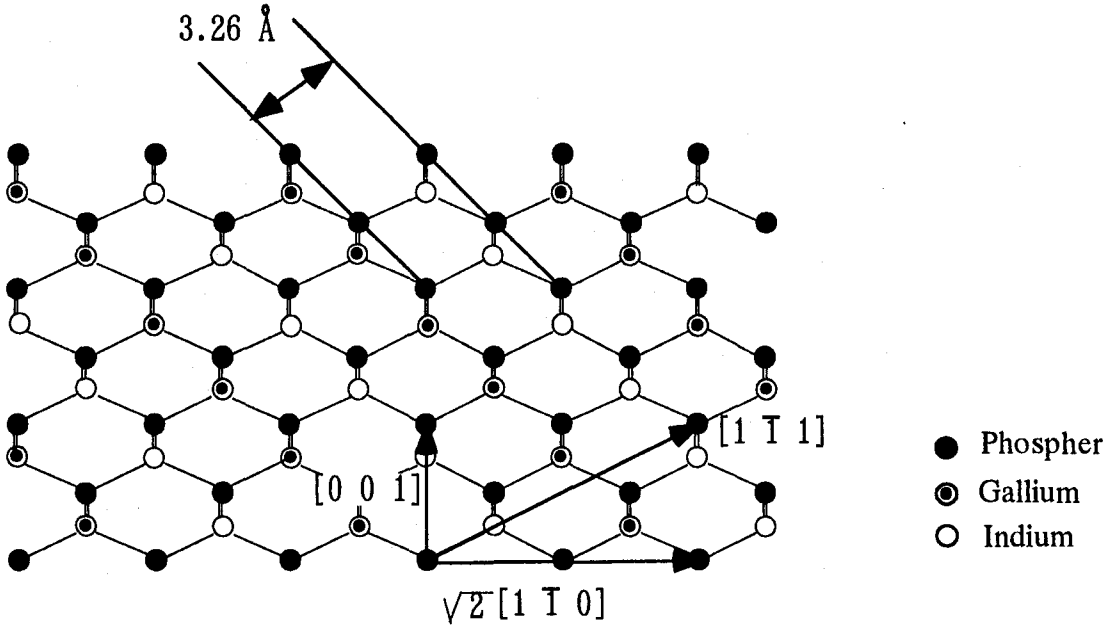

Fig. 1.4

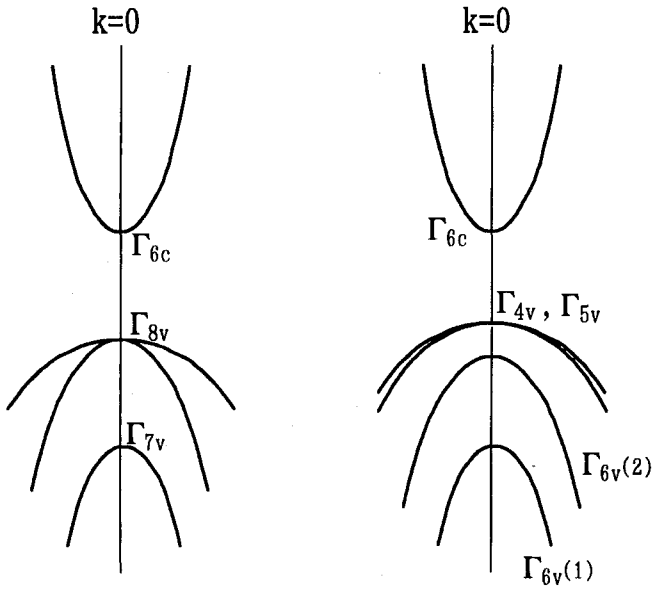

(a) disordered alloy (b) ordered alloy

Fig. 1.5

Chapter II

Experimental apparatus and technique

Abstract

The organometallic vapor phase epitaxy (OMVPE) system for crystal growth and the apparatus for characterization of crystals are described. I adjust the density of source molecules in a carrier gas supplied to a substrate and the gas flow rates to control the alloy composition and the thickness of layers. Double-crystal x-ray diffraction (XRD), photoluminescence (PL), photoluminescence excitation (PLE), and photoreflectance (PR) measurements are employed to study the alloy composition or the strain of crystals, the energy gap, and the dynamics of carriers in crystals.

2.1 Organometallic vapor phase epitaxy (OMVPE) system

The schematic diagram of the OMVPE system used for the studies described in this thesis is shown in Fig. 2.1(a). This system consists of three parts: a growth reactor block, a gas flow control block [Nipping oxygen], and a personal computer [NEC, PC9800VT]. The growth reactor block is designed by the group of Hitachi Central Research Laboratory including the present author. Figure 2.1(b) illustrates schematically the gas flow system.

In the majority of experiments, GaAs substrates [Hitachi Cable or Sumitomo Electric] are used. The Si doped n-type ($1\text{-}3\times10^{18}\,cm^{-3}$) is chosen because it is necessary to form an electric ohmic contact between the substrate and a cathode in the carrier density profiler [Biorad, Polaron EQIP PN-420] which is based on the chemical capacitance-voltage (C-V) technique. The Zn doped p-type is not used because Zn atoms easily diffuse into the epitaxial layers during the growth.[1] The surface orientation of a substrates is (100) on axis, (100) misoriented toward [011] by 7 degrees, or (511)A which is (100) misoriented toward [011] by 15.8 degrees. GaP, InP, and $GaAs_{0.61}P_{0.39}$ substrates are also used in some experiments. The objectives are explained in the chapters concerned.

The precursor of a column III element is trimethylaluminum ($(CH_3)_3Al$: TMA), trimethylgallium ($(CH_3)_3Ga$: TMG), or trimethylindium ($(CH_3)_3In$: TMI). Each of these organometallic sources is contained in a cylinder and maintained at a constant temperature in a temperature reservoir [Komatsu, DW-620A/DR-620B]: 16.0 °C for TMA, -10.0 °C for TMG, or 17.0 °C for TMI. The respective vapor pressure of these organometallic gases is 7.02 Torr, 39.3 Torr, and 1.34 Torr. [2] A carrier hydrogen gas (H_2) is bubbled in a cylinder and the mixture gas is introduced to the reactor as shown in Fig. 2.1(b). The source of a column V element is Arsine (AsH_3) or phosphine (PH_3). Zn or Si atoms are doped to layers to obtain p-type electrical conductivity or n-type one, respectively. The source of the dopant atoms is dimethylzinc (DMZ) or disilane (Si_2H_6). Arsine, phosphine, dimethylzinc, or disilane is supplied from respective gas cylinders. These gases have been diluted by hydrogen gases. The mole density of the source molecules is 20 % for Arsine, 50 % for phosphine, 500 or 1000 ppm for DMZ, or 10 ppm for disilane. Hydrogen is purified by a hydrogen purifier [Japan pionics, LS20B], and nitrogen used as a buffer gas is purified by an inert gas purifier [Japan pionics, MANN02G] before being supplied to this system.

The gas flow rates in this system are controlled by mass flow controllers (MFCs) [STEC, SEC- 4400, 4500]. The minimum flow rate we can control is 2 % of the

maximum flow rate of an MFC, which is different for different MFCs. The linearity of the flow rate and the reproducibility are ± 0.5 % and ± 0.2 %, respectively, of the maximum flow rate. The program defining a growth sequence is constructed on a personal computer and transferred to the central processing unit (CPU) in the gas flow system. The CPU controls the devices which control the gas flow such as MFCs, pneumatic valves, air pressure controller, and so forth. As shown in the subsequent section, the growth rate of a layer is determined by the product of the vapor pressure of the organometallic gas and the flow rate of the carrier gas. The ratio of the concentration of the column V source molecules to that of the column III source molecules (the V/III ratio) is larger than 200. The alloy composition of a layer is determined by the ratios of the amounts of the column III source molecules, which is verified in the subsequent section. We take the $Al_yIn_{1-y}P$ alloy as an example. Firstly, I obtain the flow rates of TMA and TMI with which the alloy is lattice matched to the GaAs substrate, i.e., $Al_{0.53}In_{0.47}P$. We denote the flow rates of TMA as $[TMA]_0$ (6.5 μmol/min) and that of TMI as $[TMI]_0$(7.5 μmol/min). When I grow the alloy $Al_yIn_{1-y}P$, the flow rate was controlled to be $y \cdot [TMA]_0 / 0.53$ for TMA and $(1-y) \cdot [TMI]_0 / 0.47$ for TMI, keeping the total concentration of the group III precursors constant. This method helped maintain a constant growth rate and control the thickness of layers. The ambiguity of alloy composition is estimated from the uncertainty of the gas flow rates controlled by MFCs for the column III sources. In this example, the uncertainty of y of $Al_yIn_{1-y}P$ is ±0.006.

Figure 2.1(c) shows the cross sectional view of the reactor. During the crystal growth, the gas pressure in the reactor is maintained at 100 torr by adjusting automatically the flow rate of the ballast N_2 gas shown in Fig. 2.1(b). The hydrogen gas containing the source molecules is introduced into the reactor through a nozzle plate; this has holes which are aligned in three concentric circles and directed slightly to the outward direction. The substrates are put on a wafer tray on a suscepter. The suscepter made of molybdenum is rotated at 50 rpm during the growth. The carbon wafer tray is coated with SiC. The tray and the suscepter are heated in the range of 600 °C - 790 °C by an ohmic heaters located under the suscepter. The power supplied to the heaters is controlled to keep the temperature which is monitored by a Pt-PtRh thermocouple just under the suscepter. The temperature at the surface of the wafer tray is monitored by pyrometers [Chino, IR-FBS and IR-FBQ]. The model IR-FBS uses the wavelength at 2.0 μm, and the model IR-FBQ uses two wavelengths at 0.85 and 1.0 μm. The pyrometer IR-FBS was calibrated by the melting point of aluminum (660 °C). At this temperature, the apparent temperature given by IR-FBS was 705 (± 5) °C.

The toxic ingredients in the waste gas is absorbed in a scrubber. The hydrogen or (and) the Arsine density in atmosphere is monitored for the purpose of safety in the gas cylinder cabinet, in the organo-metal cylinder cabinet, in the reactor housing, and on the ceiling of the laboratory.

2.2 Characterization of crystals

2.2.1 Growth rate and alloy composition

The thickness of a layer can be determined from the cross-sectional image taken by the scanning electron microscope (SEM) [Hitachi, X-6580] for layers thicker than 100 nm, or the transmission electron microscope (TEM) [Hitachi, H-900 UHR] for thinner layers. From the thickness and the growth time we may derive the growth rate of the layer. We may adopt an alternative method to obtain the growth rates of thinner layers: a plot of the superlattice (SL) period as a function of growth time of one period. The period of the SL is determined from the diffraction angles of satellite peaks in the x-ray diffraction (XRD) pattern taken by a double-crystal diffractometer [Rigaku]. This method also enables us to derive the alloy composition, because the position of the satellite peaks are also affected by the strain of the consisting layers. In this thesis, the XRD measurement is mainly employed to determine the layer thickness and the alloy composition.

The geometric configuration of the XRD system is illustrated in Fig. 2.2. The Cu x-ray source [Toshiba, A25-Cu] is operated with a tube current of 2 mA or 2.5 mA, a voltage of 20 kV or 25 kV. The x-rays are diffracted by the 1st crystal (GaAs) and the Cu $K\alpha_1$ (1.54 Å) is selected by the slit (B). This x-ray is incident on the 2nd crystal (sample). A region of approximately 1 × 10 mm is illuminated. The sample is rotated by a goniometer with a stepping motor at a rate of 128 s/min counterclockwise. The resolution of the rotation angle (diffraction angle) is ±1 s. The diffracted x-ray is registered by a scintillation counter [Rigaku, SC-10] which consists of a NaI scintillator and a photomultiplier [Hamamatsu, R268]. The relation between the diffraction angle of the interference peak (θ_d^0) and the spacing between the lattice faces (d) is expressed as

$$2d \sin \theta_d^0 = n \lambda_0, \qquad (2\text{–}1)$$

where λ_0 and n are the wavelength of the x-ray and the order number, respectively. In

the (400) diffraction, the angle θ (= 2 θ_d^0) in Fig. 2.2 is 66° for GaAs substrates, 67° for $GaAs_{0.61}P_{0.39}$ substrates, and 69° for GaP substrates for n = 1. The precision of θ is ±0.5 degree. During the measurement θ is kept constant. In order to eliminate the effect of the uncertainty of the angle θ on the measured lattice constant of the epitaxial layer, the difference between the diffraction angle of the interference peak for the substrate and that for the epitaxial layer is used. The range of observable angle θ_d determined by the slit width of the scintillation counter is 5 degree. In a measurement the geometrical configuration of the sample (the inclination angle and the position in the horizontal plane) is adjusted so that we obtain the maximum peak intensity of the (400) diffraction by the substrate.

An illustration of a periodic structure of an SL consisting of two kinds of alloys is shown in Fig. 2.3(a). Figure 2.3(b) is an example of the diffraction patterns of SLs. This is for the $Al_{0.53}In_{0.47}P/(Al_{0.71}Ga_{0.29})_{0.5}In_{0.5}P$-SL. The following equation gives the relation between the diffraction angles of the satellite peaks and the period (L) of an SL using the Bragg reflection principle.

$$L = \frac{(m-n)\lambda_0}{2(\sin\theta_m - \sin\theta_n)} . \qquad (2\text{-}2)$$

Here, θ_m and θ_n are the diffraction angles of the mth and nth satellite peaks, respectively. From the peak positions of the 0th and ±1st satellite peaks, the SL period of the example is found to be 30.9 nm. The alloy composition of a consisting layer is obtained from the SL period and the 0th satellite peak position, which gives the lattice mismatch of the SL averaged over the observed region to the GaAs substrate. [3) 4)] The results for my samples are shown in the next chapter.

2.2.2 Optical properties

The block diagram of the photoluminescence (PL) measurement system is depicted in Fig. 2.4. Electrons in the valence band is excited to the conduction band by the 476.5 nm or 514.5 nm line of an Ar^+ laser [NEC, GLG3200], the 325.4 nm line of a He - Cd laser [KIMMON, CD1252A], or the 632.8 nm line of a He-Ne laser [NEC, GLS5370]. These lasers are operated in a CW mode and the light is chopped at 280 - 300 Hz. The pulse duration is about 1.5 ms, which is long enough for the optical transition to be stationary: The time scale of the transient phenomena in an AlGaInP alloy is shorter than tens of μs. [5) 6)] The diameter of the beam spot on a sample is about 600 μm at the wavelength of 514.5 nm. The excitation power density is monitored by a photo-

detector [OPHIR, PD2-A]. The power density is adjusted by a stack of neutral density filters to the range of 10 mW/cm^2 - 5 W/cm^2. A lens made of fused quartz is used to focus the luminescence from the sample on the entrance slit of the monochromator of the focal length of 50 cm [JASCO, CT-50GD]. The linear reciprocal dispersion of the monochromator is 1.3 nm/mm at the blaze wavelength of 750 nm with the grating of 1200 grooves/mm or 2.8 nm/mm at the blaze wavelength of 1250 nm with the grating of 600 grooves/mm. The light intensity was measured in the wavelength range shorter than 900 nm by a photomultiplier biased at -700 V [Hamamatsu, R636] and for longer wavelength by a PbS detector biased at -50 V[Hamamatsu, P1026], and lock-in detected [PAR, Type D]. The wavelength is scanned by using a stepping motor with the wavelength step of 0.025 nm with a scanning rate of 30 or 60 nm/min. The signal is detected every 0.1 or 0.2 nm with a time constant of the lock-in amplifier of 0.1 or 0.3 s. The operation of the motor controller and recording of signals are controlled by a personal computer. Repeated scans over the PL spectrum of a sample at 20 K indicate reproducibility of the wavelength in the scan better than 0.1 nm. The nominal wavelength given by the reading of the spectrometer is checked by using the 632.8 nm of the He-Ne laser and the 476.5 nm of the Ar^+ ion laser. For both the wavelengths, the nominal wavelength is found longer than the actual one by 0.9 nm. The relative spectral sensitivity of the detection system was calibrated using a standard lamp [Ushio, JPD-100-500CS], which was operated at 98 V and 5.05 A; the flux of the light was reduced by using a diffuser in front of the focusing lens, and the light was incident on the entrance slit of the monochromator. Figure 2.5(a) and (b) shows the result in the visible and infrared region, respectively. For the detection system using the photomultiplier and the grating of 1200 grooves/mm, the sensitivity ratio for the polarization directions was obtained using a halogen lamp [Phillips, FCR A1/215] and a linear polarizer in the wavelength range of 540 - 720 nm. On the assumption that the light from the lamp is unpolarized, the intensities of polarized component in the parallel direction ($I_{//}$) and that in the perpendicular direction ($I_{\perp}$) to the grating ruling were observed. Figure 2.5(c) shows the result. The sample temperature is controlled in a He cryostat system [Iwatani, D105] in the range of 11 - 300 K. The illustration of the sample holder in the cryostat is shown in Fig. 2.4(b). The temperature is monitored on the wafer holder plate as shown in Fig. 2.4(b) using an FeAu-Cr thermocouple and a digital multimeter [Takeda-riken, TR6843]. The difference between the temperature of the sample and that at the contact point was found to be to within ± 2 K by the following method: The photoluminescence (PL) peak energy of an $(Al_{0.56}Ga_{0.44})_{0.5}In_{0.5}P$/ $Ga_{0.37}In_{0.63}P$/ $(Al_{0.56}Ga_{0.44})_{0.5}In_{0.5}P$ quantum well sample immersed in liquid nitrogen (1.8834 (±0.0004) eV) was compared with that

of the sample in the cryostat at the nominal temperature of 77 K (1.8833 (±0.0004) eV). These two values agree with each other within the spectral resolution of ±0.4 meV, which is due to the slit width of 0.1 mm. Since the slope dE_{cv}^{Γ}/dT (E_{cv}^{Γ} is the Γ_c-Γ_v transition energy) is 0.2 meV/K around 77 K (see Chap. IV and V), the spectral resolution corresponds to the temperature uncertainty of ± 2 K. To obtain temperatures higher than 300 K, a brass wafer holder is heated by an ohmic heater and the temperature is monitored on the surface of the holder in the vicinity of the sample by using a Cu-CuNi thermocouple.

The block diagram of the time resolved PL (TRPL) measurement system is shown in Figs. 2.6. The sample is cooled in a cryostat [Iwatani, CRT 006-2140]. The temperature of the sample is estimated using an FeAu-Cr thermocouple. The 488.0 nm light of an Ar^+ laser [NEC, GLG3070] is led to an acousto-optic modulator (AOM) [Hoya-Schott, A-161-488] operated by a pulse generator [Iwatsu, PG-230] to produce pulsed laser light with the width of 30 ns and the frequency of 2.5 kHz. The power of the laser light is 350 nJ cm^{-2}/ pulse. The luminescence is focused on the entrance slit of a monochromator [Spex, 270M] with the focal length of 27 cm. The linear reciprocal dispersion of the monochromator is 3.1 nm at the blaze wavelength of 500 nm with the grating of 1200 grooves/mm. The temporal development of PL is monitored by a photomultiplier [Hamamatsu, R329P] with the applied voltage of 1 kV and a photon-counter [Stanford Research, SR 400]. The PL observation is triggered by the signal from the pulse generator.

The experimental set up of the photoluminescence excitation (PLE) measurement is shown in Fig. 2.7. A sample is excited by a beam from a halogen lamp [Phillips JC24V-300W] through a monochromator [JASCO, CT-50C]. The linear reciprocal dispersion of the monochromator is 1.5 nm/mm at the blaze wavelength of 500 nm with the grating of 1200 grooves/mm. The automatic scanning of the wavelength is performed by a stepping motor with a step in the range of 0.1 - 0.5 nm. When the power applied to the halogen lamp is 240 W, the power density of the excitation light is 400 μW/cm^2 at 633 nm with the entrance and exit slit widths of 1.0 mm, which is monitored by a photodetector [Coherent, Labmaster-Ultima]. The relative intensity of the excitation beam observed by the photodetector is shown in Fig. 2.8. The pumping beam chopped at 300 Hz is incident on a sample with the beam shape of an approximately 1 × 5mm rectangle. I obtained this spot shape by adjusting the position of the focusing lens made of fused quartz. The luminescence is observed by a monochromator [Ritsu Oyo Kogaku, MC-25N] and a photomultiplier [Hamamatsu, R636], which is biased at -980 V. The reciprocal dispersion of the monochromator for the detection is 2.9 nm/mm at the

wavelength of 500 nm with the grating of 1200 grooves/mm. The signal is detected at an observation wavelength by a lock-in amplifier [Stanford Research, SR-530] with a time constant in the range of 0.1 - 1.0 s at the time 0.3 - 3.0 s after each wavelength scanning step of the excitation beam. The precision of the nominal wavelength of MC-25N is checked by using the 632.8 nm line of a He-Ne laser with the slit width of 0.05mm. The nominal wavelength is longer by 0.2 nm. The precision of the monochromator for the pumping beam (CT - 50C) is checked using the monochromator for the detection. The nominal wavelength and the slit width of the CT-50C are fixed at 632.8 nm and 0.5 mm, respectively, and the output of the monochromatic beam from the halogen lamp was incident on the entrance slit (0.1 mm) of the MC-25N. It was found that the nominal wavelength of the CT-50C agrees with 632.8 nm within the spectral resolution of ± 0.3 nm. Sample temperature is controlled in a He cryostat [Daikin, V202C5L] and monitored by an FeAu-Cr thermocouple in the range of 15 - 300 K. The difference between the temperature of a sample in the cryostat and that at the contact point was found to be to within ± 4 K by the same method as that for the temperature measurement in the cryostat Iwatani-D105. The difference between the sample temperature adjusted by the cryostat of Iwatani-D105 and that adjusted by the cryostat of Daikin-V202C5 with the same contact point temperature of 300 K was obtained by comparing the PL peak energy of the AlGaInP/$Ga_{0.37}In_{0.63}P$/AlGaInP quantum well structure. The obtained PL peak energy is 1.8065 (±0.0002) eV for the cryostat D105 and 1.8074 (±0.0007) eV for V202C5. Since the slope dE_{cv}^{Γ}/dT is 0.5 meV/K at around 300K (see Chap. IV), it is concluded that the disagreement is within 2 K.

The block diagram of the photoreflectance (PR) measurement system is shown in Fig. 2.9. The sample temperature is adjusted by the same system as that for the PLE measurement. The 325.4 nm line of a He-Cd laser [Ushio PCHN-U40RA] is used as a pumping beam, which is chopped at 280 - 300 Hz. The power density is equal to or less than 20 mW/cm^2. The light from the halogen lamp [Phillips JC24V-300W] through the monochromator is used as a probing beam. The monochromator is the same as that for the pumping beam in the PLE measurements. The probing beam is incident on a sample through two lenses made of fused quartz. The intensity is less than 200 μW/cm^2, which is monitored by the photodetector [Coherent, Labmaster-Ultima]. The size of the pumping beam and that of the probing beam on a sample are set almost the same; i.e., approximately 1 × 5mm rectangular shape, by the adjustment of the position of the lens located in front of the sample for the probing beam and by using a slit located on the optical path of the pumping beam. The intensity of the reflected probing light (I_R) is monitored by the photomultiplier [Hamamatsu, R636] (biased at -350 V through -500 V)

and a multimeter [Keithley, 196 System DMM]. The intensity of the modulated component (ΔI_R) is usually less than 1 % and is lock-in detected [Stanford Research, SR-530] at the time 1.0 - 6.0 s after one wavelength scanning step of 0.5 nm. The time constant of the lock-in amplifier is 0.1 - 3.0 s. Finally, $\Delta I_R/I_R$ is computed.

References

1) K.Domen, M.Kondo, and T.Tanahashi, Inst.Phys.Conf.Ser.No.129, 447, IOP publishing Ltd. (1992)
2) H.Nagai, S.Adachi, T.Hukui, III-V comnpound Crystals, Corona Publishing Co., Ltd. Tokyo, 1988
3) Armin Segmuller, P. Krishna and L.Esaki J.Appl.Cryst. 10, 1 (1977)
4) Woo-Young Choi, and Clifton G.Fonstad, Appl.Phys.Lett. 62 2815 (1993)
5) P.Michler, A.Hangleiter, M.Moser, M.Geiger, and F.Scholz, Phys.Rev.B 46 7280 (1992)
6) H. Lee, M.V.Kein, L.P.Fu and G.D.Gilliand, H.P.Hjalmarson, D.E.Aspnes, K.C.Hsieh, J.Kim, J.G.Yu, and M.G.Craford, Phys.Rev. 51 4186 (1995)

Figure captions

Fig. 2.1 Schematic diagram of the OMVPE system.
(a) Block diagram of whole the system.
(b) Schematic drawing of the gas flow system.
(c)Cross sectional view of the reactor.

Fig. 2.2. Schematic diagram of the double crystal x-ray diffractometer. Inset: configuration of the sample holder for spatial and angular adjustment.

Fig. 2.3 (a) Schematic diagram depicting an idealized superlattice consisting of the periodic structure of two kinds of layers.
(b) XRD pattern of an $Al_{0.57}In_{0.43}P$ /$(Al_{0.71}Ga_{0.29})_{0.5}In_{0.5}P$-SL on an (100) on axis substrate. The growth time of $Al_{0.57}In_{0.43}P$ and $(Al_{0.71}Ga_{0.29})_{0.5}In_{0.5}P$ are 20 s and 40 s, respectively. The growth temperature is 710°C. The measurement is conducted at room temperature.

Fig. 2.4 Schematic representation of the PL measurement system.
(a) Block diagram of the instruments for the measurement.
M: mirror, CP: chopper, L: lens, PC: personal computer, NF: neutral density filter, POL: polarizer, GT:Glan-Thompson prism.
(b) Illustration of the sample holder of the cryostat. TC: the contact point of the thermocouple.

Fig. 2.5 Sensitivity of the PL detection systems.
(a) Using the photomultiplier in the 400-1200 nm range.
(b) Using the PbS detector in the 720-1200 nm range.
(c) Sensitivity ratio for the polarization directions in the 520 - 720 nm range.

Fig. 2.6 Schematic representation of the TRPL measurement system.

Fig. 2.7 Schematic representation of the PLE measurement system.
(a) Block diagram of the PLE measurement system.
(b) Illustration of the sample holder.

Fig. 2.8 Relative intensity of the beam from the halogen lamp through the monochromator. The applied voltage and the current are 20V and 12 A, respectively. The entrance and output slit width are 1.0 mm.

Fig. 2.9 Block diagram of the PR measurement system.

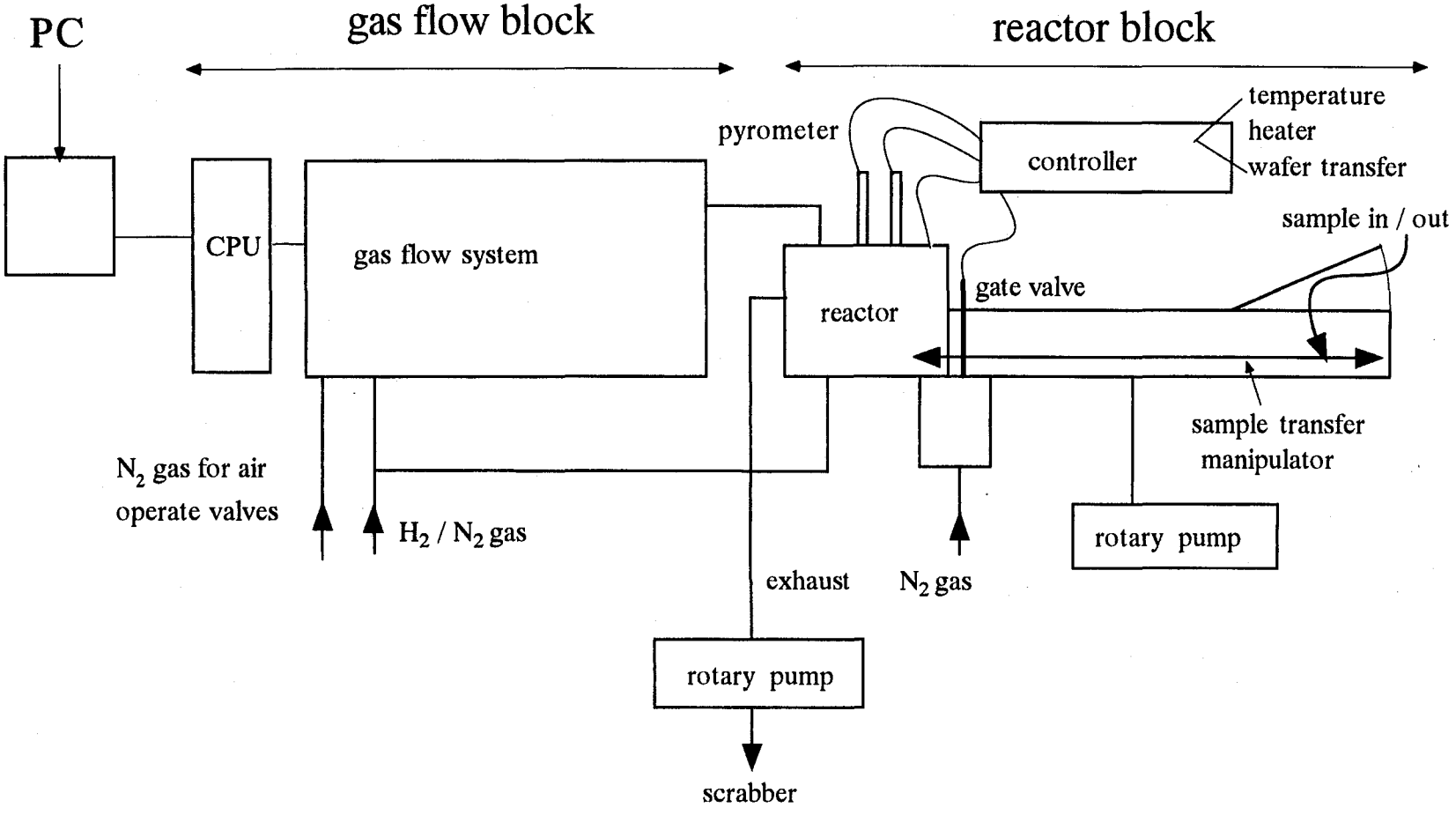
PC
gas flow block
reactor block
pyrometer
temperature
heater
wafer transfer
controller
CPU
gas flow system
sample in / out
reactor
gate valve
sample transfer
manipulator
N_2 gas for air
operate valves
H_2 / N_2 gas
exhaust
N_2 gas
rotary pump
rotary pump
scrabber

Fig. 2.1(a)

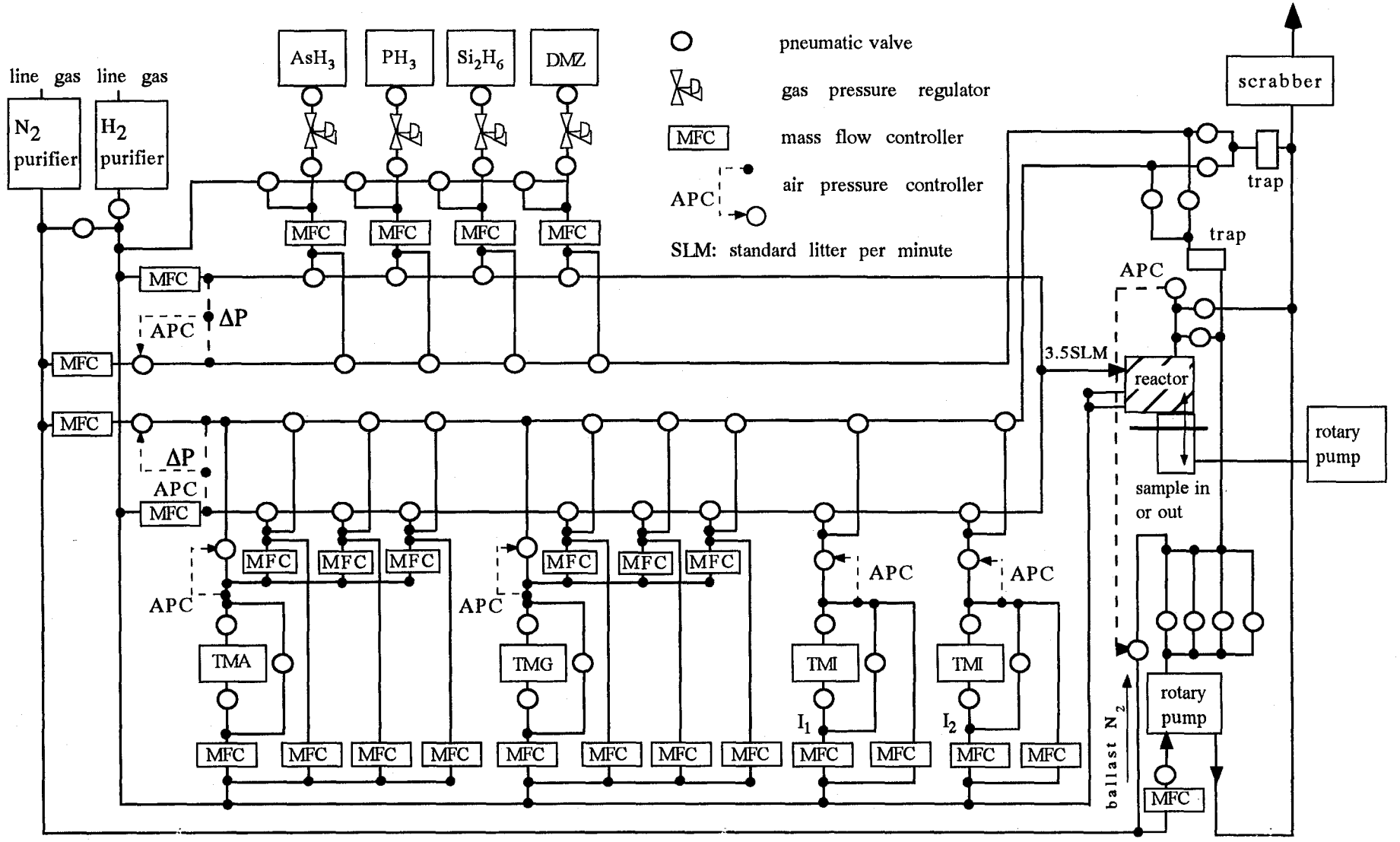
line gas
line gas
N_2 purifier
H_2 purifier
AsH_3
PH_3
Si_2H_6
DMZ
pneumatic valve
gas pressure regulator
MFC
mass flow controller
APC
air pressure controller
SLM: standard litter per minute
scrabber
trap
trap
APC
ΔP
3.5SLM
reactor
rotary pump
sample in or out
TMA
TMG
TMI
TMI
I_1
I_2
ballast N_2
rotary pump

Fig. 2.1(b)

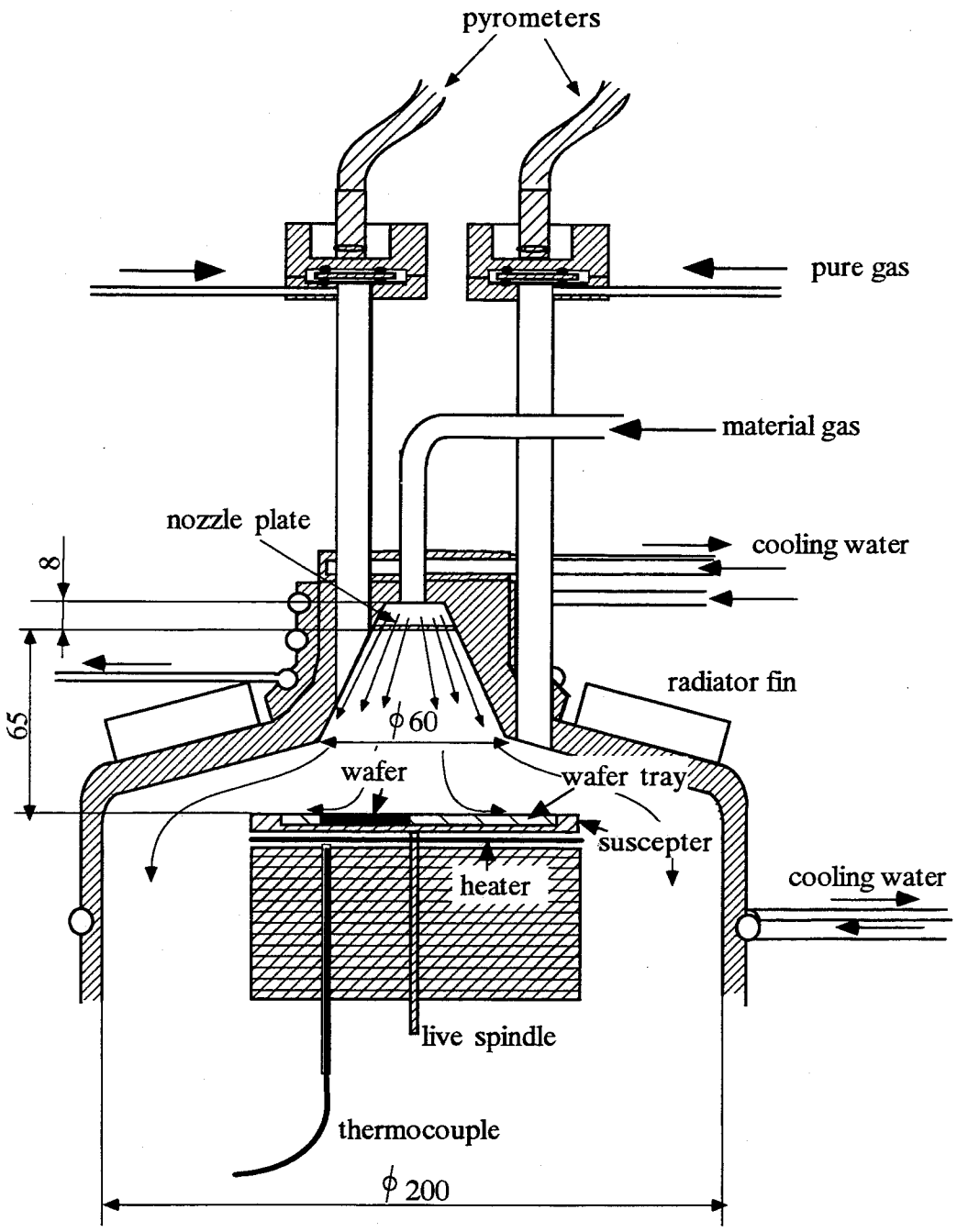
pyrometers
pure gas
material gas
nozzle plate
cooling water
8
radiator fin
65
ϕ60
wafer
wafer tray
suscepter
heater
cooling water
live spindle
thermocouple
ϕ200

Fig. 2.1(c)

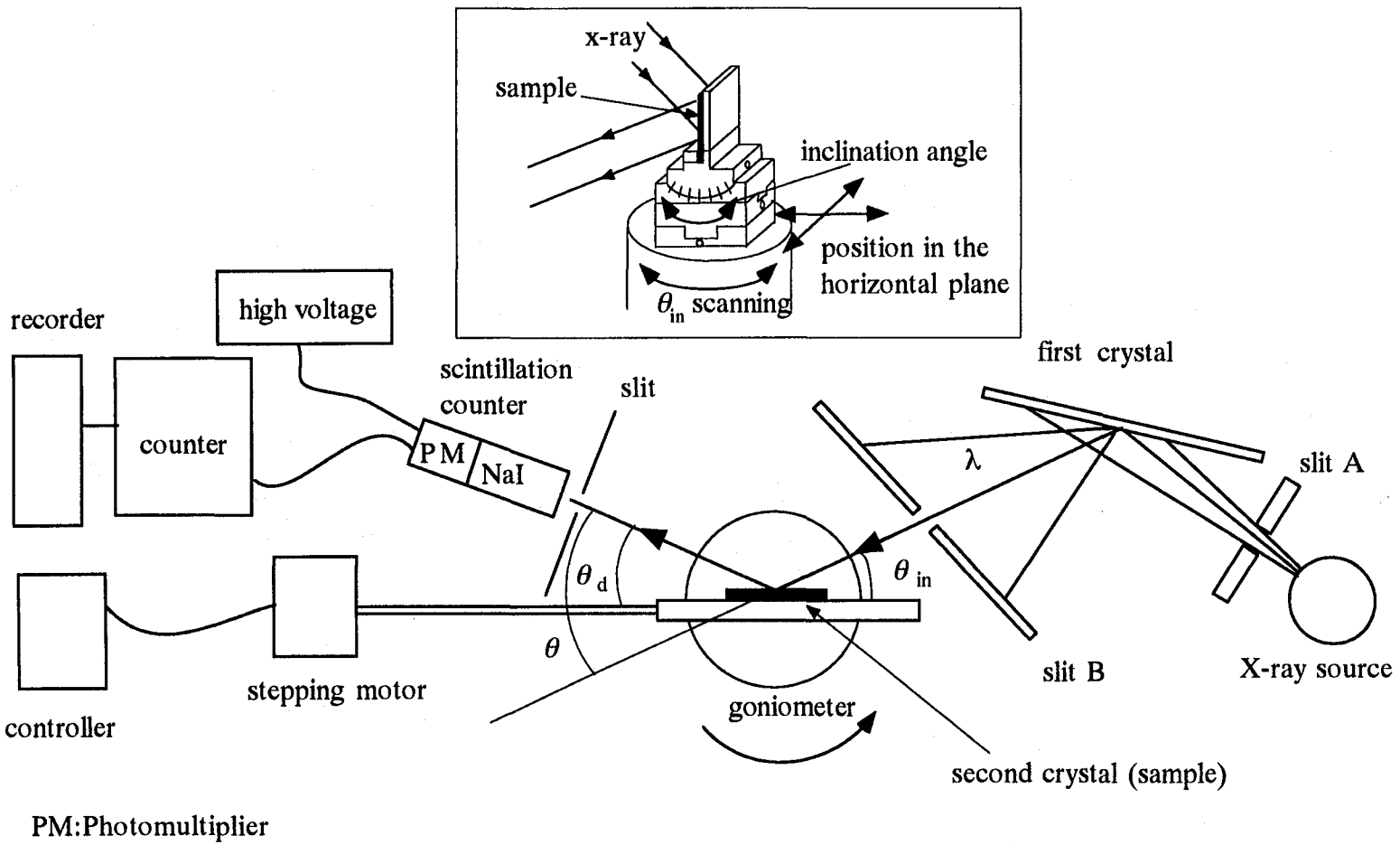
x-ray
sample
inclination angle
position in the horizontal plane
θ_{in} scanning
recorder
high voltage
counter
scintillation counter
PM
NaI
slit
first crystal
λ
slit A
θ_d
θ_{in}
θ
stepping motor
controller
goniometer
slit B
X-ray source
second crystal (sample)
PM:Photomultiplier

Fig. 2.2

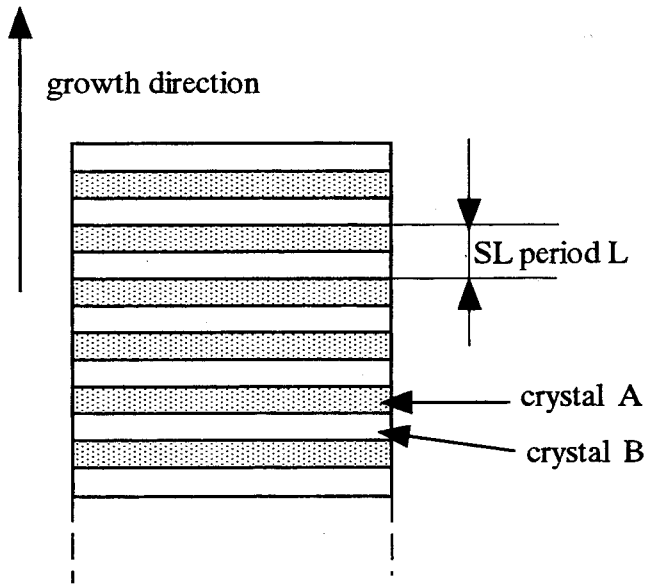

Fig. 2.3(a)

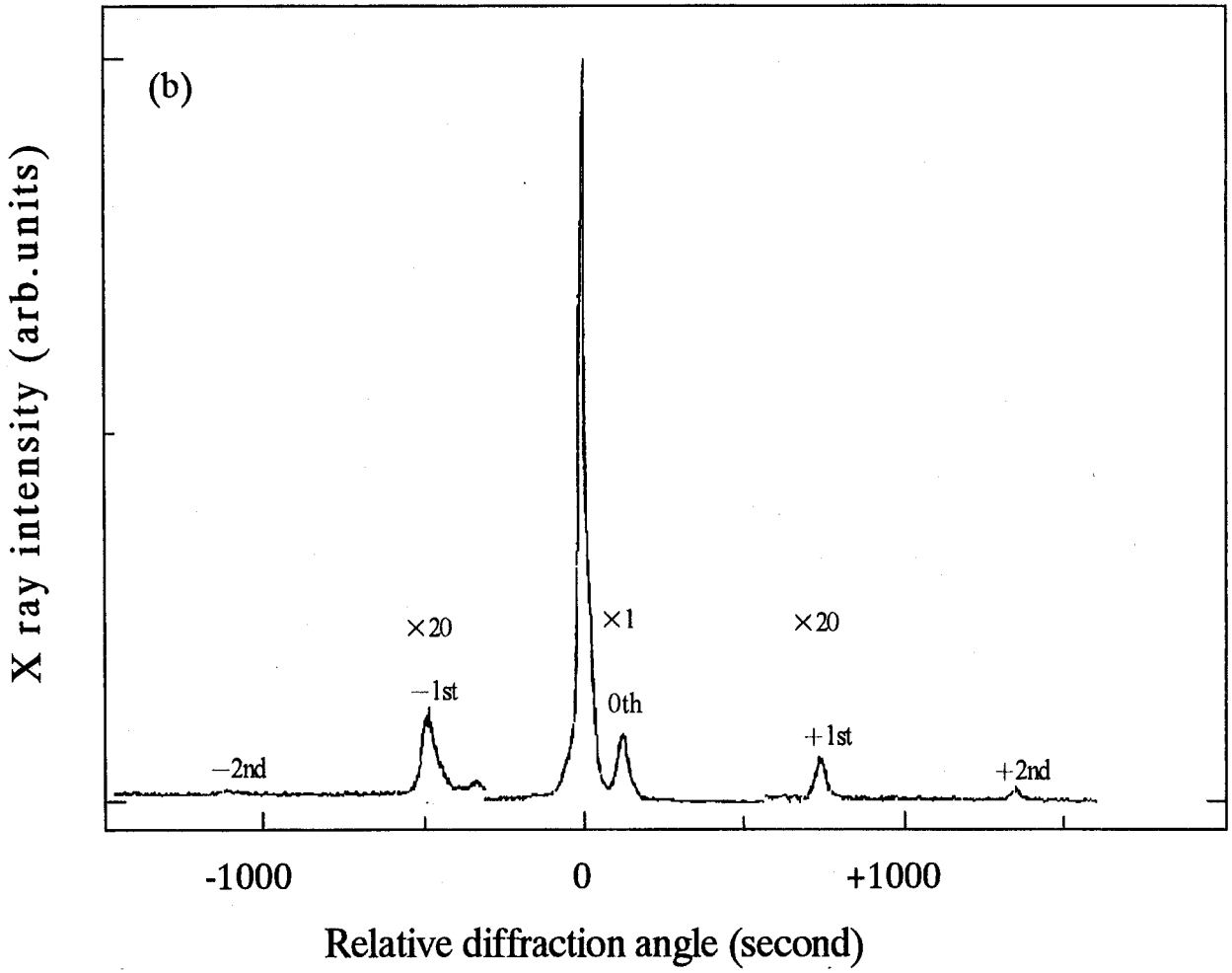
(b)
X ray intensity (arb.units)
×20
−1st
−2nd
×1
0th
×20
+1st
+2nd
-1000
0
+1000
Relative diffraction angle (second)

Fig. 2.3(b)

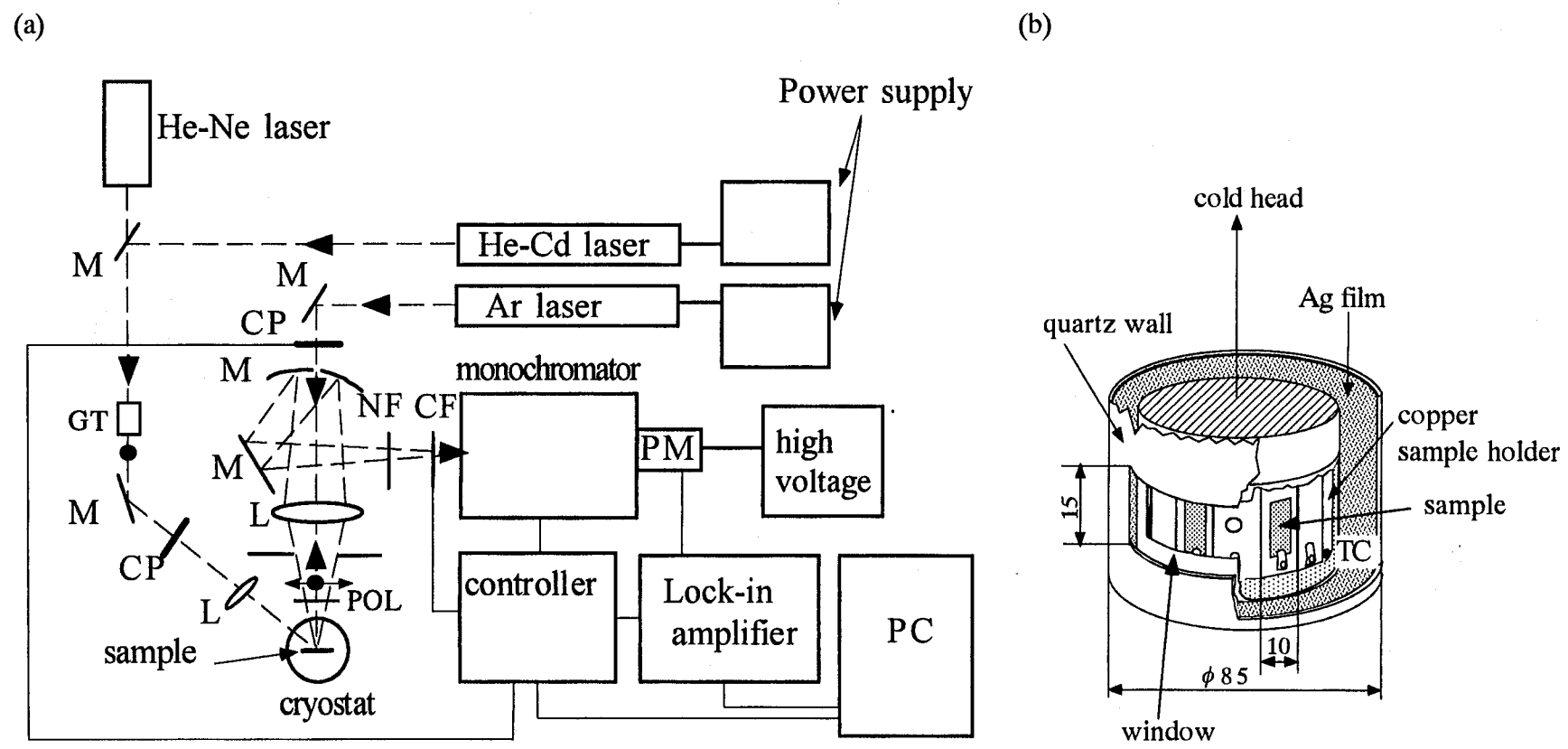
(a)
He-Ne laser
Power supply
He-Cd laser
Ar laser
M
M
CP
M
monochromator
GT
NF
CF
M
PM
high
voltage
M
L
CP
POL
L
controller
Lock-in
amplifier
PC
sample
cryostat
(b)
cold head
quartz wall
Ag film
copper
sample holder
sample
15
TC
10
ϕ85
window

Fig. 2.4

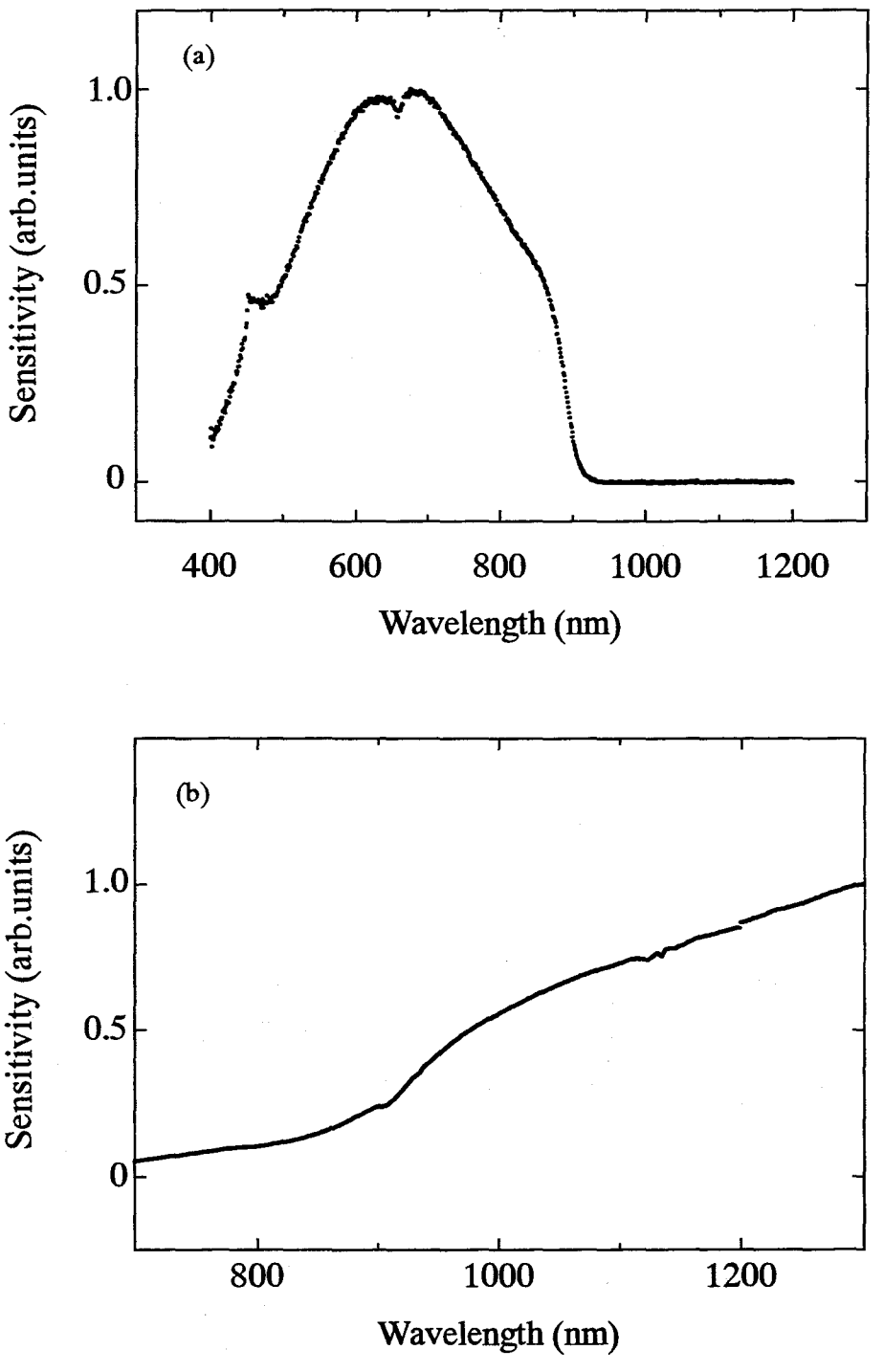
(a)
1.0
0.5
0
Sensitivity (arb.units)
400
600
800
1000
1200
Wavelength (nm)
(b)
1.0
0.5
0
Sensitivity (arb.units)
800
1000
1200
Wavelength (nm)

Fig. 2.5

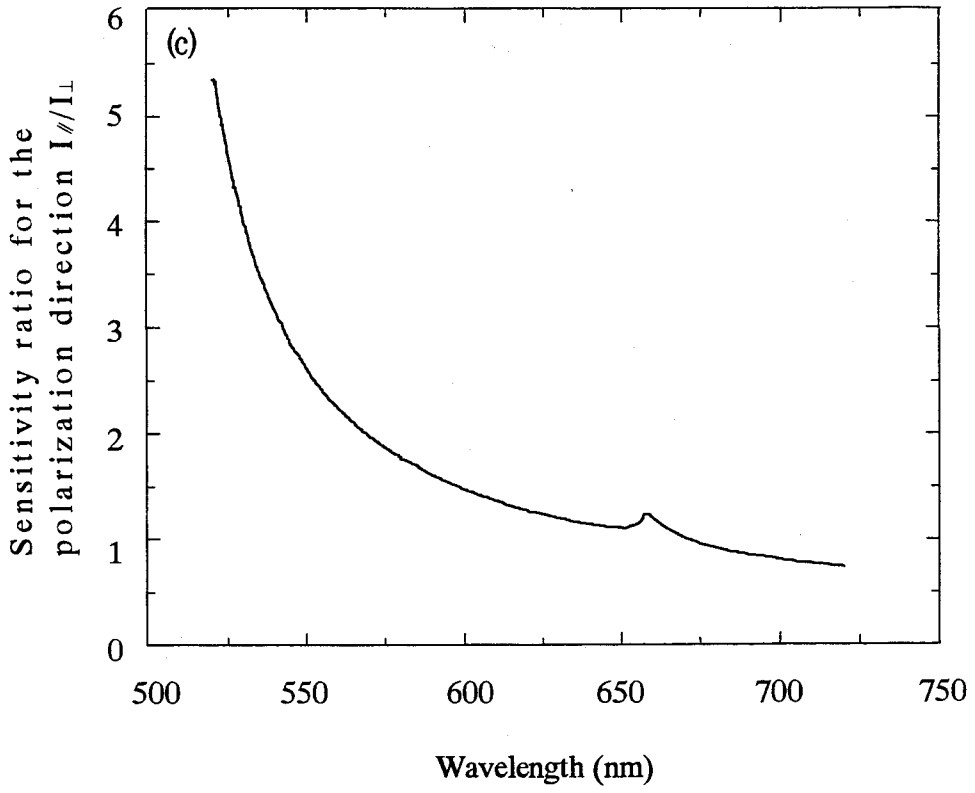
(c)
Sensitivity ratio for the polarization direction I//I⊥
0
1
2
3
4
5
6
500
550
600
650
700
750
Wavelength (nm)

Fig. 2.5(c)

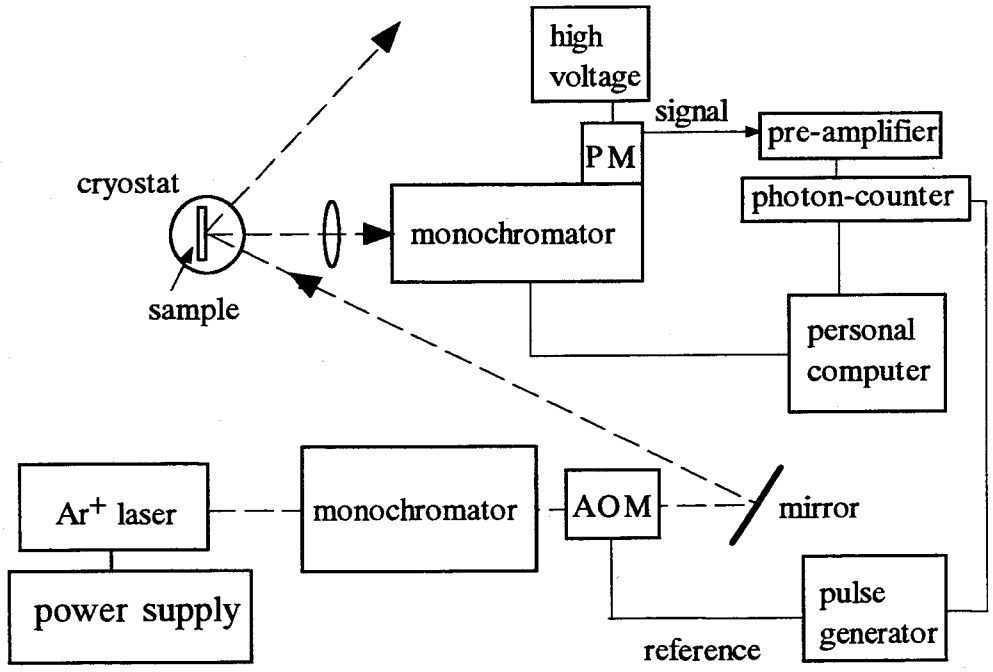
high
voltage
signal
pre-amplifier
PM
photon-counter
cryostat
monochromator
sample
personal
computer
Ar+ laser
monochromator
AOM
mirror
power supply
pulse
generator
reference

Fig. 2.6

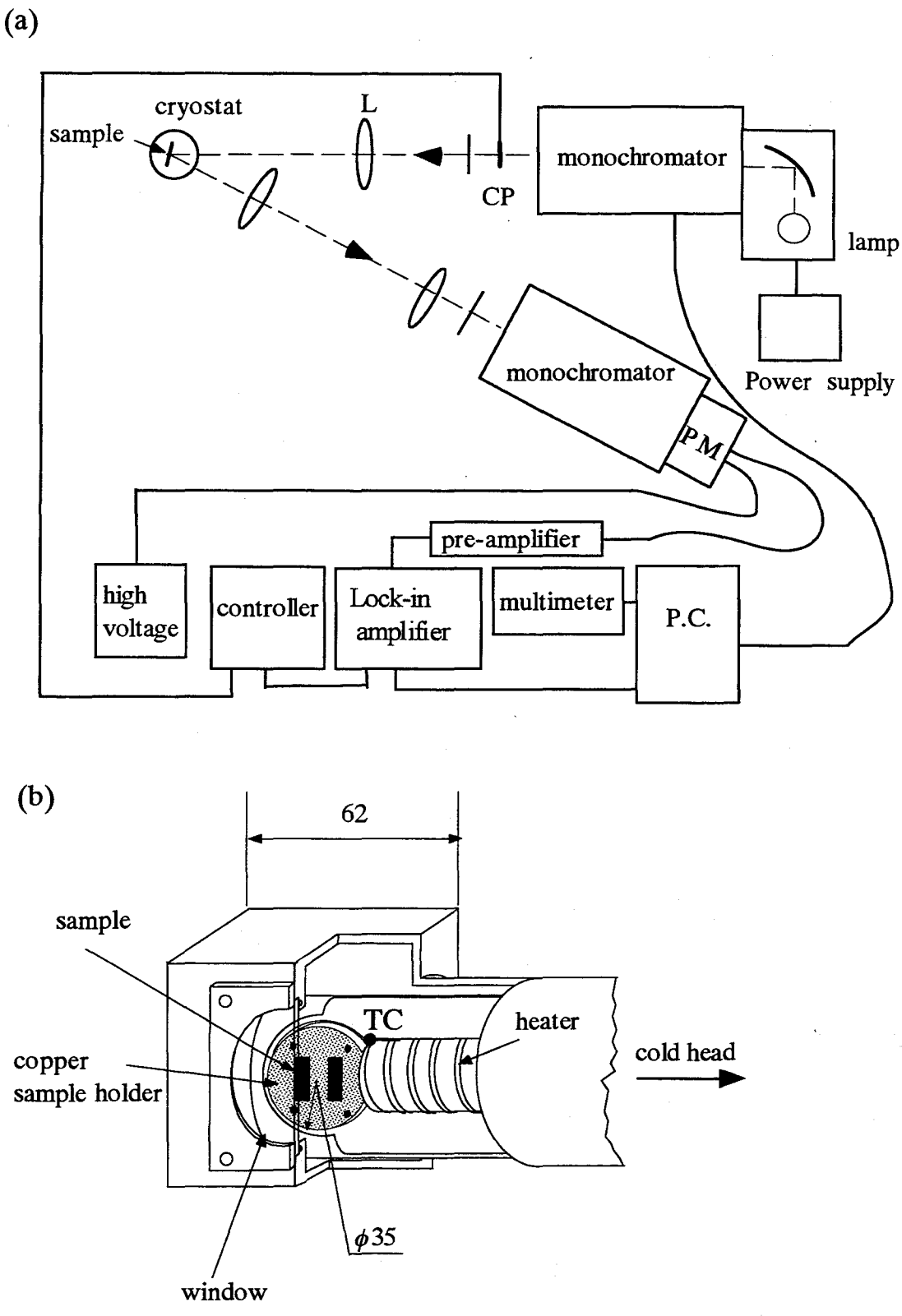
(a)
cryostat
sample
L
CP
monochromator
lamp
Power supply
monochromator
PM
pre-amplifier
high voltage
controller
Lock-in amplifier
multimeter
P.C.
(b)
62
sample
TC
heater
copper sample holder
cold head
φ35
window

Fig. 2.7

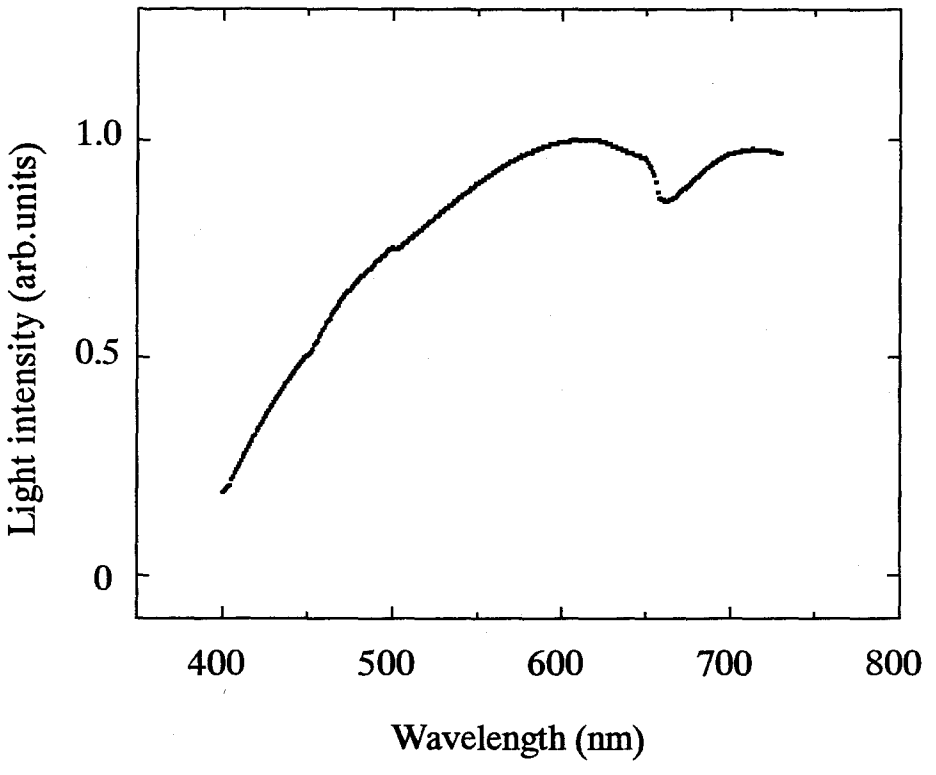
Light intensity (arb.units)
1.0
0.5
0
400
500
600
700
800
Wavelength (nm)

Fig. 2.8

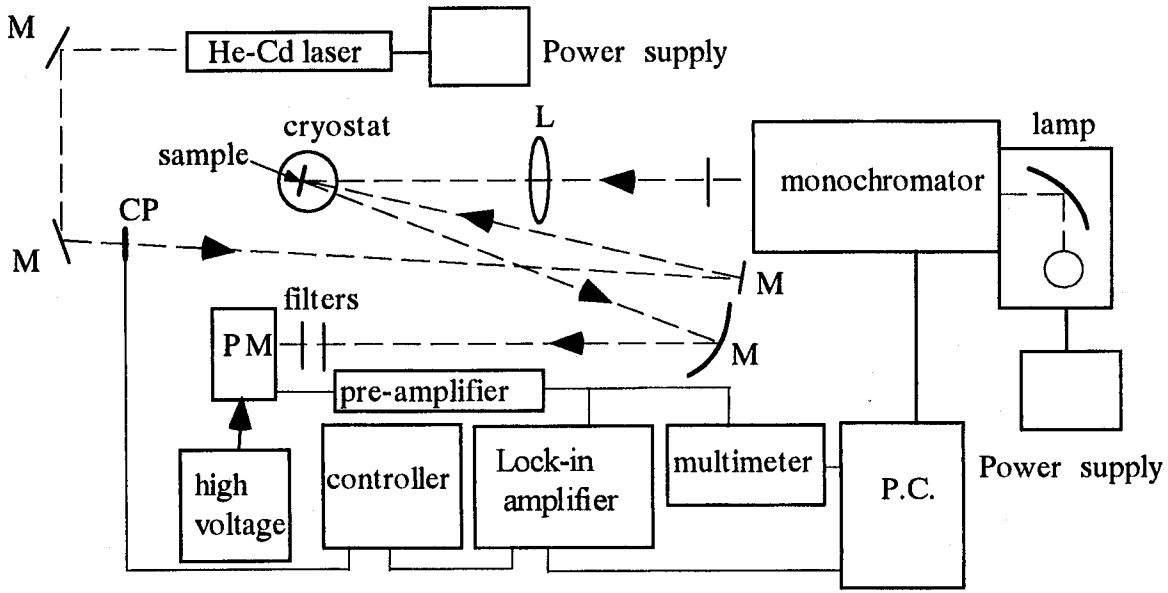
M
He-Cd laser
Power supply
cryostat
L
lamp
sample
monochromator
CP
M
M
filters
PM
M
pre-amplifier
high voltage
controller
Lock-in amplifier
multimeter
P.C.
Power supply

Fig. 2.9

Chapter III

Fundamental properties of samples grown by OMVPE

Abstract

The growth rates and the alloy compositions of crystals are derived from the diffraction angles of the satellite peaks in the x-ray diffraction patterns of superlattices. It is found that they do not depend on the misorientation angle (α_m) of the surface orientation of a substrate from (100) to [011] in the range of $0° \leq \alpha_m \leq 16°$. From the dependence of the PL peak energy on crystal temperature and the polarization of the PL spectra, it is concluded that disordered alloys are grown with misoriented substrates or high growth temperatures. Samples used in the following chapters are obtained from the region in a grown wafer where the alloy composition and layer thickness are uniform.

3.1 Growth rate and alloy composition

Firstly, we deal with the samples grown on (100) on axis. As an example we take the $(Al_{0.71}Ga_{0.29})_{0.5}In_{0.5}P$ /$Al_{0.57}In_{0.43}P$-SLs grown on GaAs substrates at 710 °C. Table 3-I shows the amounts of the column III source molecules supplied to the reactor. The growth time of the quaternary was kept constant (40 s) while that of the ternary was changed. An example of the XRD patterns has been shown in Fig. 2.3(b) for a sample with 20 s for the ternary. The SL period is determined from the 0th and ±1st satellite peaks. Figure 3.1(a) shows the relationship between the thickness of one period and the growth time of the ternary. The slope and the intersect of the fitted line give the growth rate of the $Al_{0.57}In_{0.43}P$ layers and the thickness of the $(Al_{0.71}Ga_{0.29})_{0.5}In_{0.5}P$ layers, respectively. The growth rates are thus obtained to be 0.40 (±0.01) nm/s and 0.59 (±0.01) nm/s for $Al_{0.57}In_{0.43}P$ and $(Al_{0.71}Ga_{0.29})_{0.5}In_{0.5}P$, respectively, and are shown in Table 3-I. The growth rates obtained from the SEM images of the bulk layers (≈1μm thickness) or by the TEM images for quantum well structures are found consistent with those in this table.

In fabricating $(Al_{0.71}Ga_{0.29})_{0.5}In_{0.5}P$ / $Al_yIn_{1-y}P$-SLs, I changed the AlP mole fraction y by the procedure given in section 2.1. For each y value, the growth time of $Al_yIn_{1-y}P$ and that of the $(Al_{0.71}Ga_{0.29})_{0.5}In_{0.5}P$ in one period were fixed at 20 s and 40 s, respectively. The periods as determined by XRD measurements are listed in Table 3-II. This result shows that the growth rate is independent of y. The uncertainties of the SL periods are discussed later.

Since, in general, the lattice constant of an alloy is different from that of the substrate as suggested in Table 3-III, a strained layer is formed. The situation is illustrated in Fig. 3.2. For a thin layer the lattice constants parallel to [011] and $[0\bar{1}1]$ are forced to be equal to that of the substrate. That parallel to [100] becomes different. We take $(Al_{0.71}Ga_{0.29})_{0.5}In_{0.5}P$ / $Al_yIn_{1-y}P$-SLs, particularly the SL shown in Fig. 2.3(b), as an example. The (400) diffraction measurement (Fig. 2.3(b)) gives the periodicity along [100]. The averaged lattice constant in the direction of [100] ($a_{av}^{\perp}$) is written as [1)]

$$a_{av}^{\perp} = (N_1 a_1^{\perp} + N_2 a_2^{\perp}) / (N_1 + N_2), \qquad (3\text{-}1)$$

where 1 and 2 are $(Al_{0.71}Ga_{0.29})_{0.5}In_{0.5}P$ and $Al_yIn_{1-y}P$, respectively. Here, N_1 and N_2 are the numbers of unit lattices (or thickness) of the two alloys in one period; and $a_1^{\perp}$ and $a_2^{\perp}$ are their lattice constants along [100]. We rewrite eq.(3-1).

$$\Delta a_2^{\perp} / a_0 = \{ (N_1 + N_2) \Delta a_{av}^{\perp} / a_0 - N_1 \Delta a_1^{\perp} / a_0 \} / N_2, \qquad (3\text{-}2)$$

where a_0 and $\Delta a_i{}^{\perp}/ a_0$ (i : 1, 2 or av) are the lattice constant of the substrate and the lattice mismatch along [100] as defined by $(a_i^{\perp} - a_0)/a_0$, respectively. For the present example of Fig. 2.3(b), N_1 and N_2 are obtained to be 83 (24 nm) and 28 (8.0 nm), respectively from the growth rates obtained before. The average lattice mismatch of the SL to GaAs along [100], or $\Delta a_{av}{}^{\perp} / a_0$ is found to be -0.11 % from the difference between the diffraction angle of the interference peak of GaAs and that of the 0th satellite in the XRD pattern. $\Delta a_1{}^{\perp} / a_0$ is determined to be +0.05 % from the peak position of an $(Al_{0.71}Ga_{0.29})_{0.5}In_{0.5}P$ single layer on a GaAs. $\Delta a_2{}^{\perp} / a_0$ is obtained to be -0.58 % from substitution of these values into eq.(3-2). The original lattice mismatch $\Delta a_2 / a_0$ is given from the obtained $\Delta a_2{}^{\perp} / a_0$ and the elastic stiffness C_{ij}.

$$\frac{\Delta a_2}{a_0}(y) = \frac{1}{1+2\dfrac{C_{12}}{C_{11}}(y)} \frac{\Delta a_2{}^{\perp}}{a_0} \quad . \tag{3-3}$$

Here, C_{12} / C_{11}, the lattice constant of InP and the lattice constant of AlP are obtained from a reference. [2] C_{12} / C_{11} of AlP was derived from substitution of the experimentally obtained $\Delta a^{\perp} / a_0$ value of an AlP layer grown on a GaP substrate and the $\Delta a / a_0$ value calculated using lattice constants of bulk AlP and GaP into eq.(3-3). The values for the binary compounds concerned in this thesis are listed in Table 3-III. [2] The ratios of the elastic stiffness C_{12} / C_{11} and a_2 for a y value are obtained from the linear interpolation of the respective values of AlP and those of InP (Vegard's law). The y value for a $\Delta a_2 / a_0$ is determined so that it is consistent with eq.(3-3). For the present example of Fig. 2.3(b), y of 0.57 is obtained. Figure 3.1(b) shows the plots of y values obtained by the above method as a function of the intended y. The agreement is satisfactory.

The uncertainty of the thickness of a layer consists of the uncertainty of the average thickness and the local fluctuation of thickness. The former is given as the product of the growth time and the uncertainty of the growth rate determined earlier. For the example of the $Al_{0.57}In_{0.43}P$ layer with 20 s of growth time shown in Fig. 2.3(b), it is estimated to be 0.2 nm. The width of XRD peaks is affected by several factors: the local fluctuation of the layer thickness, the local fluctuation of the alloy composition, and so forth. The fluctuation of the 0th satellite peak position is expressed by

$$\Delta\left(\frac{\Delta a_{av}{}^{\perp}}{a_0}\right) = \frac{\partial\left(\dfrac{\Delta a_{av}{}^{\perp}}{a_0}\right)}{\partial N_1}\Delta N_1 + \frac{\partial\left(\dfrac{\Delta a_{av}{}^{\perp}}{a_0}\right)}{\partial N_2}\Delta N_2 + \frac{\partial\left(\dfrac{\Delta a_{av}{}^{\perp}}{a_0}\right)}{\partial a_1}\Delta a_1 + \frac{\partial\left(\dfrac{\Delta a_{av}{}^{\perp}}{a_0}\right)}{\partial a_2}\Delta a_2 + F_i . \tag{3-4}$$

Here, F_i is the contribution from factors other than ΔN_i and Δa_i (i=1 or 2), such as instrumental factors. By dropping the Δa_i terms we estimate the upper limit of the contribution from ΔN_i. Since we are interested in local fluctuations, ΔN_1 is assumed equal to ΔN_2. From the difference between the full width at half maximum (FWHM) of the substrate and that of the 0th satellite peak we eliminate the effect of F_i. Equation (3-4) is transformed to

$$\Delta\left(\frac{\Delta a_{av}^{\perp}}{a_0}\right) - F_i = \frac{\frac{\Delta a_1^{\perp}}{a_0} - \frac{\Delta a_2^{\perp}}{a_0}}{N_1 + N_2}\Delta N_2 . \qquad (3\text{-}5)$$

All the quantities except for ΔN_2 have been determined already. For the present example $\Delta\left(\frac{\Delta a_{av}^{\perp}}{a_0}\right)$ -F_i is found to be 0.016 % of the lattice constant from the FWHM of the XRD peaks. ΔN_2 is thus obtained to be approximately 2.8 from eq.(3-5) or the fluctuation of ± 0.40 nm. For the samples treated in this thesis the uncertainties are in the range of ± 0.3 - 0.6 nm. A TEM image could also be adopted for the same purpose, but the resolution of its image is found to be 0.3 - 0.6 nm. Therefore, it is concluded that the thickness of a layer has an uncertainty less than 0.3 - 0.6 nm.

Now we deal with layers grown on misoriented substrates. Two kinds of misoriented substrates are used: (100) with misorientation angle α_m = 7° or 15.8° toward [011]; here the latter orientation is equal to (511)A. An SL is grown on a substrate as shown schematically in Figure 3.3(a). The geometrical configuration of the incident and diffracted x-rays, slit direction, and a sample is depicted in Fig. 3.3(b). The direction of the outlet slit (s) is parallel to [011]. The period along [100] (L') is obtained from the substitution of the diffraction angles of the + or - 1st and the 0th satellite peaks in the XRD pattern into eq.(2-2). The SL period (L) is derived from the equation shown in the figure. An example of the dependence of experimentally obtained y and L on the misorientation angle is shown in Table 3-IV. It is found that the SL period, and thus the growth rate, and the alloy composition are independent of the misorientation angle in the range of 0 - 15.8 degrees.

I also performed similar studies on the $Ga_xIn_{1-x}P$ /$(Al_{0.56}Ga_{0.44})_{0.5}In_{0.5}P$- SLs. All the properties are qualitatively the same. The growth rate is 0.39 (±0.01) nm/s both for $Ga_xIn_{1-x}P$ and $(Al_{0.56}Ga_{0.44})_{0.5}In_{0.5}P$. These values are listed in Table 3-I.

3.2 Difference between the optical transition spectra of ordered alloys and those of disordered alloys

It is known that the surface orientation of the substrate and the growth temperature (T_g) are the dominant factors which determine the development of LRO. I prepared two samples of $Ga_{0.52}In_{0.48}P$; sample A: grown on (100) substrate at 680 °C, and sample B: (511)A substrate at 720 °C. I excited these samples with the He-Cd laser light (Fig. 2.4) polarized along [011] with the Glan-thompson prism. PL spectra was observed with its polarized components ([011] and $[01\bar{1}]$) resolved. Figure 3.4 shows the result. PL of sample A is polarized while that of sample B is almost unpolarized. It is known that the PL from ordered GaInP is polarized because of the asymmetry of the atomic configuration due to the superlattice along $[1\bar{1}1]$ and the resultant splitting of the state at the vertex of the valence band. [3)-6)] The peak energy of the PL of sample B agrees with that of a sample known to be disordered (grown by liquid phase epitaxy). [7)] Thus I concluded that sample B is disordered. A sample grown on an (100) substrate with misorientation of 7° toward the [011] direction at 730 °C was also found disordered.

Figure 3.5(a) shows the temperature dependence of the PL peak energy of sample B. It decreases with an increase in temperature, which is characteristic to a disordered alloy. In this figure the result of other two samples are given; sample C: grown on (100) at 660 °C , and sample D: on (100) at 730 °C . Sample C clearly shows the different features from sample B: lower energies (see Fig. 3.4(a)) and the initial increase in low temperatures. The latter suggests a change of the main electron transition process from Γ_{6c} - $\Gamma_{4v,5v}$ to Γ_{6c} - $\Gamma_{6v(2)}$ (see Fig. 1.5 in Chap.I) or from the transition in the strongly ordered domains to that in the weakly ordered domains.[3)4)8)] This is the characteristic to an ordered alloy. Thus sample C is judged ordered. Sample D appears to be similar to sample B. However, this reveals the similar initial increase. Thus I judge sample B to be weakly ordered. Since the temperature 730 °C is not high enough for producing disordered alloys on (100) on axis substrates, misoriented substrates are required for disordered alloys.

I also investigated the $GaAs_{0.61}P_{0.39}$ substrate; the surface orientation of the substrates available was (100) with misorientation of 2 ° toward $[01\bar{1}]$. Figure 3.5(b) shows the PL peak energy of the $Ga_{0.70}In_{0.30}P$ alloy samples grown at 740 °C and 700 °C. The former sample has no dip at low temperatures, and the PL is found to be unpolarized. Hence this sample is judged disordered.

In the following chapters disordered alloys are grown on (511)A GaAs at 710 - 730 °C, on (100) 7 °off toward [011] at 720 - 740 °C, or on $GaAs_{0.61}P_{0.39}$ substrate with (100) 2° off toward $[01\bar{1}]$ at 740 - 760 °C.

3.3 Uniformity of the crystal properties

The chemical reaction on the surface of a wafer is affected by the temperature of the wafer, the gas flow rate, the thickness of the laminar boundary layer, and so forth. These growth conditions could vary depending on the position on the wafer; for instance, the gas flow condition around the peripheral region would be different from that near the center. The substrate used is of a circular shape of 2 inch diameter (type A), a quarter of the 2 inch wafer (type B), or 10×30 mm rectangular shape (type C).

An example of the distribution of the PL peak wavelength for a disordered bulk $Ga_{0.52}In_{0.48}P$ alloy is shown in Fig. 3.6 for the type C wafer. It may be concluded that the region of 6×25 mm near the center is uniform with respect to the PL peak energy or the alloy composition. Figure 3.7 shows the PL peak wavelength distribution for a disordered $Al_{0.53}In_{0.47}P/Ga_{0.52}In_{0.48}P$ (6 nm)/ $Al_{0.53}In_{0.47}P$ - single quantum well (SQW) structure. This figure indicates that the thickness of a QW layer at the fringe is larger than that at the center. A 4×24 mm region near the center is judged uniform. Figure 3.8 shows the regions that are found uniform, and used as a sample in the following chapters.

References

1) Woo-Young Choi and Clifton G. Fonstad, Appl. Phys. Lett. 62, 2815 (1993)
2) M.Neuberger, Hand book of electronic materials vol.2: III-V semiconducting compounds, Plenum Publishing Corp., New York, 1971
3) T.Kita, M.Nishimoto, H.Nakayama, and T.Nishino, Phys.Rev.B 45, 6637 (1992)
4) M.C.Delong, P.C.Taylor, and J.M.Olson, Appl.Phys.Lett. 57, 620 (1990)
5) M.Kondow, H.Kakibayashi, S.Minagawa, Y.Inoue, T.Nishino, and Y.Hamakawa, J.Cryst.Growth 93, 412 (1988)
6) Su-Huai Wei and Alex Zunger, Phys.Rev.B 39, 3279 (1988)
7) M.Kondow, H.Kakibayashi, and S.Minagawa, J.Cryst.Growth 88, 291 (1988)
8) G.S.Horner, A.Mascarehas, R.G.Alonso, D.J.Friedman, K.Sinha, K.A.Bertness, J.G.Zhu, and J.M.Olson, Phys.Rev.B 48, (1993)

Table 3-I Flow rates of column III source molecule gases and growth rates of layers at 710 °C.

	$Al_{0.53}In_{0.47}P$	$Ga_{0.52}In_{0.48}P$	$(Al_{0.71}Ga_{0.29})_{0.5}In_{0.5}P$	$(Al_{0.56}Ga_{0.44})_{0.5}In_{0.5}P$
TMA (μmol /sec)	6.5		6.9	3.4
TMG (μmol /sec)		5.8	2.6	2.6
TMI (μmol /sec)	7.5	7.7	11.9	7.7
growth rate (μm/hour)	1.44(±0.04)	1.40(±0.04)	2.12(±0.04)	1.40(±0.04)

Table 3-II Periods of $Al_yIn_{1-y}P/(Al_{0.71}Ga_{0.29})_{0.5}In_{0.5}P$ -SLs for various y.
The growth time of $Al_yIn_{1-y}P$ and $(Al_{0.71}Ga_{0.29})_{0.5}In_{0.5}P$ are 20 s and 40 s, respectively. T_g = 710 °C. The measurements were conducted at room temperature.

y	0.47	0.49	0.53	0.55	0.57	0.62
SL period (nm)	30.6(±0.3)	30.8(±0.3)	30.6(-)	30.2(±0.6)	30.9(±0.4)	30.5(±0.3)

Table 3-III Lattice constants and ratios of elastic stiffness (C_{12}/C_{11}) for binary compounds.

	AlP	GaP	InP	GaAs
a (Å) [a)]	5.463	5.450	5.868	5.653
C_{12}/C_{11}	0.483*	0.442[a)]	0.564[a)]	0.453 [a)] **

a) ref.2
*: at RT, **: at 298 K, the other data was obtained at 300 K.

Table 3-IV Thickness and AlP mole fraction of $Al_yIn_{1-y}P$ in SLs vs. misorientation angle of the substrate.

The growth time of a layer is 20 s for an $Al_yIn_{1-y}P$ layer and is 40 s for an $(Al_{0.71}Ga_{0.29})_{0.5}In_{0.5}P$ layer. The partial pressure of the organo-metal molecules are common for all the cases. T_g = 720 °C. The measurements were conducted at room temperature.

Misorientation angle (degree)	0	7	15.8
SL period (nm)	30.9(±0.4)	30.6(±0.3)	30.3(±0.3)
y	0.570(±0.004)	0.579(±0.003)	0.576(±0.003)

Figure captions

Fig. 3.1 Results of XRD measurements for $Al_yIn_{1-y}P$ /$(Al_{0.71}Ga_{0.29})_{0.5}In_{0.5}P$ -SLs on (100) on axis substrates. The growth time of $Al_yIn_{1-y}P$ and $(Al_{0.71}Ga_{0.29})_{0.5}In_{0.5}P$ are 20 s and 40 s, respectively. The lattice mismatch of $(Al_{0.71}Ga_{0.29})_{0.5}In_{0.5}P$ to GaAs $(\Delta a^{\perp}_1 / a_0)$ is +0.05%.

(a) Relation between the growth time of $Al_{0.57}In_{0.43}P$ and the SL period.

(b) Relation between the intended y and the experimentally determined y. The growth time of $Al_yIn_{1-y}P$ and that of $(Al_{0.71}Ga_{0.29})_{0.5}In_{0.5}P$ are 20 s and 40 s, respectively.

Fig. 3.2 Schematic illustration of unstrained and tetragonally deformed lattices.

Fig. 3.3 Geometric setting of a sample in an XRD measurement.

(a) Incident x-ray is parallel to (011). The x-ray slit is in the plane [011] (vector s). θ_{in} is the incident angle of the x-ray. L is the thickness of one SL period. L' is the apparent SL period in measurement. The dashed lines indicate <011> and <100>. The misorientation angle of the surface orientation from (100) is denoted by α_m.

(b) Geometric configuration of the incident and diffracted x-ray and a sample.

Fig. 3.4 PL spectra with its polarized components resolved for bulk $Ga_{0.52}In_{0.48}P$ alloys. PL measurements were performed at RT.

(a) For an ordered alloy. The sample is grown on an (100) on axis GaAs substrate at 680°C (sample A).

(b) For a disordered alloy. The sample is grown on a (511)A GaAs substrate at 720°C (sample B).

Fig. 3.5 Plot of the PL peak energy as a function of crystal temperature.

(a) For $Ga_{0.52}In_{0.48}P$ alloys. ■: sample C grown at 660 °C; ●: sample B grown at 720 °C; □: sample D grown at 730 °C. Sample B is grown on a (511) A substrate. The other samples are on (100) on axis substrates.

(b) For $Ga_{0.70}In_{0.30}P$ alloys. O : sample grown at 740 °C; ● :sample grown at 700 °C.

Fig. 3.6 Distribution of the PL peak wavelength of a disordered bulk $Ga_{0.52}In_{0.48}P$ on a type

C substrate at RT.
X-Y coordinate in the sample is denoted in the inset.
(a) Distribution along the Y direction. X is 5mm.
(b) Distribution along the X direction. The measured positions are in two lines with Y of 3mm and 15mm.

Fig. 3.7 Distribution of the PL peak wavelength at RT of an $Al_{0.53}In_{0.47}P/Ga_{0.52}In_{0.48}P$ / $Al_{0.53}In_{0.47}P$ quantum well on a type C substrate.
(a) Distribution along the Y direction. X is 5mm.
(b) Distribution along the X direction. The measured positions are in two lines with Y of 3mm and 15mm.

Fig. 3.8 Areas used in the studies of the following chapters for samples of type A, B, and C wafers.
The hatched area is chosen. The other parts are removed before measurements in the following chapters.

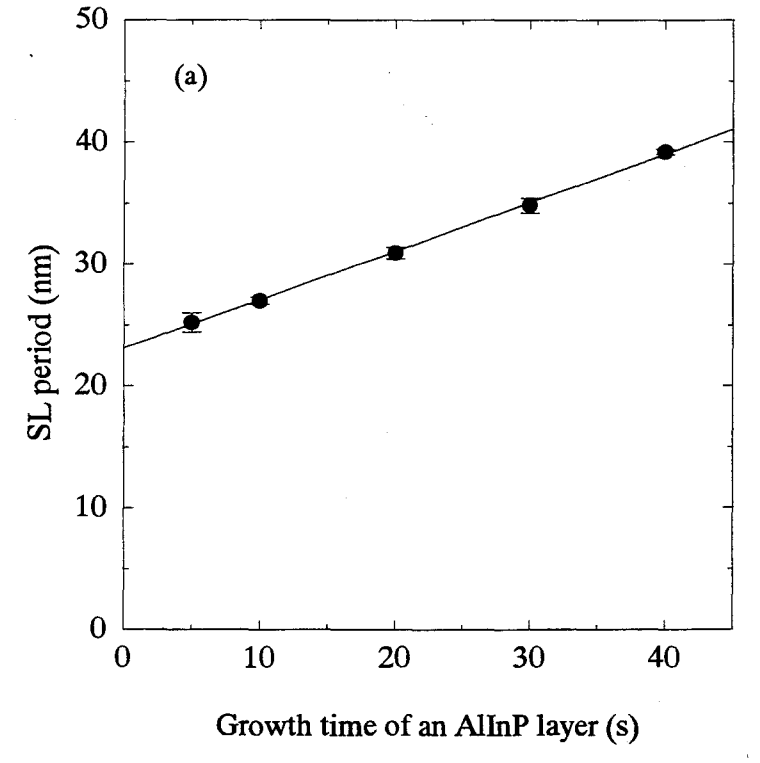
(a)
SL period (nm)
Growth time of an AlInP layer (s)
0
10
20
30
40
50

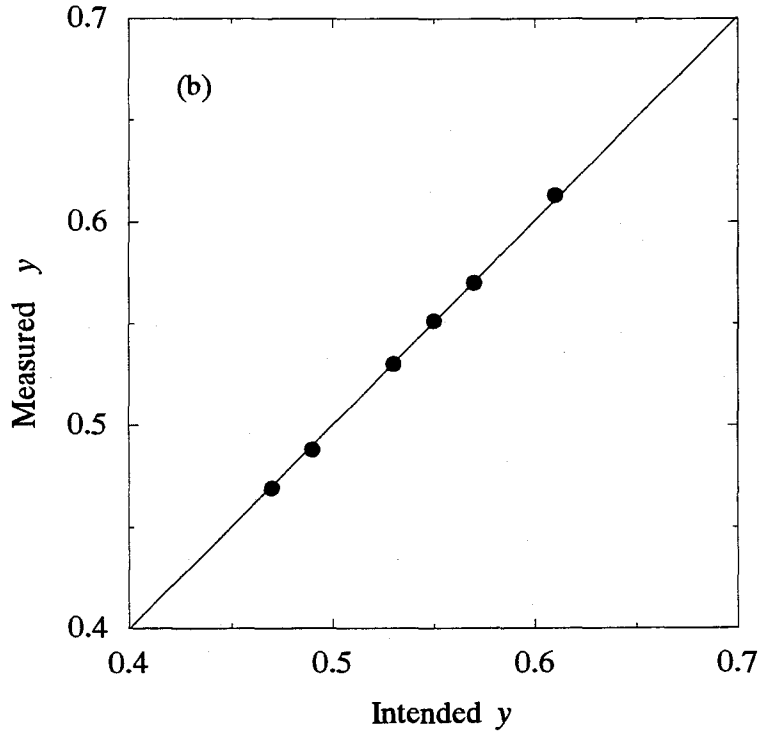
(b)
Measured y
Intended y
0.4
0.5
0.6
0.7

Fig. 3.1

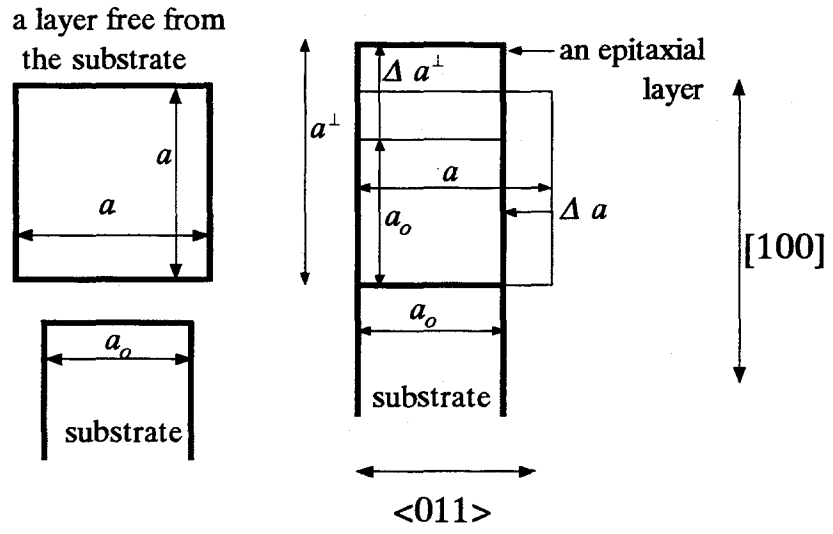
a layer free from
the substrate
a
a
a_o
substrate
$a^{\perp}$
$\Delta a^{\perp}$
an epitaxial
layer
a
Δa
a_o
a_o
substrate
[100]
<011>

Fig. 3.2

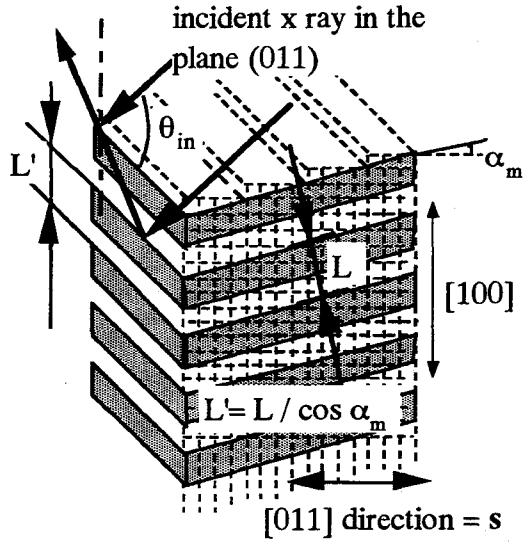
incident x ray in the
plane (011)
θin
L'
αm
L
[100]
L'= L / cos αm
[011] direction = s

(a)

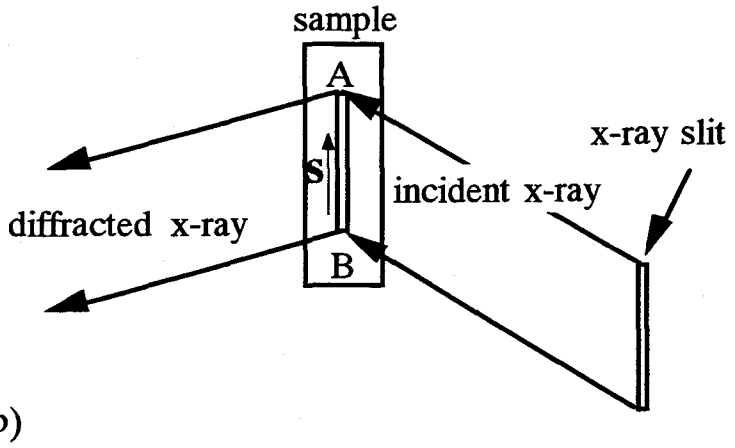
sample
A
B
S
x-ray slit
incident x-ray
diffracted x-ray

(b)

Fig. 3.3

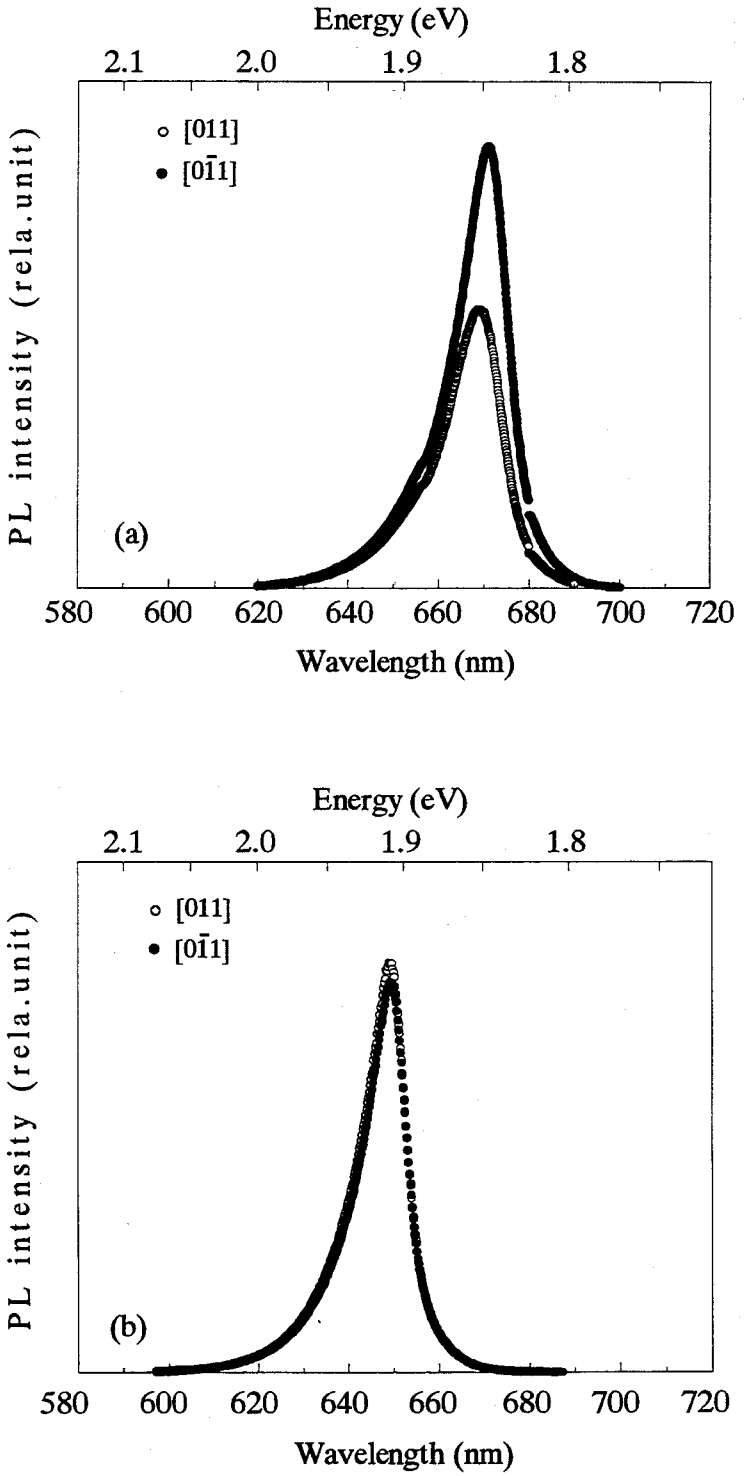
Energy (eV)
2.1
2.0
1.9
1.8
[011]
[0$\bar{1}$1]
PL intensity (rela.unit)
(a)
580
600
620
640
660
680
700
720
Wavelength (nm)
Energy (eV)
2.1
2.0
1.9
1.8
[011]
[0$\bar{1}$1]
PL intensity (rela.unit)
(b)
580
600
620
640
660
680
700
720
Wavelength (nm)

Fig. 3.4

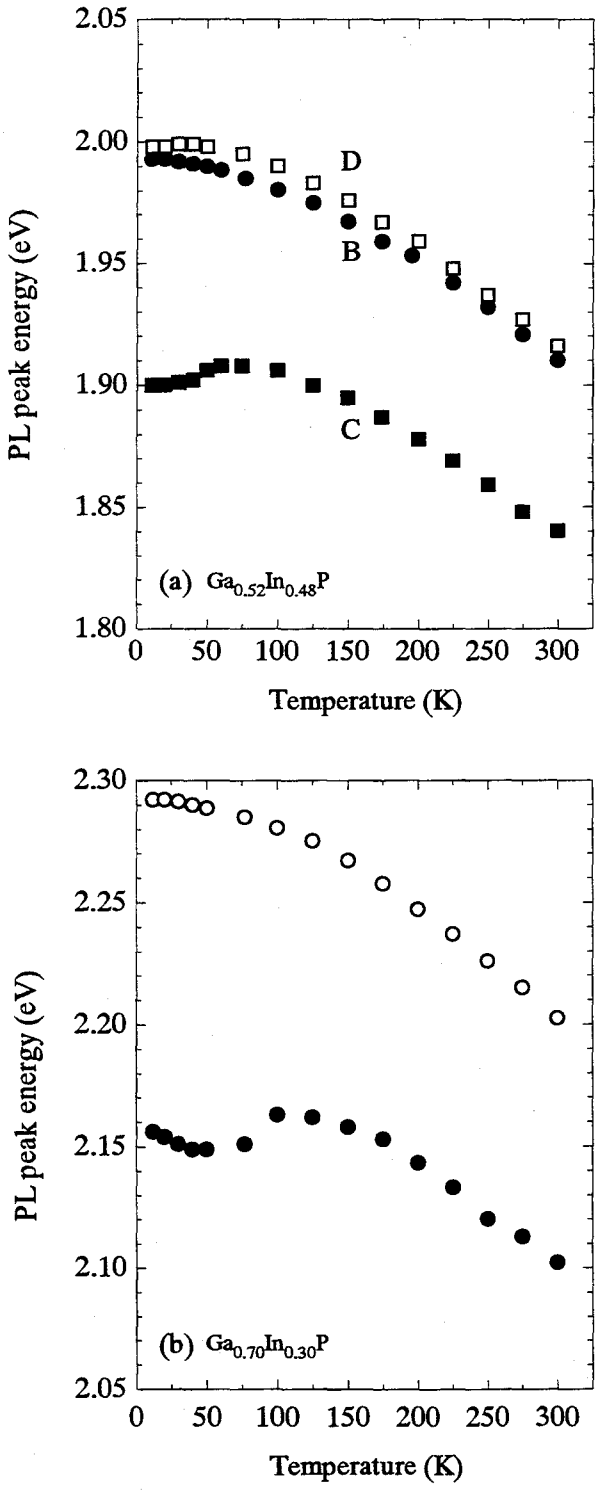
2.05
2.00
1.95
1.90
1.85
1.80
PL peak energy (eV)
D
B
C
(a) $Ga_{0.52}In_{0.48}P$
0
50
100
150
200
250
300
Temperature (K)
2.30
2.25
2.20
2.15
2.10
2.05
PL peak energy (eV)
(b) $Ga_{0.70}In_{0.30}P$
0
50
100
150
200
250
300
Temperature (K)

Fig. 3.5

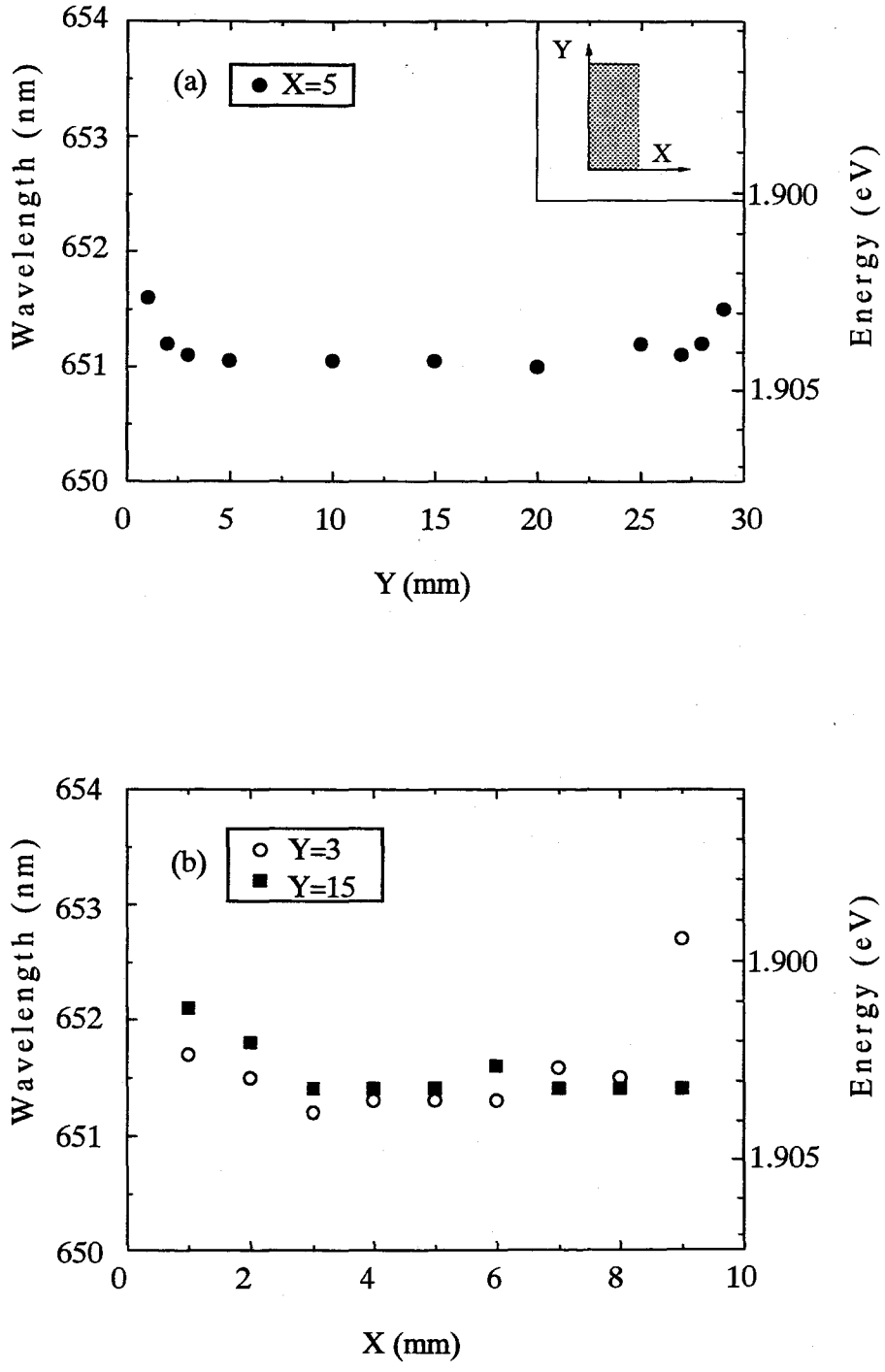
(a)
X=5
Y
X
Wavelength (nm)
Energy (eV)
654
653
652
651
650
1.900
1.905
0
5
10
15
20
25
30
Y (mm)
(b)
Y=3
Y=15
Wavelength (nm)
Energy (eV)
654
653
652
651
650
1.900
1.905
0
2
4
6
8
10
X (mm)

Fig. 3.6

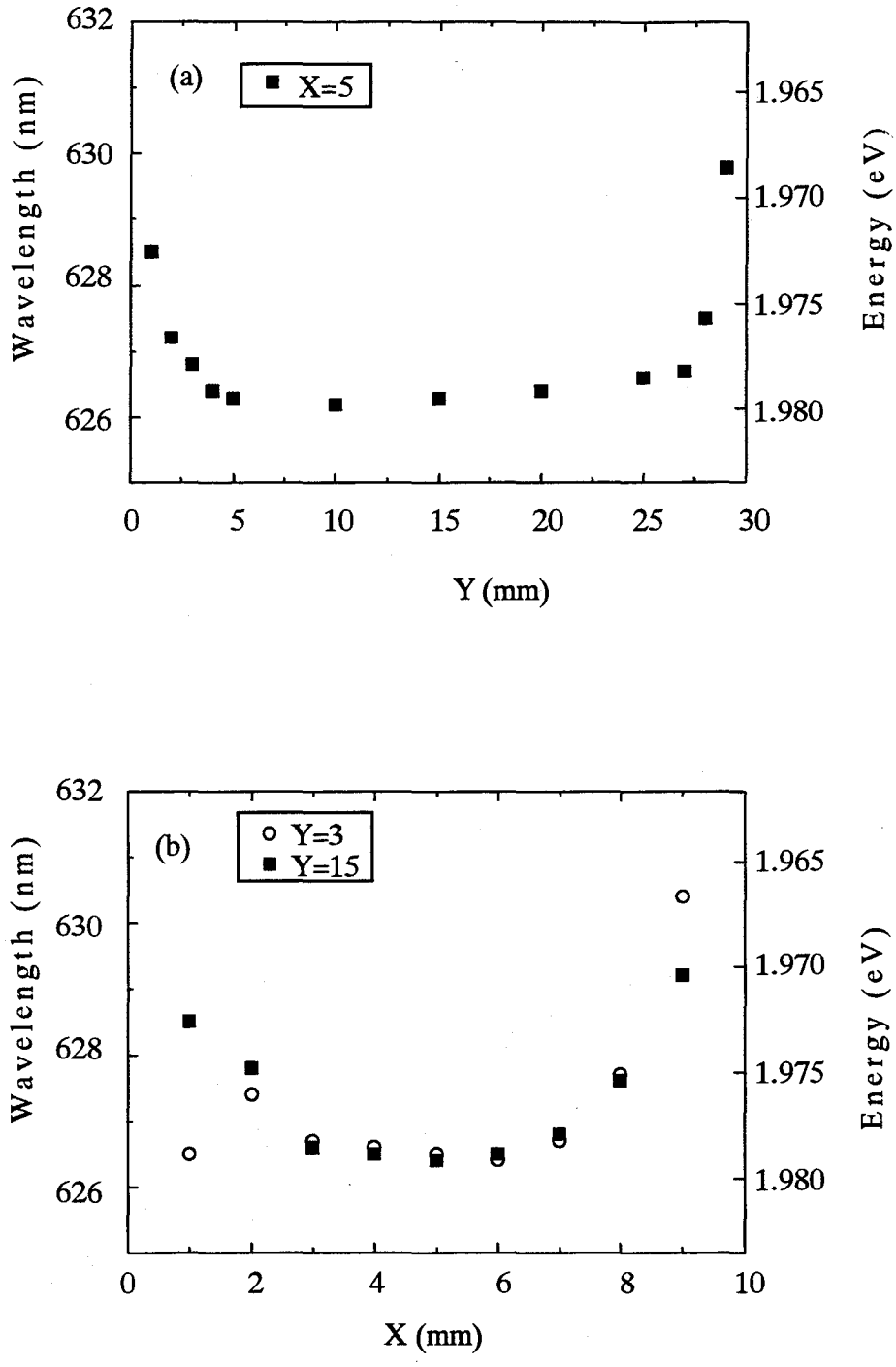
(a)
X=5
Wavelength (nm)
Energy (eV)
Y (mm)
632
630
628
626
1.965
1.970
1.975
1.980
0
5
10
15
20
25
30
(b)
Y=3
Y=15
X (mm)
2
4
6
8

Fig. 3.7

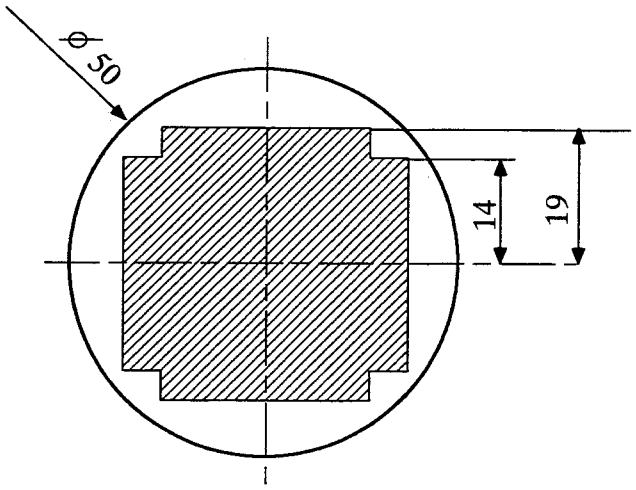

(a) type A

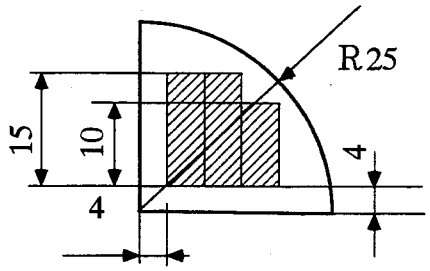

(b) type B

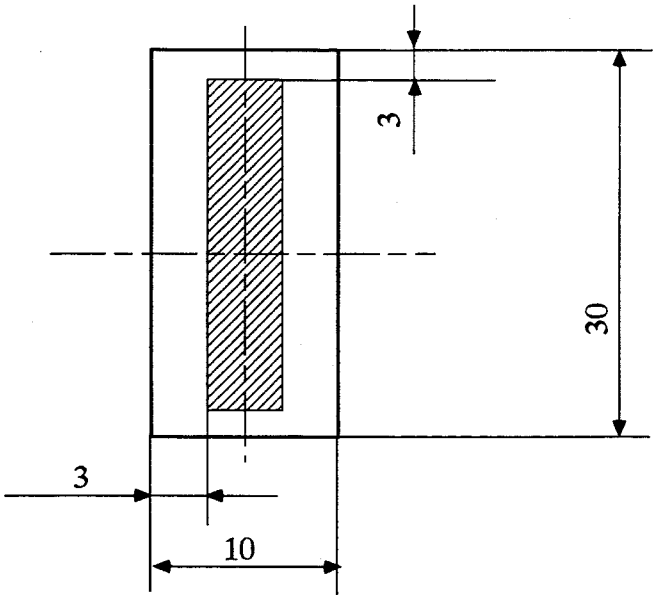

(c) type C

Fig. 3.8

Chapter IV

Temperature dependence of the Γ_c - Γ_v transition energies of the $Ga_xIn_{1-x}P$ crystals

Abstract

The excitonic Γ_c - Γ_v fundamental transition energies of disordered $Ga_xIn_{1-x}P$ (x = 0.0, 0.52, 0.70, and 1.0) crystals have been measured by photoreflectance (PR) and photoluminescence excitation (PLE) measurements at temperatures from 20 to 300 K. The PL peak energy at 20 K is found to be lower than the energy obtained from PR or PLE spectra by about 6 meV. The temperature dependence of the transition energy is expressed by a function consisting of several terms, each of which represent the effects of the volume-thermal expansion and the electron-phonon interactions. It is found that the temperature dependent decrease of the transition energy from the pure electronic transition energy is mainly caused by the electron-phonon interactions. The energy shift due to the electron-phonon interaction increases as the GaP mole fraction increases.

4.1 Introduction

In many cases AlGaInP alloys have been studied at low temperatures, i.e., 77 K or lower. The spectra obtained by optical measurements such as photoluminescence (PL) or photoreflectance (PR) reveal narrow lines: The localization of carriers in the lowest energy states and the weak electron-lattice interactions result in small broadening of energy states.[1] However, opto-electronic devices are usually operated at room temperature (RT). The lasing wavelength, for example, is determined by the fundamental Γ_c - Γ_v transition energy (E_{cv}^{Γ}) at the operating temperature. Thus the temperature dependence of E_{cv}^{Γ} has been studied by many workers. [2)-6)]

Two formulas have been proposed to express the temperature (T) dependence. The first is Varshni's empirical formula. [2)]

$$E_{cv}^{\Gamma}(T) = E_0 - \frac{\zeta T^2}{T + \theta_v}. \tag{4-1}$$

Here among the constants E_0, θ_v and ζ, θ_v is related to the Debye temperature. The other is proposed by Allen and Cardona, [3)] and has been applied to III-V compounds such as GaAs [4)] and InP. [5)]

$$E_{cv}^{\Gamma}(T) = E_a - E_b\left(\frac{1}{e^{\theta_p/T} - 1} + \frac{1}{2}\right), \tag{4-2}$$

where E_a, E_b, and θ_p (the phonon temperature) are constants. The second term in the right hand side expresses the electron-phonon interaction effect. For InP Lautenshlager *et al.* obtained $E_{cv}^{\Gamma}(T)$ from the measurement of spectroscopic ellipsometry in the temperature range of 30 - 450 K. [5)] They found that the apparent phonon temperature θ_p is 697 (±177) K. Rudra *et al.* obtained $E_{cv}^{\Gamma}(T)$ from photoluminescence (PL) measurements in the temperature range of 2 - 230 K. [6)] They found θ_p of 209 (±9) K. Since eq. (4-2) neglects the effect of volume thermal expansion, the parameters E_b and θ_p thus determined may include the effects other than the pure electron-phonon interaction. In this formula, furthermore, although the effect of electron-phonon interaction is expressed only by one term, but, in reality, there are several phonon modes, the energies of which are different. The energy dispersion of the phonons in an InP crystal is shown in Fig. 4.1 as an example. [7)]

4.2 Experimental

The samples were grown by the OMVPE system. GaAs substrates with the surface orientation of (511)A and the growth temperature of 720 °C were adopted for an undoped $Ga_{0.52}In_{0.48}P$ layer with the thickness of 1.4 μm. An undoped $Ga_{0.70}In_{0.30}P$ layer with the thickness of 2.0 μm was grown at 760 °C on a (100) $GaAs_{0.61}P_{0.39}$ substrate with the misorientation of 2 ° toward $[1\bar{1}0]$. This substrate is Te doped and the electron concentration is 7×10^{17} cm^{-3}. These growth conditions prevented the generation of a long-range ordering (LRO) structure in the $Ga_xIn_{1-x}P$ alloys. The lattice mismatch of the alloy to the substrate was measured to be less than ±0.1% by the double-crystal x-ray diffractometer (XRD) using (400) diffraction at RT. Undoped GaP and InP layers (1 μm in thickness) were grown on a Si doped n-type (1 - 3×10^{18} cm^{-3}) GaP substrate at 760 °C and on a Si doped n-type (1 - 3×10^{18} cm^{-3}) InP substrate at 680 °C, respectively. The net carrier concentration N_D-N_A of undoped layers was measured to be less than 2.5×10^{15} cm^{-3}.

The PR measurements were performed at temperatures in the range of 20 to 300 K. The Franz-Kerdysh oscillation in PR spectra due to the band bending was not observed. The PR spectra of a bulk $Ga_{0.52}In_{0.48}P$ layer at 20 - 300 K are shown in Fig. 4.2(a). The photoluminescence excitation (PLE) measurement was performed at 20 K. The sample was excited by the linearly polarized excitation beam. The photoluminescence with the polarization direction perpendicular to that of the excitation beam was selected by a linear polarizer, and was observed at the wavelength of its maximum intensity (~ 622 nm) by a monochromator. This cross-polarization measurement was effective in eliminating the scattering of the incident light. The PLE spectrum of the bulk $Ga_{0.52}In_{0.48}P$ layer at 20 K is shown in Fig. 4.2(b) together with the PL and PR spectrum. In PR and PLE measurements, the spectral resolution determined by the scanning step of the wavelength was ±0.8 meV for InP, ±0.8 meV for $Ga_{0.52}In_{0.48}P$, ±1 meV for $Ga_{0.70}In_{0.30}P$, and ±1.5 meV for GaP. Appendix 4A deals with E_{cv}^{Γ} of an $Al_{0.53}In_{0.47}P$ alloy.

4.3 Results and discussion

4.3.1. Temperature dependence of the experimentally obtained Γ_c - Γ_v transition energies

E_{cv}^{Γ}s (Γ_{6c} - Γ_{8v} for bulk alloys) of $Ga_xIn_{1-x}P$ were derived from PR or PLE spectra. In a PR measurement the ratio of the modulated component of the reflectivity to the stationary reflectivity is given by [8]

$$\Delta R/R = C_\alpha \Delta\varepsilon_1 + C_\beta \Delta\varepsilon_2. \tag{4-3}$$

$$\Delta\varepsilon_i = \left[\frac{\partial\varepsilon_i}{\partial E_{rs}}\left(\frac{\partial E_{rs}}{\partial P_{ex}}\right) + \frac{\partial\varepsilon_i}{\partial \Gamma_{rs}}\left(\frac{\partial \Gamma_{rs}}{\partial P_{ex}}\right) + \frac{\partial\varepsilon_i}{\partial I_{rs}}\left(\frac{\partial I_{rs}}{\partial P_{ex}}\right) \right] P_{ex} . \tag{4-4}$$

Here $\Delta\varepsilon_1$ and $\Delta\varepsilon_2$ are the modulation of the real and imaginary parts of the dielectric function, respectively. C_α and C_β are the seraphin coefficients. $\Delta\varepsilon_i (i = 1,2)$ is given by the superposition of three components; that is, modulations of the transition energy E_{rs}, the lifetime broadening (Γ_{rs}), and the oscillator strength (I_{rs}). [8] The subscript rs indicates the transition from a valence band sublevel s to a conduction band sublevel r. P_{ex} is the excitation power. The dielectric function is described by a Lorentzian function when the electron-lattice coupling or the scattering of carriers at the heterointerface or crystal defects is negligible. Otherwise it is expressed by a Gaussian function.[1) 8)] With the assumption of the Lorentzian dielectric function and the neglect of the term for I_{rs} reflectance modulation spectra are expressed as

$$\Delta R/R(E) = \mathrm{Re}\ \{ C \exp(i\phi)[(E - E_{rs} + i\Gamma_{rs})^{-n}]\}. \tag{4-5}$$

Here ϕ and C are the phase factor and the amplitude, respectively. The value of n shows the type of the transition: $n = 2$ for the excitonic transition, and $n = 3$ for the transition at the band edge with the 2 dimensional critical point. [9) 10)] $\Delta R/R(E)$ for the Gaussian dielectric function was found to be approximated by using eq.(4-5) with n larger than 2. [10) 11)] Figure 4.2(b) shows examples of the fitted functions with $n = 2$ or 3 to the PR spectra of $Ga_{0.52}In_{0.48}P$ at 20 K. The experimental spectrum was fitted by the superposition of the functions, each representing the Γ_{6c}(r) - Γ_{8v}(s) and Γ_{6c}(r) - Γ_{7v}(s) (electron-spin-orbit split hole) transitions (See Fig. 1.2). The Γ_{6c} - Γ_{8v} transition energy is obtained as 2.001 eV both for $n = 2$ and 3, which is indicated by the arrow. The Γ_{6c} -

Γ_{7v} transition energy for the function with n = 2 and 3 is 2.107 and 2.110 eV, respectively, virtually in agreement. The PLE peak energy agrees with the Γ_{6c} - Γ_{8v} energy from the PR spectrum. The PL peak energy was smaller by 6 meV. This result suggests that the photo-generated carrier excitons are localized in lower energy states than the free exciton state. The energies obtained from the PR spectrum at higher temperatures are indicated by the arrows in Fig. 4.2(a) and are plotted in Fig. 4.3(b) against the crystal temperature. The temperature dependence of the other samples are depicted in Figs. 4.3(a) - (d). We define ΔE_{lr} as the decrease of the transition energy from 20 K to 300 K, which is shown in Fig. 4.4 as a function of E_{cv}^{Γ} at 20 K. In this figure the result of the $Al_{0.53}In_{0.47}P$ is also plotted at E_{cv}^{Γ} = 2.704 eV (see Appendix 4A). ΔE_{lr} increases linearly with E_{cv}^{Γ}. The dependence may be expressed as

$$\Delta E_{lr} = 28.0\ (\pm 4.2) \times 10^{-3} + 30.0(\pm 1.8) \times 10^{-3}\ E_{cv}^{\Gamma}\ (\text{eV}). \qquad (4\text{-}6)$$

The obtained E_{cv}^{Γ}s from the PR spectra of all the samples are concluded to be of the excitonic nature for all of the temperatures. The reason is as follows. For bulk $Ga_{0.52}In_{0.48}P$ at 20 K, the PLE spectrum in Fig. 4.2(b) shows a sharp peak characteristic to an excitonic transition, and its energy agrees with that obtained from the PR spectrum. ΔE_{lr} (90 (±3) meV) in Fig. 4.3(b) is equal to the value of the QW sample with 6 nm well width (90 (±3) meV, see Fig. 5.4(a)). If the transition energy obtained at 300 K were of a band - band nature, ΔE_{lr} of the bulk layer should be smaller than that of the QW by the exciton binding energy of 8 meV. [12] Since GaP has higher exciton binding energy, [13] the transition energies determined by the PR spectra for x = 0.7 and 1.0 are also assumed to be excitonic. Rudra *et al.* found that the exciton binding energy of InP is 5.3 meV at 4 K. [6] Turner *et al.* found the distinct excitonic peak in absorption spectra of InP up to 77 K (1.417 eV at 6 - 20 K), and estimated the excitonic transition energy at 300 K as 1.348 eV ; [14] ΔE_{lr} is 69 meV. This value agrees well with the present value of 70 meV. It is thus concluded that the transition energy obtained from a PR spectrum of InP is also of excitonic up to 300 K.

4.3.2 Electron-phonon interaction behavior

From the theoretical expression of the electron-phonon interaction terms shown in eq.(4B-4) in Appendix 4B, [3] the shift of E_{cv}^{Γ} is expressed as

$$\sum_i \sum_{\theta_{pi}} \frac{\partial E_{cv}^{\Gamma}}{\partial n_{\theta_{pi}}} \left(n_{\theta_{pi}} + \frac{1}{2} \right). \qquad (4\text{-}7)$$

Here, $n_{\theta pi}$ is the Bose-Einstein occupation factor for the phonons with mode i and the phonon temperature θ_{pi}. We may average eq.(4-7) over all of the wavevectors. I now propose an improved formula to express the temperature dependence of E_{cv}^{Γ}.

$$E_{cv}^{\Gamma}(T) = E_0 - E_v(T) - \sum_{i=1}^{m} E_i \left(\frac{1}{e^{\theta_{pi}/T} - 1} + \frac{1}{2} \right) \tag{4-8}$$

The last term corresponds to eq.(4-7). $E_v(T)$ represents the volume-thermal expansion effect.

$$E_v(T) = \int_0^T \alpha(T) \left(\frac{\partial E_{cv}^{\Gamma}}{\partial P} \right)_T V \left(\frac{\partial P}{\partial V} \right)_T dT. \tag{4-9}$$

Here, $\alpha(T)$ is the volume-thermal expansion coefficient as given by $\alpha = 3\ \alpha_{ln}$, here α_{ln} is the linear thermal expansion coefficient. Table 4-I shows the referred α_{ln}s at 300 and 10 K taken as examples. [15) 16)] α_{ln} values at other temperatures are obtained by the cubic spline interpolation using referred values at several temperatures. [15) 16)] For a $Ga_xIn_{1-x}P$ crystal, α_{ln} is obtained by linear interpolation between the values of GaP and InP. $V(\partial P/\partial V)_T$ (hereafter denoted by B) is the bulk modulus, where V and P are the volume of a unit cell and the pressure, respectively. The values of B and $(\partial E_{cv}^{\Gamma}/\partial P)_T$ at 300 K are also given from the interpolation between GaP and InP as given in Table 4-II. [17)] We assume B and $(\partial E_{cv}^{\Gamma}/\partial P)_T$ to be independent of temperature. $E_v(T)$ is obtained by substitution of these values into eq.(4-9). The temperature dependent lattice mismatch of $Ga_xIn_{1-x}P$ layers (x = 0.52 and 0.70) to the respective substrates is calculated from the difference in $\alpha_{ln}(T)$ between the epitaxial layers and the substrates to be within 0.03%; this causes the variation in $E_{cv}^{\Gamma}(T)$ less than 2 meV, which is included in $E_v(T)$. The obtained $E_v(300)$ is 11 meV for x = 0.00, 15 meV for x = 0.52, 17 meV for x = 0.70, and 19 meV for x = 1.00; $E_V(T)$ increases with x. $E_{cv}^{\Gamma}(0) - E_v(T)$ of each sample is depicted with the dashed curve in Fig. 4.3. $E_{cv}^{\Gamma}(0)$ is obtained by the fitting of the experimental points as explained later. The share of $E_v(300)$ in ΔE_{lr} is 15 - 17 % for these crystals. The remaining 83 - 87 % is attributed to the electron-phonon interaction. The energy shift due to the electron-phonon interaction is depicted by the open circles in Figs. 4.3(a) - (d). This energy shift increases with x.

$E_{cv}^{\Gamma}(T)$ was fitted by eq.(4-8) with m = 1. Figures 4.3(a) - (d) show the results

with the solid curves. The best fit parameters of θ_{p1} and E_1 are plotted in Fig. 4.5. The obtained average phonon temperatures are in the range of 180 - 250 K, which is in the temperature range of the acoustic phonon. The temperature ranges for InP and GaP are listed in Table 4-III. [7) 17)] Electron-phonon interaction strength E_1s of GaP and $Ga_{0.70}In_{0.30}P$ are larger than those of $Ga_{0.52}In_{0.48}P$ and InP. Figure 4.6 shows $E_{cv}^{\Gamma}(T)$ of $Ga_{0.70}In_{0.30}P$ at temperatures lower than 150 K. The best fit function is drawn by the solid curve. There is small but systematic disagreement between the best fit function and the experimental points. This deviation may indicate the limitation of describing the phenomena with eq.(4-8) with m = 1. For other samples the deviation is not obvious; this may be due to smaller energy shift or larger experimental errors.

The function with m = 2 is applied to $E_{cv}^{\Gamma}(T)$ of $Ga_{0.70}In_{0.30}P$. In this case i = 1 and 2 may be identified with the acoustic phonon and the optical phonon, respectively. In the fitting procedure θ_{p1}, E_0, E_1, and E_2 were fitted with a θ_{p2} value in the optical phonon temperature range of 500 - 570 K, which was obtained from the interpolation between the values of InP and GaP listed in the Table 4-IV.[7) 17)] The best fit function for θ_{p2}= 540 K is shown in Fig. 4.6 by the dashed curve as an example. The best fit parameters are: θ_{p1} = 174 K, E_1= 0.0468 eV, E_2= 0.1030 eV, E_0= 2.3105 eV. The ranges of the respective parameters of the function with smaller chi square than the best fit function with m = 1 are $0.015 \le E_1 \le 0.10$ (eV), $0 \le E_2 \le 0.16$ (eV), $85 \le \theta_{p1} \le 250$ (K). The sum of E_1 and E_2 are found to be in the range of 0.1 - 0.2 eV. This result suggests that (1) even though the obtained apparent phonon temperature by the use of m = 1 is in the acoustic phonon temperature range, the interaction with optical phonon may affect the energy shift, and that (2) both of the sum of the interaction strength E_1 and E_2 are smaller than 0.2 eV, which is consistent with E_1 for m = 1.

Appendix 4A Temperature dependence of the Γ_{6c} - Γ_{8v} transition energy of the $Al_{0.53}In_{0.47}P$ alloy

$Al_{0.53}In_{0.47}P$ has the largest E_{cv}^{Γ} among the AlGaInP alloys that are lattice matched to GaAs substrates. Quaternary alloys of AlGaInP which is lattice matched to GaAs are the compounds of $Al_{0.53}In_{0.47}P$ and $Ga_{0.52}In_{0.48}P$. We compare the temperature dependence of E_{cv}^{Γ} of $Al_{0.53}In_{0.47}P$ with those of $Ga_xIn_{1-x}P$ alloys.

Figure 4A.1 shows the $E_{cv}^{\Gamma}(T)$ obtained from PR spectra. E_{cv}^{Γ} at 20 K (2.704 eV) is slightly smaller than that of GaP by 160 meV. ΔE_{lr} is 112 meV, which is consistent with E_{cv}^{Γ} dependence of ΔE_{lr} for $Ga_xIn_{1-x}P$ (Fig. 4.4). When the $Al_{0.53}In_{0.47}P$ alloy is compared with the $Ga_{0.52}In_{0.48}P$ alloy, ΔE_{lr} of the former crystal is larger than that of the latter by 20 meV. The volume thermal-expansion effect of $Al_{0.53}In_{0.47}P$ is estimated to agree with that for $Ga_{0.52}In_{0.48}P$ within a few meV(Chap.VI and ref.13). Thus, it is concluded that the disagreement in ΔE_{lr} is mainly caused by the difference in the electron-phonon interaction effect.

Appendix 4B Theoretical expression of the transition energy shift due to electron-phonon interaction

Consider a crystal with atoms of species γ which occupy sites $\boldsymbol{R}(l, \gamma)$ and have displacements $\boldsymbol{u}(l, \gamma)$ from equilibrium. Here l labels the unit cells. The electron-atom interaction potential $V(\boldsymbol{r}-\boldsymbol{R}(l,\gamma)-\boldsymbol{u}(l,\gamma))$ is Taylor expanded about the positions $\boldsymbol{u}(l, \gamma) = 0$. The one-electron state $|\boldsymbol{k}\, n_b\rangle$ and band energies $E_0(\boldsymbol{k}, n_b)$ are given by the zero-th order Hamiltonian H_0. Here, $\boldsymbol{k}$ and n_b are the wavevector and the band index for electrons. The first two terms of the expansion of $V(\boldsymbol{r}-\boldsymbol{R}(l,\gamma)-\boldsymbol{u}(l,\gamma))$ in powers of $\boldsymbol{u}(l, \gamma)$ are

$$H_1 = \sum_{l,\gamma} \frac{\partial V}{\partial R_\alpha(l,\gamma)} u_\alpha(l,\gamma), \tag{4B-1}$$

$$H_2 = \frac{1}{2} \sum_{l,l',\gamma,\gamma'} \frac{\partial^2 V}{\partial R_\alpha(l,\gamma)\partial R_\beta(l',\gamma')} u_\alpha(l,\gamma) u_\beta(l',\gamma') \tag{4B-2}$$

The subscripts α and β denote the Cartesian components, which are summed when

repeated. The phonon energies are assumed to be small in comparison with the relevant scale of electronic energies. The band energy except for the volume-thermal expansion effect is obtained using the perturbation theory as

$$E(\boldsymbol{k},n_b) = E_0(\boldsymbol{k},n_b) + \langle \boldsymbol{k},n_b | (H_1 + H_2) | \boldsymbol{k},n_b \rangle + \sum_{\boldsymbol{k}',n'}{}' \frac{|\langle \boldsymbol{k}',n_b' | H_1 | \boldsymbol{k},n_b \rangle|^2}{E_0(\boldsymbol{k},n_b) - E_0(\boldsymbol{k}',n_b') + i\eta}$$
$$= E_0(\boldsymbol{k},n_b) + \Sigma^{DW} + \Sigma^{SE} \qquad (4B\text{-}3)$$

The prime on the summation indicates that the term $(\boldsymbol{k}',n_b') = (\boldsymbol{k}, n_b)$ is omitted. The first term is the unperturbed energy state. Σ^{DW} and Σ^{SE} are purely real Debye-Waller (DW) term and the self energy (SE) term, respectively. In the processes of thermal averaging, the first-order correction term from H_1 vanishes because $\boldsymbol{u}(l, \gamma)$ in the harmonic approximation vanishes when averaged. The following expression is obtained from the translational invariance of the energy state .

$$E(\boldsymbol{k},n_b,T) = E_0(\boldsymbol{k},n_b) + \sum_j \sum_{q_j} \frac{\partial E(\boldsymbol{k},n_b)}{\partial n_{q_j}} \left(n_{qj} + \frac{1}{2} \right) . \qquad (4B\text{-}4)$$

$$\frac{\partial E(\boldsymbol{k},n_b)}{\partial n_{q_j}} = \frac{1}{N} \sum_{\gamma,\gamma',n'} \left[\frac{\langle \boldsymbol{k}\, n_b | \partial V / \partial R_\alpha(\gamma) | \boldsymbol{k}+\boldsymbol{q}_j\, n_b' \rangle \langle \boldsymbol{k}+\boldsymbol{q}_j\, n_b' | \partial V / \partial R_\beta(\gamma') | \boldsymbol{k}\, n_b \rangle}{E(\boldsymbol{k},n_b) - E(\boldsymbol{k}+\boldsymbol{q}_j,n_b')} \right.$$
$$\left. - \frac{\langle \boldsymbol{k}\, n_b | \partial V / \partial R_\alpha(\gamma) | \boldsymbol{k}\, n_b' \rangle \langle \boldsymbol{k}\, n_b' | \partial V / \partial R_\beta(\gamma') | \boldsymbol{k}\, n_b \rangle}{E(\boldsymbol{k},n_b) - E(\boldsymbol{k},n_b')} \right] \times$$
$$\exp\left(-i\boldsymbol{q}_j \cdot (\tau_\gamma - \tau_{\gamma'}) \right) \hbar \left(M\gamma\, M\gamma' \omega_{q_j}{}^2 \right)^{-1/2} p_\alpha(-\boldsymbol{q}_j,\gamma)\, p_\beta(\boldsymbol{q}_j,\gamma') \qquad (4B\text{-}5)$$

Here, n_{qj} is the Bose-Einstein occupation factor $(e^{k_b\theta_{pj}/k_bT}\text{-}1)^{-1}$ for the wavevector $\boldsymbol{q}_j$ with the energy $k_b\theta_{pj}$. M_γ is the mass of the γ-th atom located in the unit cell at position τ_γ. N is the number of unit cells in the crystal. $\boldsymbol{p}$ is phonon polarization vector. The first term in the large parenthesis means the SE term and the second one the DW term.

The interaction with a zone center phonon is classified into the deformation potential (DP) interaction and the piezoelectric (PE) interaction for the acoustic phonon and the optical deformation potential (OPD) interaction and the Fröhlich potential (FR) interaction for the optical phonon. [18] This is summarized in Table 4B-I. The electron-

LA phonon interaction is large for the crystals with large hydrostatic deformation potential, and has the main contribution to the DP interaction. [18] In polar crystals such as III-V compounds optical phonon causes the relative displacements of oppositely charged atoms, which generates an electric field. This interaction potential called Fröhlich potential is characteristic to the interaction with the LO phonon. The optical deformation potential interaction is caused by changes of the bond length and/or the bond angles, which are also seen in nonpolar crystals as Si. The interaction with a zone-edge or near-zone-edge phonon is characterized by the intervalley deformation potential. This interaction has no analog of the Fröhlich or piezoelectric interaction.

The respective first order interaction Hamiltonian in powers of $\boldsymbol{u}$ for small wavevectors $\boldsymbol{q}$ can be expressed as follows. For the LA phonon interaction,

$$H_{e\text{-}LA} = V_a \cdot (\boldsymbol{q}\cdot\boldsymbol{u}). \tag{4B-6}$$

Here, V_a is the hydrostatic deformation potential. For the piezoelectric interaction,

$$H_{pe} = \frac{|e|}{q^2 \varepsilon_\infty} \boldsymbol{q}\cdot\boldsymbol{e}_m(\boldsymbol{qu}), \tag{4B-7}$$

where ε_∞, $\boldsymbol{e}_m$, and $\boldsymbol{qu}$ are the dielectric function for the infinite frequency, electromechanical tensor, and strain tensor, respectively. For optical deformation potential interaction,

$$H_{e\text{-}ODP} = D_{nk}(u/a), \tag{4B-8}$$

where a and D_{nk} are, respectively, the equilibrium distance of atoms in a unit cell and the optical deformation potential for the electron with wavevector $\boldsymbol{k}$ in the band n.

$$H_{FR} = (ieF/q)\, u_{LO}$$
$$F = -\,[\,4\pi N\mu\omega_{LO}^2(\varepsilon_\infty^{-1}-\varepsilon_0^{-1})]^{1/2}, \tag{4B-9}$$

where u_{LO}, μ, ω_{LO}, ε_0 are the relative displacement between the positive and negative ions, reduced mass of the ions, and the LO phonon frequency, and the static dielectric function, respectively. For the intervalley interaction,

$$H_{iv} = \boldsymbol{p}\cdot\frac{\partial H_0}{\partial \boldsymbol{R}}u. \tag{4B-10}$$

The intervalley deformation potential D_{ij} is written as

$$D_{ij}\,u = \left\langle \boldsymbol{k}_i\ n_{bi} \left| H_{\mathrm{iv}} \right| \boldsymbol{k}_j\ n_{b\,j} \right\rangle, \qquad \text{(4B-11)}$$

$$\boldsymbol{k}_j - \boldsymbol{k}_i = \boldsymbol{q}.$$

References

1) Y.Toyozawa, Prog.Theor.Phys. 20, 53 (1958)
2) Y.P.Varshni, Physica 34, 149 (1967)
3) P.B.Allen and M.Cardona, Phys.Rev.B 23, 1495 (1981)
4) P.Lautenschlager, M.Garriga, S.Logothetidis, and M.Cardona, Phys.Rev.B 35, 9174 (1987)
5) P.Lautenschlager, M.Garriga, and M.Cardona, Phys.Rev.B 36, 4813 (1987)
6) A.Rudra, J.F.Carlin, L.Pavesi, F.Piazza, M.Proctor, and M.Ilegemes, J.Electron.Mater. 20, 1087 (1991)
7) B.Ulrici and E.Jahne, Phys.Status Solidi B 74, 601 (1976)
8) W.M.Theis, G.D.Sanders, C.E.Leak, K.K.Bajaj, and H.M.Morkoç, Phys.Rev.B 37, 3042 (1988)
9) D.E.Aspnes, Surface Sci. 37 418 (1973)
10) B.V.Schanabrook, O.J.Glembocki, and W.T.Beard, Phys. Rev. B 35, 2540 (1987)
11) O.J.Glembochi and B.V.Schanabrook, Superlattice and microstructures, 3, 235 (1987)
12) C.T.H.F.Liedenbaum, A.Valster, A.L.G.J.Severens, and G.W.`tHooft, Appl. Phys. Lett. 57 2698(1990)
13) H.Nagai, S.Adachi, and T.Fukui, III-V compound crystals, 1988, Corona Publishing Co., Ltd. Tokyo Japan
14) W.J.Turner, W.E.Reese, and G.D.Pettit, Phys.Rev. 136, A1467 (1964)
15) T.Soma, Solid.State Commun. 34, 375 (1980)
16) Properties of Indium Phosphide, EMIS data reviews series No.6, INCPEC publication
17) M.Neubuerger, Handbook of electronic materials vol.2, Electtric properties information center, New York, 1971
18) P.Y.Yu and M.Cardona, Fundamentals of Semiconductors, Springer, Berlin,1996

Table 4-I Referred linear thermal-expansion coefficients (K^{-1})

	10 K	300K
GaAs	-0.08×10^{-7}	5.7×10^{-6}
InP	2.0×10^{-7}	4.6×10^{-6}
GaP	0.1×10^{-7}	4.7×10^{-6}

refs.15 - 17

Table 4-II Referred parameters at 300 K in the calculation of $E_v(T)$

	InP	GaP
$\left(\frac{\partial E_{cv}^{\Gamma}}{\partial P}\right)_T$ (eVcm^2/dyne)	0.786×10^{-11} a)	1.07×10^{-11} b)
$\frac{1}{V}\left(\frac{\partial V}{\partial P}\right)_T$ (dyne/cm^2)	7.25×10^{11} b)	8.88×10^{11} b)

a): see Chap. VI, b): ref.17

Table 4-III Temperature ranges of acoustic phonons

	InP	GaP
TA	0 - 92 (K)	0 - 92 (K)
LA	0 - 275 (K)	0 - 305 (K)

TA: transverse acoustic phonon

LA: longitudinal acoustic phonon

InP: ref.7, GaP: ref.17

Table 4-IV Range of optical phonon temperature θ_{p2}

x	0.00	1.00
θ_2 (K)	440 - 500	525 - 595

InP: ref. 7, GaP: ref.17

Table 4B-I Summary of electron-zone-center-phonon interaction

Acoustic phonon		Optical phonon	
TA	LA	TO	LO
	DP	ODP	ODP
PE	PE		FR

Figure captions

Fig. 4.1 Dispersion curve of phonon temperature of InP. The original data of the plots is shown in the unit of cm^{-1} in ref. 6. The solid curve is the guidance for the reader's eyes. a is the lattice constant.

Fig. 4.2 (a) PR spectra of a bulk $Ga_{0.52}In_{0.48}P$ layer at temperatures from 20 to 300 K. The determined E_{cv}^{Γ}s are indicated by the arrows.
(b) Examples of the PR, PLE, and PL spectra at 20 K. The circles are experimental plots. The solid curve and the dotted curve in the PR spectrum are the fitted functions with n = 2 and 3, respectively. The obtained parameters of the Γ_{6c} - Γ_{8v} transition are $C = 4.28\times10^{-9}$, ϕ = 2.88 rad, E_{cv}^{Γ} = 2.001 eV, and Γ_{cv} = 0.009 eV for n = 2 and $C = 8.854\times10^{-11}$, ϕ = 4.46 rad, E_{cv}^{Γ} = 2.001 eV, and Γ_{cv} = 0.017 eV for n = 3, where E_{rs} and Γ_{rs} are denoted as E_{cv}^{Γ} and Γ_{cv}. The obtained Γ_{6c} - Γ_{8v} and Γ_{6c} - Γ_{7v} transition energies are indicated by arrows.

Fig. 4.3 Temperature dependence of E_{cv}^{Γ} and the shift of E_{cv}^{Γ} due to electron-phonon interaction for $Ga_xIn_{1-x}P$ crystals. (a): x = 0.00, (b): x = 0.52, (c): x = 0.70, (d): x = 1.00. The solid circles show E_{cv}^{Γ}. The open circles show the shift of E_{cv}^{Γ} due to electron-phonon interaction, which is obtained as $E_{cv}^{\Gamma}(0) - E_{cv}^{\Gamma}(T) - E_v(T)$. The dashed curves show $E_{cv}^{\Gamma}(0) - E_v(T)$. The solid curves are the best fit functions using eq.(4-8) with m = 1.

Fig. 4.4 Dependence of ΔE_{lr} on E_{cv}^{Γ}.
The circles and the square symbols are the plots for $Ga_xIn_{1-x}P$ and $Al_{0.53}In_{0.47}P$, respectively. E_{cv}^{Γ}s are obtained at 20 K

Fig. 4.5 Adjusted parameters in eq.(4-8) with m = 1.
(a) Apparent phonon temperature θ_{p1}.
(b) Coefficient of the electron-phonon interaction term E_1.

Fig. 4.6 Comparison of the fitted functions for $Ga_{0.70}In_{0.30}P$.
The spectral resolution determined by the scanning step of the wavelength is shown as the error bar. The solid curve shows the function with m = 1;. The dashed curve shows the function with m = 2; θ_1 = 174 K, θ_2 = 540 K, E_1 =

0.0468 eV, E_2 = 0.103 eV, E_0 = 2.3105 eV. The dotted curve shows the function with m = 2; θ_1 = 100 K, θ_2 = 540 K, E_1 = 0.0196 eV,E_1 = 0.162 eV, E_0 = 2.3577 eV.

Fig. 4A.1 Dependence of E_{cv}^{Γ} on temperature for the $Al_{0.53}In_{0.47}P$ alloy.

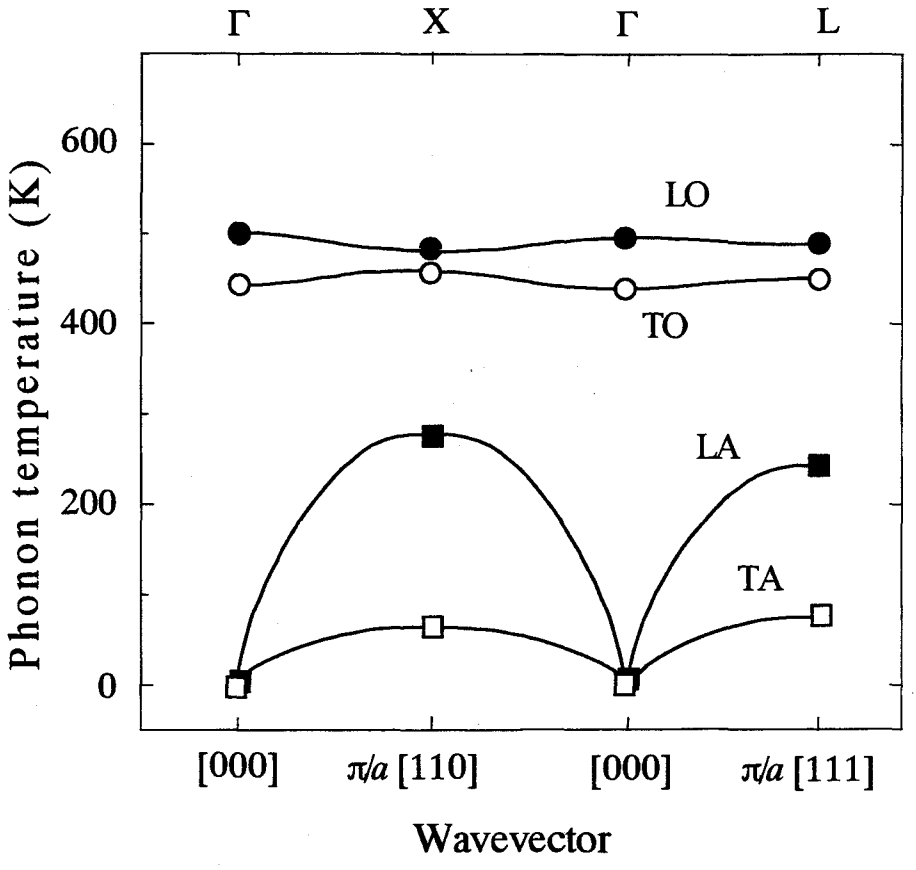
Γ
X
Γ
L
600
400
200
0
Phonon temperature (K)
LO
TO
LA
TA
[000]
π/a [110]
[000]
π/a [111]
Wavevector

Fig. 4.1

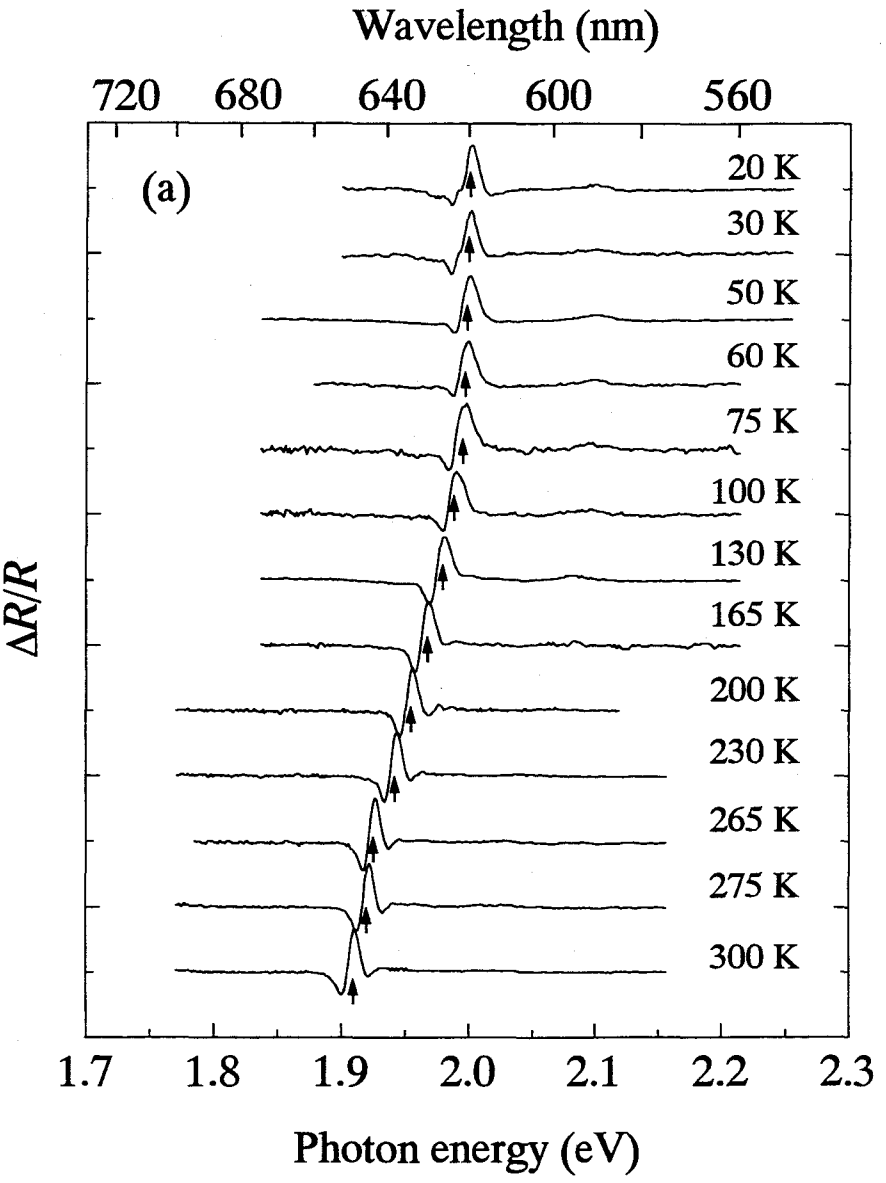
Wavelength (nm)
720
680
640
600
560
(a)
20 K
30 K
50 K
60 K
75 K
100 K
130 K
165 K
200 K
230 K
265 K
275 K
300 K
ΔR/R
1.7
1.8
1.9
2.0
2.1
2.2
2.3
Photon energy (eV)

Fig. 4.2(a)

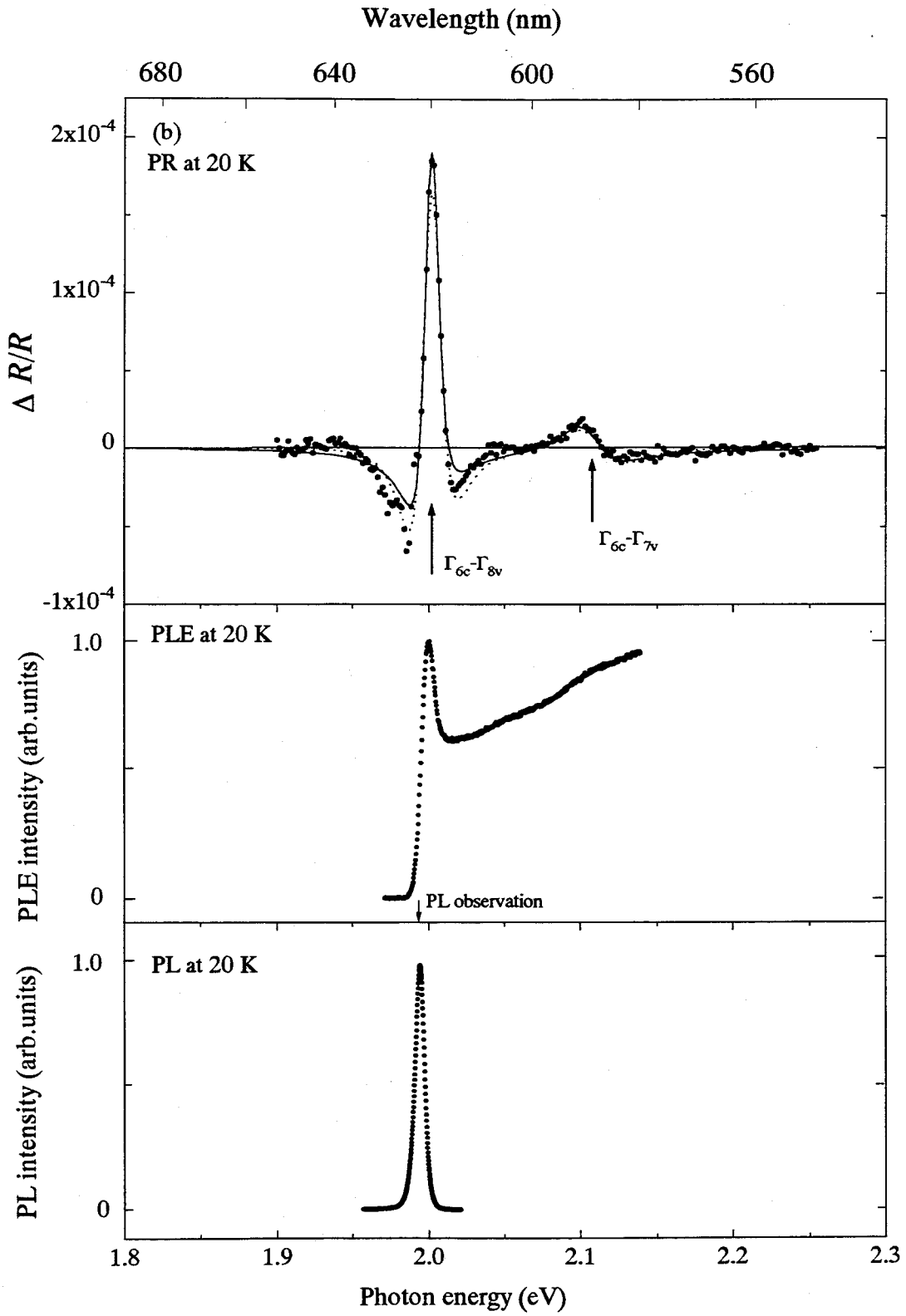
Wavelength (nm)
680
640
600
560
(b)
PR at 20 K
2x10-4
1x10-4
0
-1x10-4
Δ R/R
Γ6c-Γ8v
Γ6c-Γ7v
PLE at 20 K
1.0
0
PLE intensity (arb.units)
PL observation
PL at 20 K
1.0
0
PL intensity (arb.units)
1.8
1.9
2.0
2.1
2.2
2.3
Photon energy (eV)

Fig. 4.2(b)

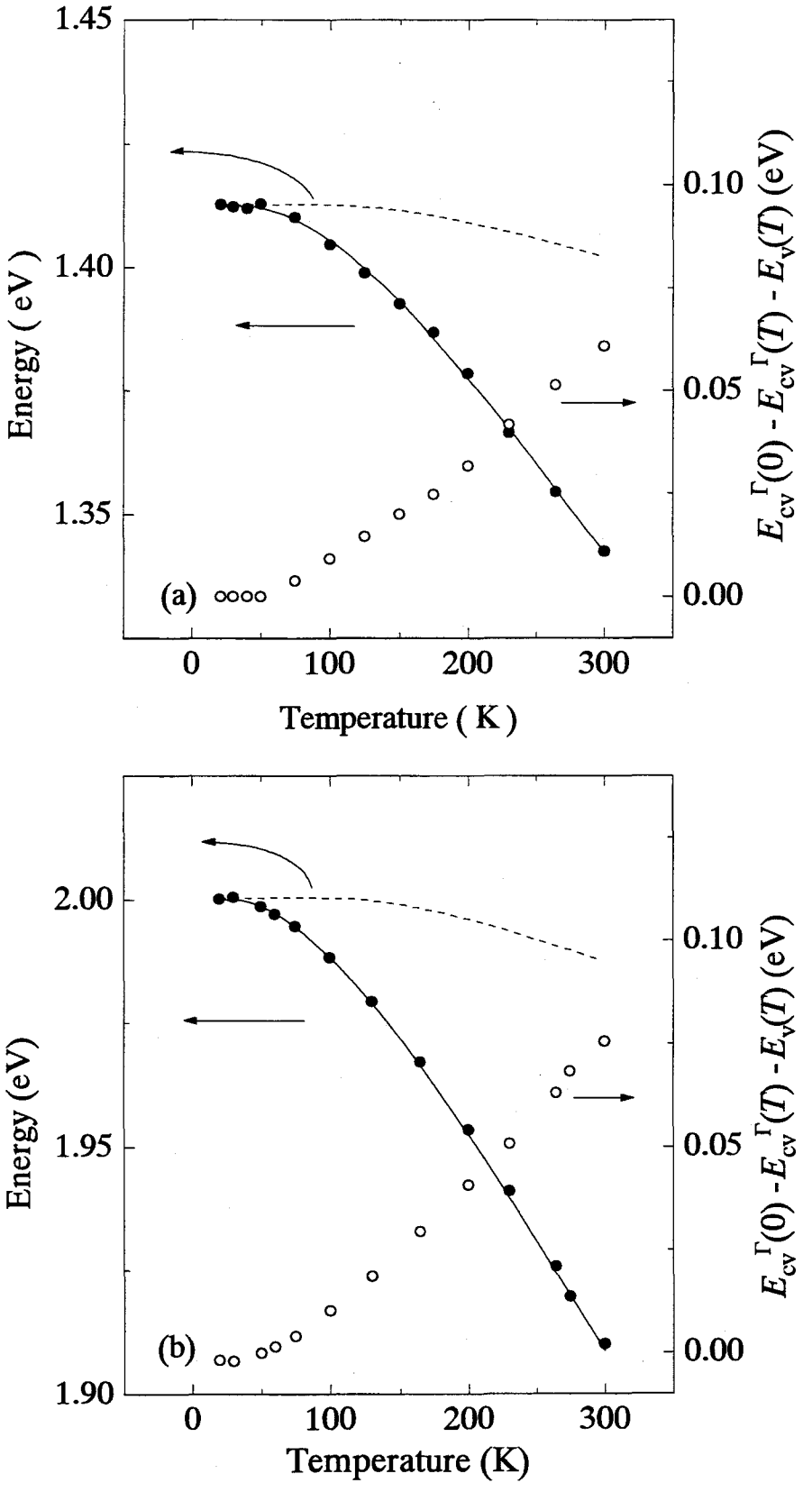
1.45
1.40
1.35
Energy (eV)
0.10
0.05
0.00
$E_{cv}^{\Gamma}(0) - E_{cv}^{\Gamma}(T) - E_v(T)$ (eV)
(a)
0
100
200
300
Temperature (K)
2.00
1.95
1.90
Energy (eV)
0.10
0.05
0.00
$E_{cv}^{\Gamma}(0) - E_{cv}^{\Gamma}(T) - E_v(T)$ (eV)
(b)
0
100
200
300
Temperature (K)

Fig. 4.3

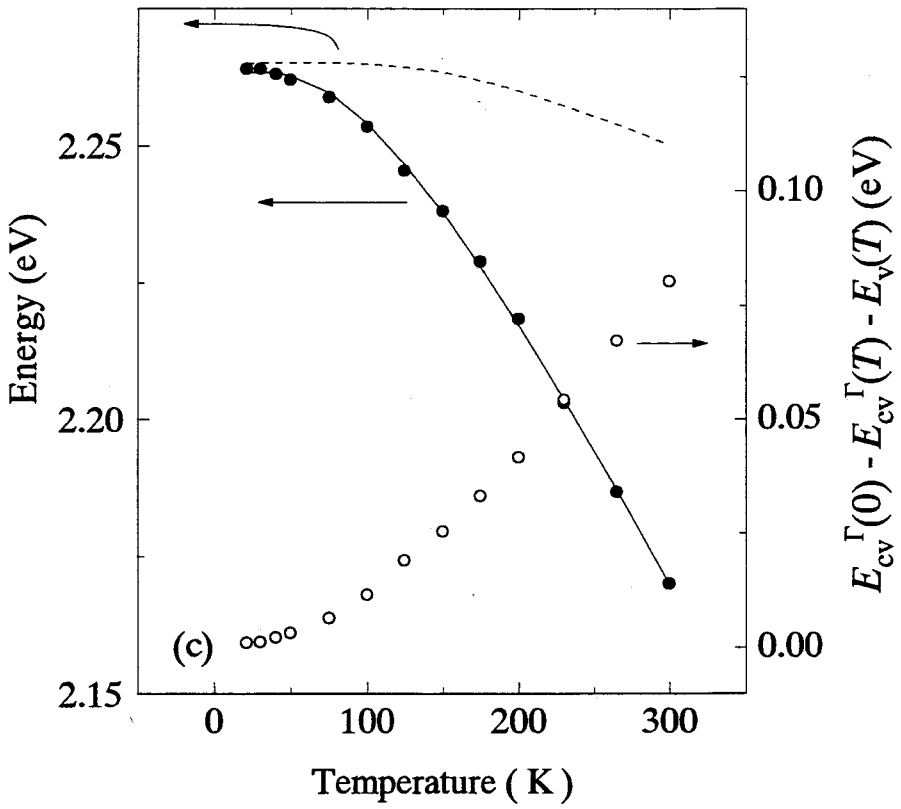
Energy (eV)
2.25
2.20
2.15
0.10
0.05
0.00
(c)
0
100
200
300
Temperature (K)
$E_{cv}^{\Gamma}(0) - E_{cv}^{\Gamma}(T) - E_v(T)$ (eV)

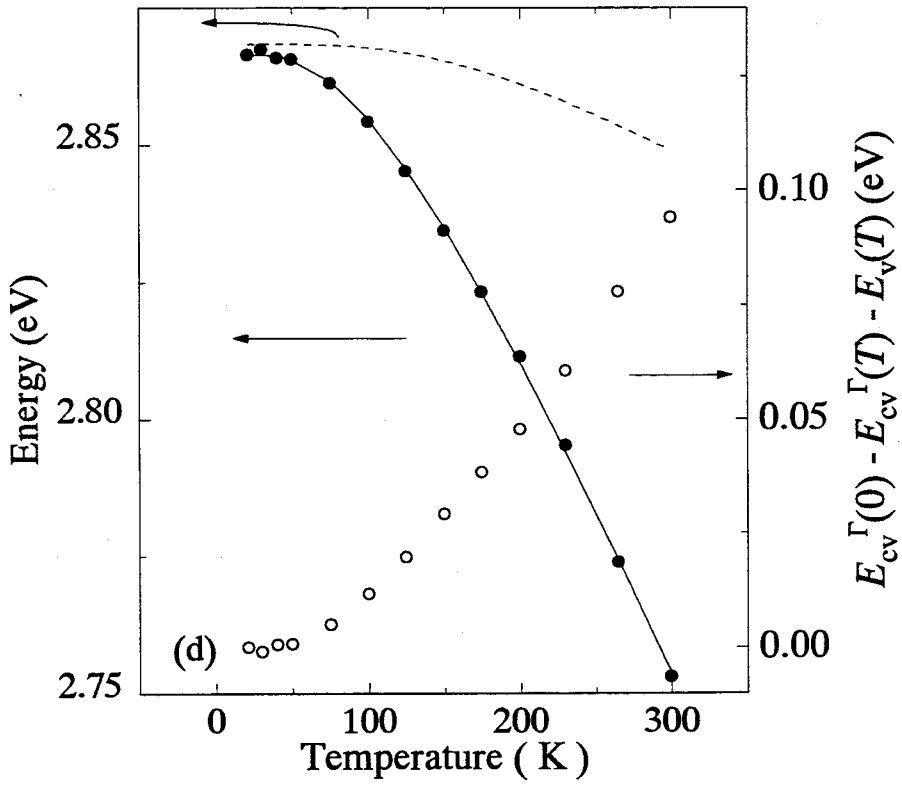
Energy (eV)
2.85
2.80
2.75
0.10
0.05
0.00
(d)
0
100
200
300
Temperature (K)
$E_{cv}^{\Gamma}(0) - E_{cv}^{\Gamma}(T) - E_v(T)$ (eV)

Fig. 4.3

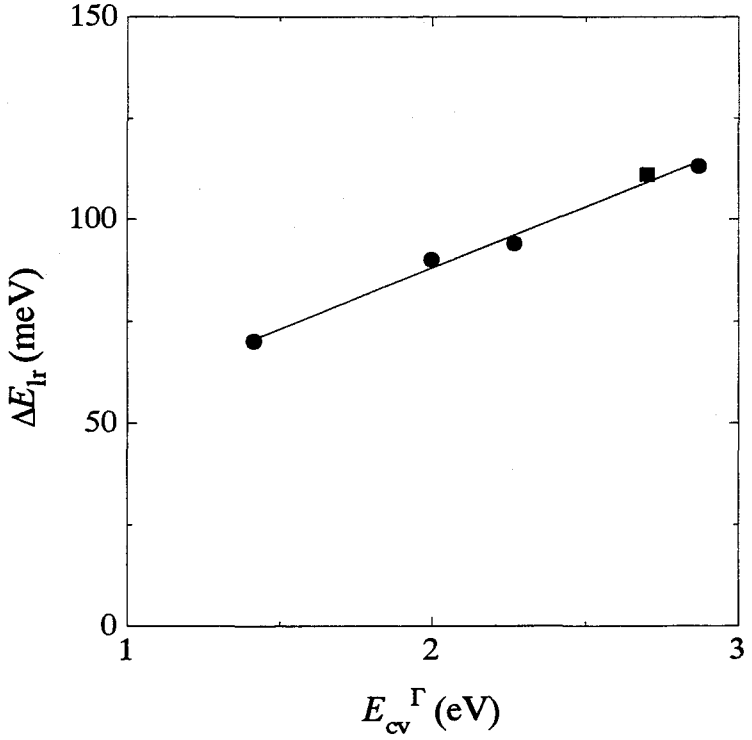

Fig. 4.4

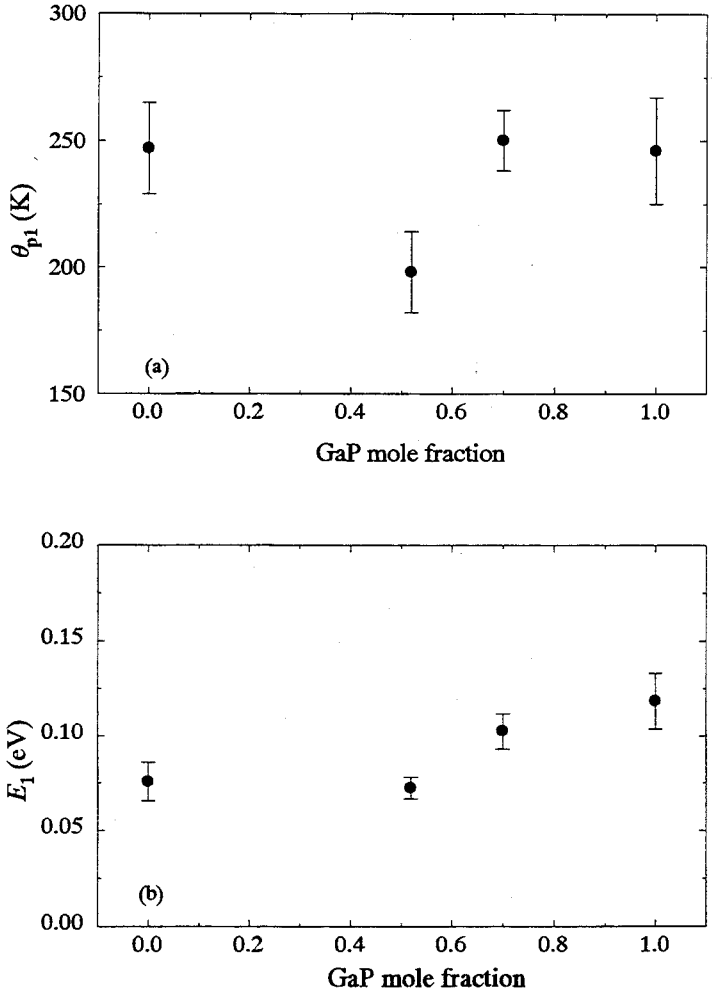
300
250
200
150
θ_{p1} (K)
(a)
0.0
0.2
0.4
0.6
0.8
1.0
GaP mole fraction
0.20
0.15
0.10
0.05
0.00
E_1 (eV)
(b)
0.0
0.2
0.4
0.6
0.8
1.0
GaP mole fraction

Fig. 4.5

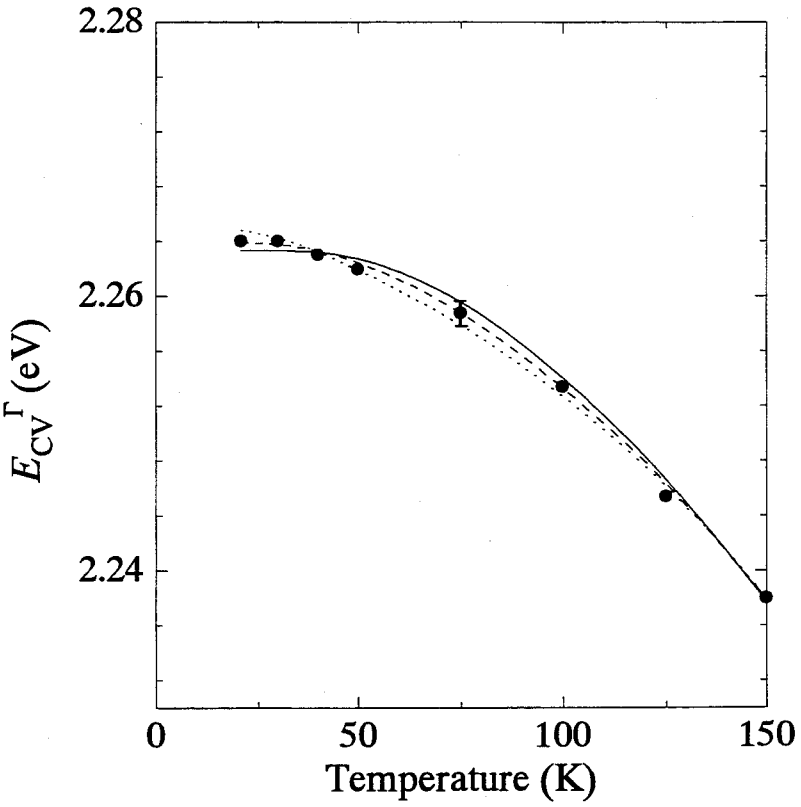

Fig. 4.6

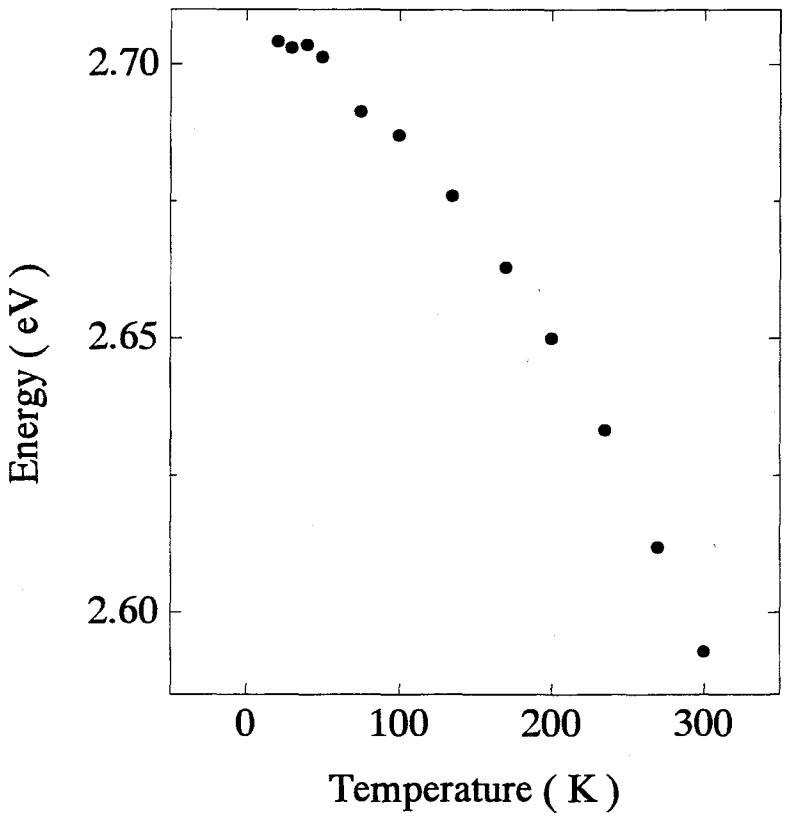

Fig. 4A.1

Chapter V

Optical processes in the $Al_{0.53}In_{0.47}P$ / $Ga_{0.52}In_{0.48}P$ / $Al_{0.53}In_{0.47}P$ quantum wells

Abstract

Photoluminescence (PL), photoluminescence excitation (PLE), and photoreflectance (PR) measurements have been conducted on the disordered $Al_{0.53}In_{0.47}P/Ga_{0.52}In_{0.48}P$(5.9 nm- or 2.0 nm-thick) /$Al_{0.53}In_{0.47}P$ quantum wells in the temperature range of 11 - 300 K. At low temperatures the PL peak energy is lower than the Γ_{6c} - Γ_{7v} (electron-heavy hole) transition energy that is derived from a PLE or PR spectrum. From the comparison of the energy difference with the calculated variation of the energy level in the QW, it is concluded that PL originates from recombinations of electron-hole pairs (excitons) in localized energy states due to the local variation of the well width by about one molecular layer. The experimentally obtained energy difference between the heavy hole and light hole states and the relative energy levels of heavy hole state in the QW (2 nm) and the Γ_{8v} level in $Al_{0.53}In_{0.47}P$ are compared with the theoretical results. It is found that the share of the band offset for the conduction band against the sum of the band offsets at the conduction and the valence bands for the bulk $Al_{0.53}In_{0.47}P$ /$Ga_{0.52}In_{0.48}P$ heterostructure is 0.73 (+0.08,–0.05).

5.1 Introduction

The band energy alignment of heterostructures of bulk alloys constitutes the basis of the state diagram of quantum well (QW) structures. The alignment is usually determined by using QWs and expressed in terms of the share of the conduction band in the band offset at the Γ point, $\Delta E_c^{\Gamma}/\Delta E_{cv}^{\Gamma}$. Here, ΔE_c^{Γ} is the band offset at the Γ_c point. ΔE_{cv}^{Γ} is the total band offset, which is the sum of the band offsets of the conduction (ΔE_c^{Γ}) and valence bands (ΔE_v^{Γ}). Several methods have been applied to obtain these values. For $(Al_{0.6}Ga_{0.4})_{0.5}In_{0.5}P/Ga_{0.5}In_{0.5}P/(Al_{0.6}Ga_{0.4})_{0.5}In_{0.5}P$-QWs Liedenbaum *et al.* observed the dependence of the photoluminescence excitation (PLE) spectra on the well width, and compared the result with the calculated ones to obtain $\Delta E_c^{\Gamma}/\Delta E_{cv}^{\Gamma} = 0.65$ (± 0.05).[1] For $Al_{0.5}In_{0.5}P/Ga_{0.5}In_{0.5}P$ heterostructure Hayakawa *et al.* obtained $\Delta E_c^{\Gamma}/\Delta E_{cv}^{\Gamma} =$ 0.39 by a similar method except that photoluminescence (PL) spectra were used in place of PLE.[2] Patel *et al.* applied a pressure on the QW of the same alloy composition and measured changes in the energy and intensity of the peak in the PL spectra against the pressure.[3] They obtained $\Delta E_c^{\Gamma}/\Delta E_{cv}^{\Gamma} = 0.52$ (±0.10).

The above observations arouse a doubt about the reliability of various standard methods in determining the transition energy. In fact, it is pointed out that, transitions involving the energy state of impurities or excitons localized in the vicinity of an impurity site could give rise to luminescence peaks with the energy smaller than that for excitons free from localization.[1] In contrast to this, a PLE spectrum, which usually reveals a much similarity to the absorption spectrum, is believed to be insensitive to the localization of the carriers under a low excitation condition.

Another point is concerning the crystal structure: e.g., the QW treated in ref. 3 has a long range ordering (LRO). It is natural to expect that characteristics, e.g., $\Delta E_c^{\Gamma}/\Delta E_{cv}^{\Gamma}$, depend on whether the crystal is ordered or disordered, but the quantitative differences are unknown so far.

The objective of this chapter is thus two-fold; first, on the basis of comparative studies to determine transition energies by various methods, i.e., PL, PLE and photoreflectance (PR), I try to assess the reliability or the limitation of these methods, particularly of PL. Secondary, for the purpose of obtaining a basic data for designing a high performance diode laser I investigate the share of the band offset of a disordered heterostructure.

5.2 Experimental details and results

Two samples studied by spectroscopic measurements were $Al_{0.53}In_{0.47}P/Ga_{0.52}In_{0.48}P/Al_{0.53}In_{0.47}P$ QWs grown by the OMVPE system. The development of LRO was prevented by adopting the (511)A surface orientation of GaAs substrates and growth temperature of 720 °C. They were of a single quantum well (SQW) with the well width of 5.9 nm (sample A) or 2.0 nm (sample B). For the purpose of comparison $(Al_{0.56}Ga_{0.44})_{0.5}In_{0.5}P$ /$Ga_{0.52}In_{0.48}P$(5.9 nm or 2.0 nm) /$(Al_{0.56}Ga_{0.44})_{0.5}In_{0.5}P$ SQWs, bulk $Ga_{0.52}In_{0.48}P$ and $Al_{0.53}In_{0.47}P$ layers were also grown. The thickness uncertainties of the QW layer for the 5.9 and 2.0 nm well width obtained from the products of the growth time and the uncertainty of the growth rate (Chap. III) are ±0.60 nm and ±0.05 nm, respectively. On the basis of the schematic image of the heterointerface structure shown in Fig. 5.1, the upper limit of the local fluctuation of a layer thickness is estimated to be 0.3 - 0.6 nm as shown in Chap. III. It is noted that 0.3 nm is close to the thickness of one molecular layer (0.28 nm). The surface region of the upper barrier layer was doped over 25 nm thickness with Zn in p-type to add the band bending in the vicinity of the surface of the epitaxial layer. The carrier concentration of the doped layers was estimated to be less than 1×10^{17} cm^{-3} from the relation between the flow rate of dimethylzinc and the carrier concentration in bulk layers measured by chemical capacitance-voltage technique. The other layers were undoped. For undoped bulk $(Al_{0.56}Ga_{0.44})_{0.5}In_{0.5}P$ and $Ga_{0.52}In_{0.48}P$ layers the carrier concentration was found to be 3×10^{15} cm^{-3} of the n-type.

The PL measurements were performed using the 476.5 nm line of the Ar^+ laser for QW samples or the 325.4 nm line of the He-Cd laser for the bulk $Al_{0.53}In_{0.47}P$ layer. The laser power was kept as low as possible (20 mW/cm^2) so as to avoid the peak energy shift and broadening. The beam was chopped at 300 Hz. An example of the results is shown in Fig. 5.2(a) for sample A at T = 12 K. Sample A and a similar SQW without doping showed no difference, suggesting that the Zn-doping in the surface layer does not affect the electron-hole recombination process.

In Figs. 5.2(b) and (c) the respective PLE (18 K) and PR (20 K) spectra of sample A are shown as examples. The Franz-Keldysh oscillation due to the band bending is not observed in the PR spectra. The PR spectra at the band edge of QWs are fitted by the superposition of two functions expressed by eq.(4-5) with n of 2 or 3. The two components are identified with the Γ_{6c} - Γ_{7v} (e-hh) and Γ_{6c} - $\Gamma_{6v(2)}$ (e-lh) transitions, respectively. The lowest transition energy at the Γ point (E_{cv}^{Γ}) is the e-hh transition. An example of the fitted functions is shown in Fig. 5.2(c). The respective transition

energies are found to be 2.068 and 2.088 eV. The PLE peaks in Fig. 5.2(b) at 2.068 (±0.0010) and 2.090 (±0.0015) eV are thus identified with the e-hh and e-lh recombinations, respectively. It is noted that the peak position of the PL spectrum is lower than the e-hh energy by 10 meV. The dependence of the PR spectra on crystal temperature is depicted in Fig. 5.3. These PR spectra were analyzed similarly, and the obtained e-hh and e-lh transition energies are shown with the arrows in Fig. 5.3. The temperature dependences of the energies are plotted in Fig. 5.4 by the closed symbols.

Figure 5.5 shows the temperature dependence of the PL spectra. Sample A has a sharp single peak (peak A) at low temperatures, while at temperatures higher than 100 K it has the broad tail toward the higher energy side. The tail may be identified as the superposition of the spectra for higher energy transitions such as the e-lh transition. Sample B shows a sharp peak at 2.21 eV (peak B_1) and a small broad peak located at its lower energy side in the temperatures range of 10 - 50 K. Above 65 K, as the temperature increases, the sharp peak diminishes, while another broad peak at 2.13 eV and a higher energy peak at around 2.25 eV (peak B_2) appear, and finally the highest one survives with its energy decreasing. The sharp peaks located around 2.0 - 2.03 eV are noises. At around 75 K the multi-peak structure appears, suggesting that at least 2 transition processes are involved. The PL peak energies for samples A and B are plotted in Fig. 5.4(a) (peak A) and Fig. 5.4(b) (peak B_1 and B_2) with open symbols. Time resolved PL measurements were performed at 15 K using the 488.0 nm line of the Ar^+ laser with the pulse duration of 30 ns for samples A and B for the purpose of studying the difference in the electron-hole recombination rates. Figure 5.6 shows the temporal development of the PL intensity. For sample A the PL intensity at peak A decayed faster than the time resolution of 30 ns. For sample B the lifetime at peak B_1 is hundreds of ns. The long decay time is the characteristic feature of an indirect transition type. In fact, similar profile of the spectra to Fig. 5.5(b) is observed for the semiconductors of the indirect transition nature, [4) 5)] and is also shown for AlGaInP alloys of the indirect transition nature (Appendix 5).

5.3 Discussion

5.3.1 Nature of the PL signals

The band energy alignment of $Al_{0.53}In_{0.47}P/Ga_{0.52}In_{0.48}P(2nm)/Al_{0.53}In_{0.47}P$-QW is schematically depicted in Fig 5.7. Both of the band offsets ΔE_c^{Γ} and ΔE_v^{Γ} are assumed to be positive. [6)] The PL peak at 2.215 eV (peak B_1) is assigned to the $Al_{0.53}In_{0.47}P$ X_c -

$Ga_{0.52}In_{0.48}P$ Γ_v transition, because its energy is lower than 2.347 eV of the X_{6c} - Γ_{8v} transition in $Al_{0.53}In_{0.47}P$, and this transition has the indirect transition nature. In the spectrum at 12 K, the energy difference between the sharp peak B_1 and the broad and small peak at 2.17 eV is about 40 meV, which agrees well with the phonon energy shown in Appendix 5. Therefore it is concluded that the peak B_1 is for no-phonon transition and that the smaller peak is for phonon-assisted one. This no-phonon transition can take place owing to the violation of the wavevector ($\boldsymbol{k}$)-selection rule for electrons which is caused by the penetration of the X_{6c} wavefunction of the $Al_{0.53}In_{0.47}P$ layers into the $Ga_{0.52}In_{0.48}P$ well or the scattering of carriers at the interfaces between the $Al_{0.53}In_{0.47}P$ and the $Ga_{0.52}In_{0.48}P$ layers. The peak located around 2.14 eV at 50 - 100 K is estimated to originate from the phonon assisted transition enhanced by the increase of temperature.

Since the peak B_2, which is dominant at high temperatures, appears at 75 K, this peak is assigned to a transition different from peak B_1. The former is assigned to recombinations of e-hh excitons in the well which are localized in lower energy states in the vicinity of the Γ point. The candidates of the origin of the localization energy are (1) the local fluctuation of the well width and the resultant variation of the energy levels in the well, (2) the spatial fluctuation of the alloy composition in the well or the barrier layer and the resultant variation of the energy levels in the well, and (3) the localization of excitons in the vicinity of impurities or defects. First, I examine (1); The difference between the PL peak energy and the transition energy obtained from PR spectra for the QWs is shown in Table 5-I. The difference becomes larger as the well width becomes smaller, and as the band offset between the well and the barriers becomes larger. The energy levels in QWs are calculated with the square potential well model and the effective mass approximation. The adopted effective masses are listed in Table 5-II. [1)] It is assumed that $\Delta E_c^{\Gamma}/\Delta E_{cv}^{\Gamma}$ is 0.73 for the $Al_{0.53}In_{0.47}P$ barrier, which is shown later, and 0.65 for the $(Al_{0.56}Ga_{0.44})_{0.5}In_{0.5}P$ barrier. [1)] The local fluctuation of the well width was assumed to be one molecular layer, i.e., 0.28 nm. The calculated variation of the transition energy is listed in the Table 5-III. These values agree well with the experimentally obtained differences. Next, the candidate (2); From the difference between the PL peak energy and the PLE peak energy of a bulk $Ga_{0.52}In_{0.48}P$ sample (Fig. 4.2 in Chap.IV) the exciton localization energy is estimated to be about 6 meV. With the assumption that E_{cv}^{Γ} of the $Al_{0.53}In_{0.47}P$ layer has the same variation, the fluctuation of the quantized energy level is calculated to be 1 to 2 meV. As for candidate (3) the localization energy should be independent of the well width. Thus I conclude that peak A and peak B_2 in PL spectra originate from the e-hh transitions, and that the deviation of a PL peak energy from E_{cv}^{Γ} determined by a PR measurement is ascribed to the

fluctuation of well width by one molecular layer. In the schematic illustration of the heterostructure shown in Fig. 5.1, the exciton radius varies owing to the fluctuation of well width. This leads to the broadening of the energy levels. The shift of the PL peak toward the PR transition energy with an increase in temperature is ascribed to the occupation of the higher energy states in the well.

5.3.2 Share of the band offset for the conduction band at the Γ point

The energy difference between hh and lh states (ΔE_{lh}) is obtained to be 22 (±2) meV for sample A and 45.3 (±8) meV for sample B from the respective PR spectrum at 20 K. ΔE_{lh} is calculated using the square potential well model. The results are plotted in Fig. 5.8(a) as a function of $\Delta E_c^{\Gamma}/\Delta E_{cv}^{\Gamma}$. The closed squares and circles are for sample A and sample B, respectively. The error ranges of the plots are calculated as the variation of the QW energy levels due to the fluctuation of the well width of 0.28 nm. For the purpose of comparison with other reports, the $\Delta E_c^{\Gamma}/\Delta E_{cv}^{\Gamma}$ range is from 0.5 to 0.8. The experimental ΔE_{lh} for sample B leads to $\Delta E_c^{\Gamma}/\Delta E_{cv}^{\Gamma}$ of 0.72 - 0.81. The energy difference between the vertex of the $Al_{0.53}In_{0.47}P$ valence band and the hh state in the well (ΔE_v^{bw}) of sample B is obtained from the subtraction of the transition energy of $Al_{0.53}In_{0.47}P$ X_c - $Ga_{0.52}In_{0.48}P$ Γ_v (2.215 eV) from that of $Al_{0.53}In_{0.47}P(X_c - \Gamma_v)$ (2.347 eV), and is found to be 132 (±4) meV. Here, the difference in the electron-hole interaction potential energy between an $Al_{0.53}In_{0.47}P$ X_c - $Ga_{0.52}In_{0.48}P$ Γ_v pair and an $Al_{0.53}In_{0.47}P$ X_c - Γ_v pair is neglected. ΔE_v^{bw} is also calculated using the square potential well model, and plotted in Fig. 5.8(b). This figure leads us to $\Delta E_c^{\Gamma}/\Delta E_{cv}^{\Gamma}$ of 0.68 - 0.74. Thus I determine $\Delta E_c^{\Gamma}/\Delta E_{cv}^{\Gamma}$ to be 0.73 (+0.08,–0.05). It may be added that the most plausible value is in the 0.72 - 0.74 range. This is slightly larger than 0.65 (±0.05) for the $(Al_{0.6}Ga_{0.4})_{0.5}In_{0.5}P/Ga_{0.5}In_{0.5}P$-heterostructure obtained by Liedenbaum *et al.* [1] The result of Hayakawa *et al.* (0.39) [2] is smaller than the present result. This is probably because they adopted the PL method to measure E_{cv}^{Γ} of QW structures. The present share is larger than that obtained by Patel *et al.* (0.52 (±0.1)) [3] on the ordered sample, for which there exist additional factors such as antiphase domain boundary, [7] larger compositional fluctuation, pronounced step bunching [8] and so on, which can locally modify the band structure. It may be interesting to investigate the effect of LRO on $\Delta E_c^{\Gamma}/\Delta E_{cv}^{\Gamma}$ value as a future subject.

Appendix 5 Transition energies of the bulk $(Al_{0.53}In_{0.47}P)_z$ $(Ga_{0.52}In_{0.48}P)_{1-z}$ alloys

Undoped single layers of $Al_{0.53}In_{0.47}P$ (500 nm in thickness), $(Al_{0.53}In_{0.47}P)_z$ $(Ga_{0.52}In_{0.48}P)_{1-z}$ (z = 0.41, 0.46, 0.56, 0.71) (500 nm - 1μm) on (511)A substrates, and an undoped InP layer (1μm) on an n-type ($1\text{-}3\times10^{18}$ cm^{-3}) InP substrate with (100) surface orientation were grown. Lattice mismatch of the ternary and quaternary alloys to GaAs substrates was found to be within ± 0.05% from the XRD measurements. $(Al_{0.53}In_{0.47}P)_z$ $(Ga_{0.52}In_{0.48}P)_{1-z}$ is denoted by $(Al_zGa_{1-z})_{0.5}In_{0.5}P$ as the conventional notation.

The examples of the PL spectra of single layers, $(Al_{0.71}Ga_{0.29})_{0.5}In_{0.5}P$ and $Al_{0.53}In_{0.47}P$, at 12 K are shown in Fig. 5A.1(a). A sharp peak (peak C) and a broad one are shown for both layers. The energies of the sharp peaks in the $(Al_{0.71}Ga_{0.29})_{0.5}In_{0.5}P$ and $Al_{0.53}In_{0.47}P$ layers are 2.326(±0.002) eV and 2.347(±0.002) eV, respectively. The energies of the broad peaks are 2.280 and 2.292 eV for $(Al_{0.71}Ga_{0.29})_{0.5}In_{0.5}P$ and 2.300 eV for $Al_{0.53}In_{0.47}P$. The similar PL spectra were obtained for the alloys with $z \geq 0.56$. Figure 5A.1(b) shows the transition energies for $(Al_zGa_{1-z})_{0.5}In_{0.5}P$ layers obtained by the PL, PLE, or PR measurement. Note that the energies of peak C are smaller than the E_{cv}^{Γ}s obtained from PR spectra at 20 K: 2.454 eV for the $(Al_{0.71}Ga_{0.29})_{0.5}In_{0.5}P$ layer and 2.704 eV for the $Al_{0.53}In_{0.47}P$ layer. The difference between the transition energy of Γ_{6c} - Γ_{8v} and that of the PL peak C reduces to zero as y decreases. The shape of the PL spectra is typical of indirect transition alloys. [4) 5)] Yamashita *et al.* observed the transient PL with the pulse excitation by an Ar^+ laser with the duration of 30 ns for an $(Al_{0.5}Ga_{0.5})_{0.5}In_{0.5}P$ alloy, and obtained the long PL decay component of 1.56 μs at 15 K. [9)] This decay time is larger than the exciton recombination lifetime of $Ga_{0.52}In_{0.48}P$ alloys by several orders. [10)] From these facts the PL peaks are ascribed to indirect transitions. The energy differences between the sharp and broad peaks in the PL spectra agree fairly well with the phonon energies obtained by Raman scattering measurements: 52 to 57 meV for AlP-like phonon modes and 39 to 43 meV for InP-like phonon modes. [11) - 13)] Since in indirect $(Al_zGa_{1-z})_{0.5}In_{0.5}P$ alloys the lowest critical point in the conduction band is the X_c point,[9) 14)] it is concluded that peak C is assigned to the X_c - Γ_v transition without absorption or emission of phonons (no-phonon transition) and the broad peak to the superposition of phonon-assisted transitions. The presence of the no-phonon transition may be ascribed to the transfer of $\boldsymbol{k}$-vector of carriers by the scattering at positions with potential irregularities such as crystal defects or the local fluctuation of alloy composition. From the fitting of linear functions to the Γ_{6c} - Γ_{8v} and X_{6c} - Γ_{8v} transition energies, the X_c - Γ_c crossing point at 20 K is estimated to be z of 0.48 (±0.04).

References

1) C.T.H.F.Liedenbaum, A.Valster, A.L.G.J.Severens, and G.W.`tHooft, Appl. Phys. Lett. 57 2698(1990)
2) T.Hayakawa, K.Takahashi, M.Hosoda, S.Yamamoto, and T.Hijikata, Jpn. J. Appl. Phys. 27 L1553 (1988)
3) D.Patel, M.J.Hafich, G.Y.Robinson, and C.S.Mononi, Phys. Rev. B 48 18031 (1993)
4) J.C.Strum, H.Manoharan, L.C.Lenchyshyn, M.L.W.Thewalt, N.L.Rowell, J.P.Noel, and D.C.Houghton, Phys. Rev. Lett. 66 1362 (1991)
5) S.Fukatsu, N.Usami, and Y.Shiaraki, Jpn.J.Appl.Phys. 31, L1525 (1992)
6) M.O.Watanabe and Y.Ohba, Appl.Phys.Lett. 50, 906 (1987)
7) C.S.Baxeter, W.M.Stobbs, and J.H.Wilkie, J.Cryst.Growth 112 373 (1991)
8) A.Gomyo, H.Hotta, F.Miyasaka, K.Tada, H.Fujii, K.Kobayashi, and H.Hino, The extended abstract of 7th International conference on metalorganic vapor phase epitaxy, B-3-3 p.62 (1994)
9) K.Yamashita, T.Kita, H.Nakayama, and T.Nishino, Phys.Rev.B 23, 15713 (1996)
10) P. Michler, A. Hangleiter, M. Moser, M. Geiger, and F. Scholtz, Phys. Rev. B 46, 7280 (1992)
11) M.Kubo, M.Mannoh, Y.Takahashi, and M.Ogura, Appl. Phys. Lett. 52, 715 (1988)
12) M.Kondow, S.Minagawa, and S.Satoh, Appl.Phys.Lett. 51, 2001 (1987)
13) B.Ulrici and E.JAhne, Phys. States Solidi B, 74, 601 (1976)
14) H.Asahi, Y.Kawamura, and H.Nagai, J.Appl.Phys. 53, 4928 (1982)

Table 5-I Difference between the PL peak energy and the e-hh transition energy obtained from PR spectra.

well width (nm)	$Al_{0.53}In_{0.47}P/Ga_{0.52}In_{0.48}P$	$(Al_{0.56}Ga_{0.44})_{0.52}In_{0.48}P/Ga_{0.52}In_{0.48}P$
2.0	40 meV(at 100K)	25 meV(at 20K)
5.9	10 meV(at 20K)	4 meV(at 20 K)

Table 5-II Effective masses of electrons and holes in $Ga_{0.52}In_{0.48}P$ and $Al_{0.53}In_{0.47}P$.

	$Ga_{0.52}In_{0.48}P$ [a]	$Al_{0.53}In_{0.47}P$ [b]
m_e / m_0	0.105	0.115
m_{hh} / m_0	0.48	0.54
m_{lh} / m_0	0.14	0.16

m_0: electron rest mass (9.11×10^{-31} kg) m_e: effective mass of an electron

m_{hh}: effective mass of a heavy hole m_{lh}: effective mass of a light hole

a): ref.1, b): estimation from the linear extrapolation of the data for $Ga_{0.52}In_{0.48}P$ and $(Al_{0.6}Ga_{0.4})_{0.5}In_{0.5}P$ in ref. 1.

Table 5-III Calculated fluctuation of e-hh transition energies due to the fluctuation of the well width.

well width (nm)	$Al_{0.53}In_{0.47}P/Ga_{0.52}In_{0.48}P$	$(Al_{0.56}Ga_{0.44})_{0.52}In_{0.48}P$ /$Ga_{0.52}In_{0.48}P$
2.0±0.28	± 46 meV	± 22 meV
5.9±0.28	± 6 meV	± 4 meV

Figure captions

Fig. 5.1 Image of the structure at the heterointerface between a quantum well layer and barrier layers.
The effective size of exciton is also depicted by the hatched area.

Fig. 5.2 PL, PLE, and PR spectra at 12 - 20 K for sample A.
(a) PL spectrum at 12 K.
(b) PLE spectrum at 18 K.
(c)An example of the fittings of eq.(4.5) to the experimentally obtained PR spectra. The measurement temperature is 20 K. The adopted n in eq.(4-5) is equal to 3. The dashed curves are the e-hh and e-lh transition components of the spectrum. The solid curve is the superposition of them. The obtained best fit parameters are $C = 4.07\times10^{-11}$, $E_{cv}^{\Gamma} = 2.068$ eV, $\phi = 3.5$ rad, $\Gamma_{cv} = 0.011$ eV for the e-hh transition and $C = 1.86\times10^{-11}$, $E_{cv}^{\Gamma} = 2.088$, $\phi = 2.7$ rad, $\Gamma_{cv} = 0.013$ eV for the e-lh transition.

Fig. 5.3 Dependence of PR spectra on temperature.
The transition energies of the e-hh and e-lh are indicated by arrows.
(a) Sample A (5.9 nm quantum well).
(b) Sample B (2.0 nm quantum well). The signal located at the higher energy side (2.70eV at 16 K) is from the $Al_{0.53}In_{0.47}P$ barrier layers.

Fig. 5.4 Dependence of transition energies on temperature.
(a) Sample A (5.9 nm quantum well) ○:PL peak A; ●:e-hh by PR; ■:e-lh by PR.
(b) Sample B (2.0 nm quantum well) ○:PL peak B_1 for X_c - Γ_v; □: PL peak B_2 for Γ_c - Γ_v; ●:e-hh by PR; ■:e-lh by PR.

Fig. 5.5 Dependence of PL spectra on temperature.
(a) Sample A (5.9 nm-thick quantum well). (b) Sample B (2.0 nm-thick quantum well).

Fig. 5.6 Temporal development of the PL intensity at 15 K.
(a) Sample A. PL was measured at 2.21 eV. (b)Sample B. PL was measured at 2.06 eV.

Fig. 5.7 Energy level diagram for the $Al_{0.53}In_{0.47}P/Ga_{0.52}In_{0.48}P(2.0nm)/ Al_{0.53}In_{0.47}P$-quantum well.
The measurement temperature is 10 - 20 K.

Fig. 5.8 Estimation of $\Delta E_c^{\Gamma}/\Delta E_{cv}^{\Gamma}$ at 12 K.
(a) Relationship between $\Delta E_c^{\Gamma}/\Delta E_{cv}^{\Gamma}$ and ΔE_{lh}. ■: sample A. ●: sample B.
(b) Relationship between $\Delta E_c^{\Gamma}/\Delta E_{cv}^{\Gamma}$ and ΔE_v^{bw} for sample B.

Fig. 5A.1 Results of transition energies for $(Al_zGa_{1-z})_{0.5}In_{0.5}P$ alloys.
(a) PL spectra of bulk $(Al_{0.71}Ga_{0.29})_{0.5}In_{0.5}P$ and $Al_{0.53}In_{0.47}P$ at 12 K.
The excitation power is 20 mW/ cm^2.
(b) Dependence of transition energies on alloy composition at 11 - 20 K.
The energies of the Γ_{6c} - Γ_{8v} transitions and the X_{6c} - Γ_{8v} transitions are plotted by the closed symbols and open symbols, respectively. The respective symbols of squares, triangles, and circles indicate the results of PLE, PL, and PR measurements.

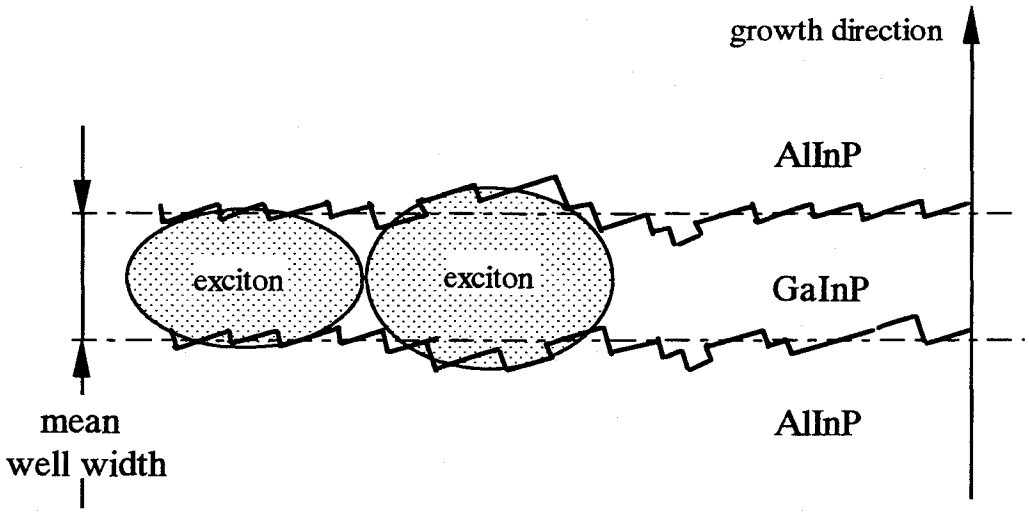
growth direction
AlInP
exciton
exciton
GaInP
AlInP
mean
well width

Fig. 5.1

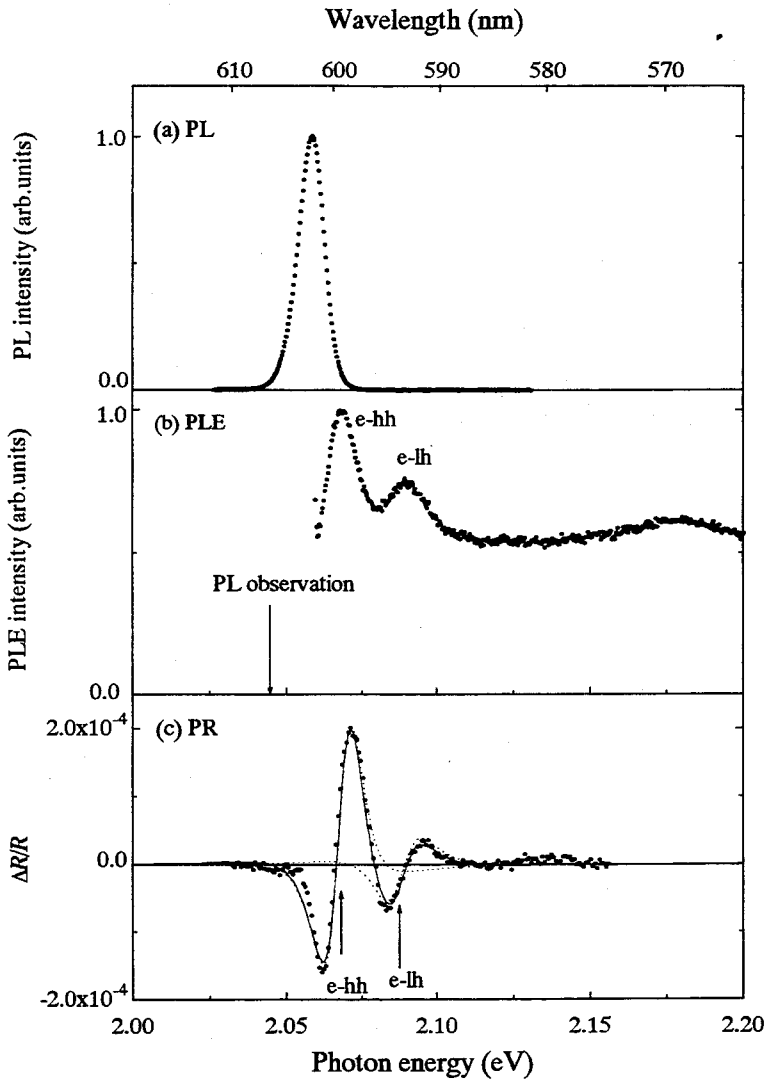
Wavelength (nm)
610
600
590
580
570
(a) PL
1.0
0.0
PL intensity (arb.units)
(b) PLE
e-hh
e-lh
PL observation
PLE intensity (arb.units)
(c) PR
2.0x10-4
0.0
-2.0x10-4
ΔR/R
e-hh
e-lh
2.00
2.05
2.10
2.15
2.20
Photon energy (eV)

Fig. 5.2

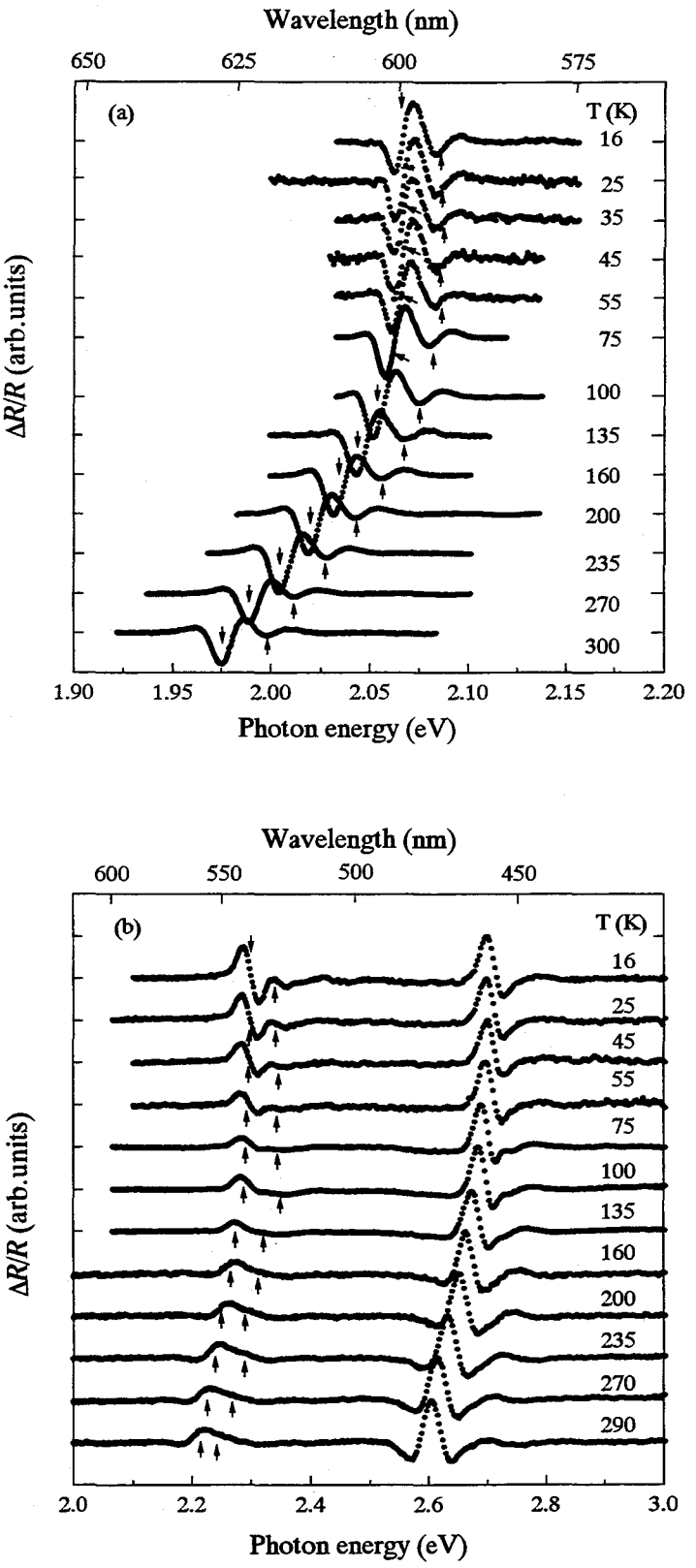
Wavelength (nm)
650
625
600
575
(a)
T (K)
16
25
35
45
55
75
100
135
160
200
235
270
300
ΔR/R (arb.units)
1.90
1.95
2.00
2.05
2.10
2.15
2.20
Photon energy (eV)
Wavelength (nm)
600
550
500
450
(b)
T (K)
16
25
45
55
75
100
135
160
200
235
270
290
ΔR/R (arb.units)
2.0
2.2
2.4
2.6
2.8
3.0
Photon energy (eV)

Fig. 5.3

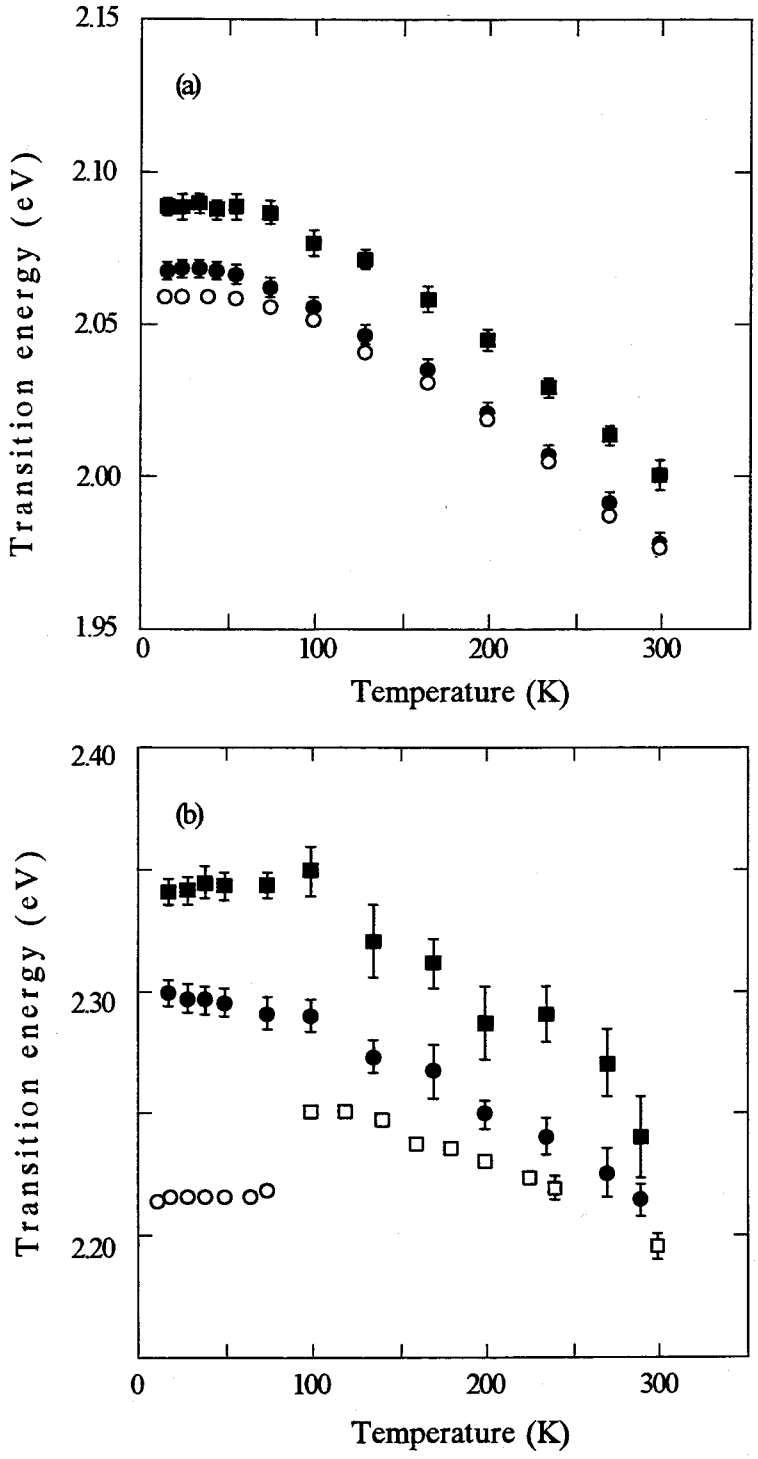
(a)
Transition energy (eV)
2.15
2.10
2.05
2.00
1.95
0
100
200
300
Temperature (K)
(b)
Transition energy (eV)
2.40
2.30
2.20
0
100
200
300
Temperature (K)

Fig. 5.4

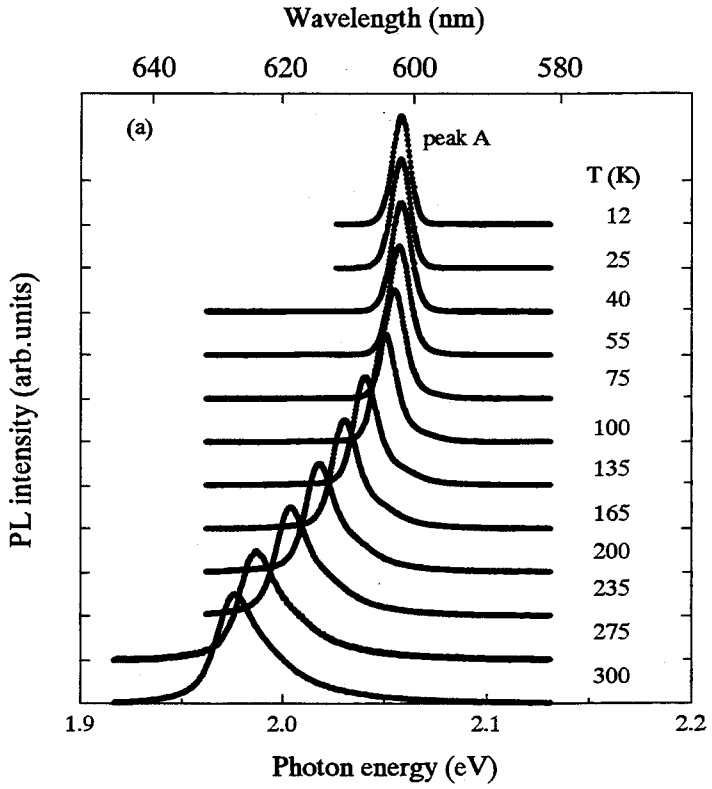
Wavelength (nm)
640
620
600
580
(a)
peak A
T (K)
12
25
40
55
75
100
135
165
200
235
275
300
PL intensity (arb.units)
1.9
2.0
2.1
2.2
Photon energy (eV)

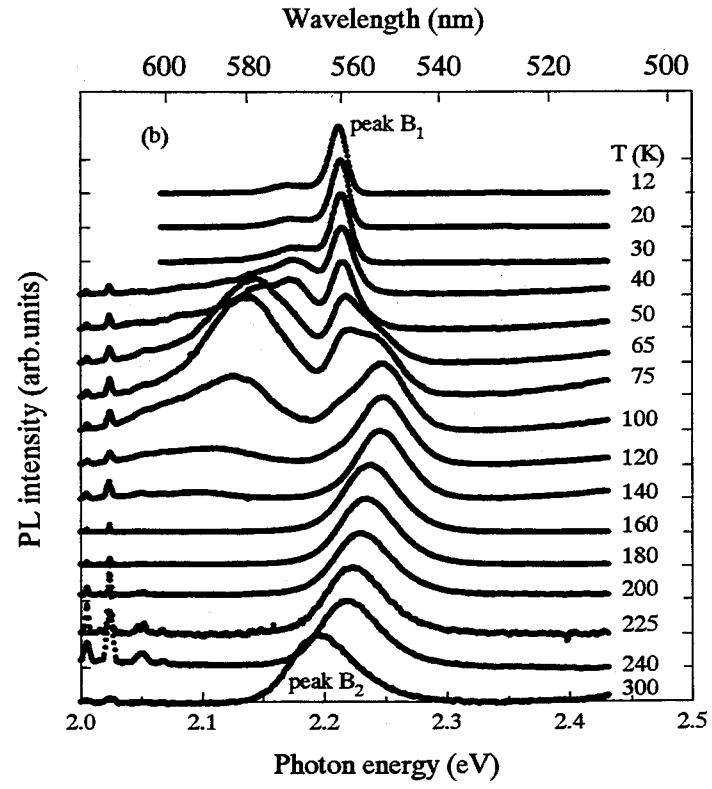
Wavelength (nm)
600
580
560
540
520
500
(b)
peak B1
T (K)
12
20
30
40
50
65
75
100
120
140
160
180
200
225
240
300
peak B2
PL intensity (arb.units)
2.0
2.1
2.2
2.3
2.4
2.5
Photon energy (eV)

Fig. 5.5

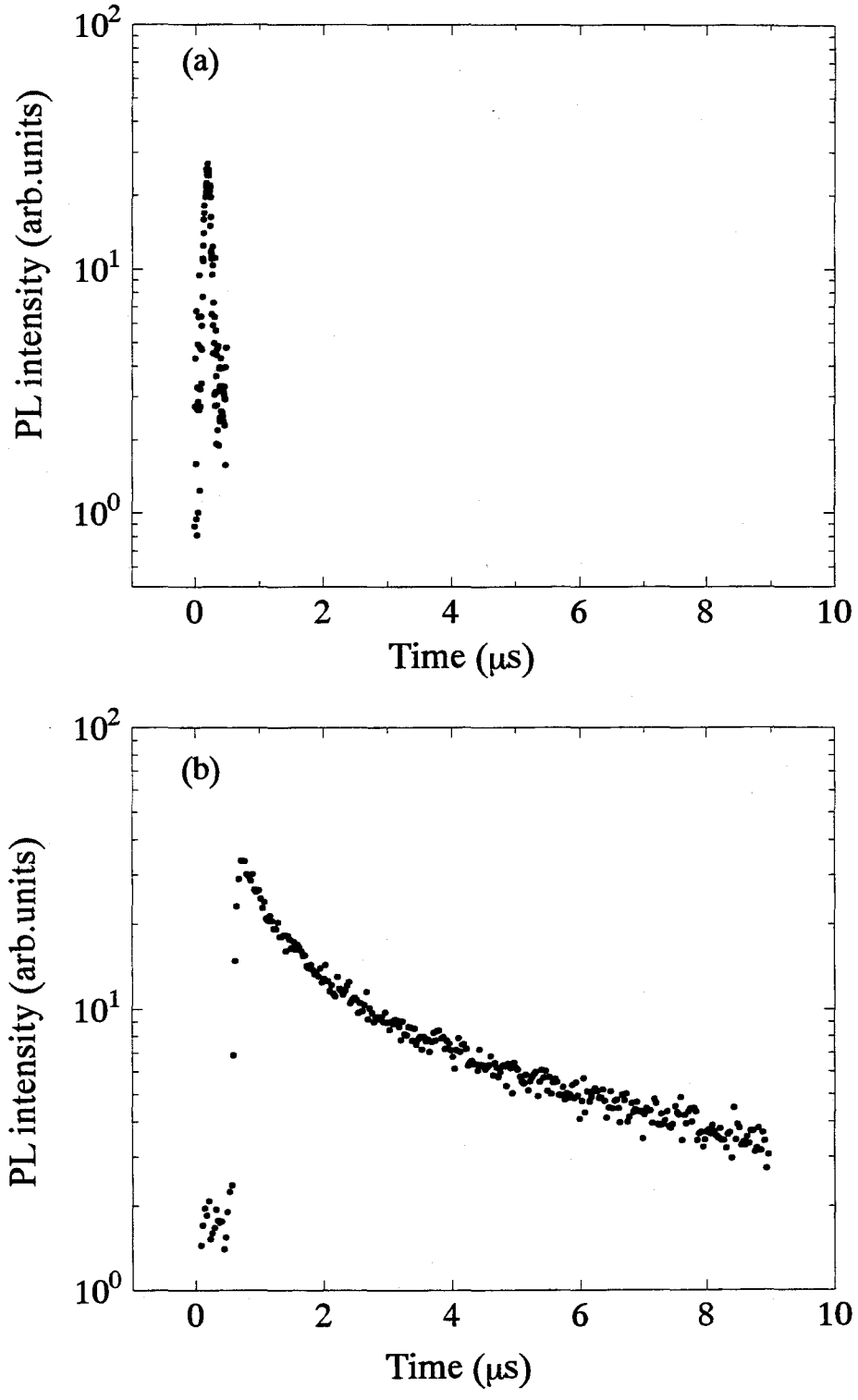
(a)
PL intensity (arb.units)
10^2
10^1
10^0
0
2
4
6
8
10
Time (μs)
(b)
PL intensity (arb.units)
10^2
10^1
10^0
0
2
4
6
8
10
Time (μs)

Fig. 5.6

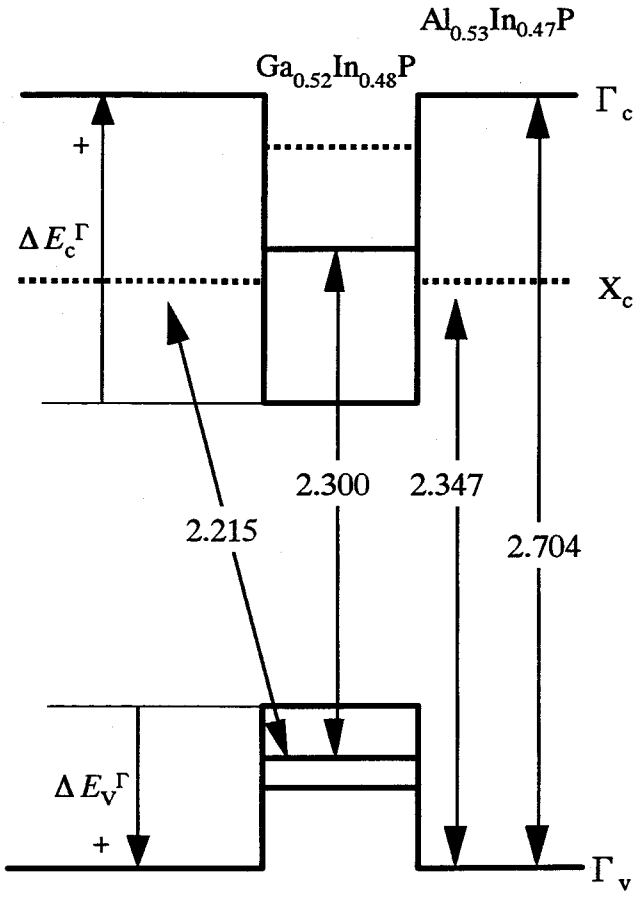
$Al_{0.53}In_{0.47}P$
$Ga_{0.52}In_{0.48}P$
Γ_c
+
ΔE_c^{Γ}
X_c
2.300
2.347
2.215
2.704
ΔE_V^{Γ}
+
Γ_v

Fig. 5.7

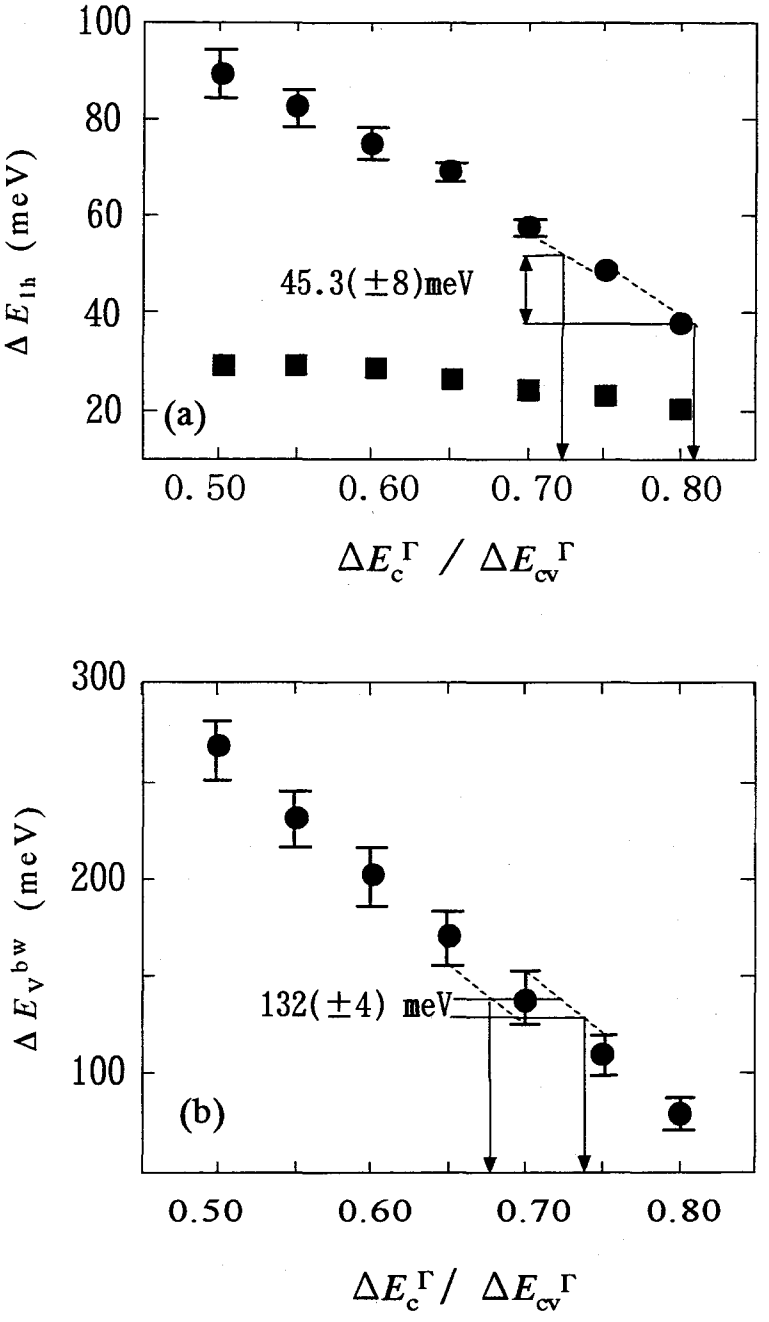
100
80
60
40
20
ΔE_{1h} (meV)
45.3(±8)meV
(a)
0.50
0.60
0.70
0.80
$\Delta E_c^{\Gamma} / \Delta E_{cv}^{\Gamma}$
300
200
100
ΔE_v^{bw} (meV)
132(±4) meV
(b)
0.50
0.60
0.70
0.80
$\Delta E_c^{\Gamma} / \Delta E_{cv}^{\Gamma}$

Fig. 5.8

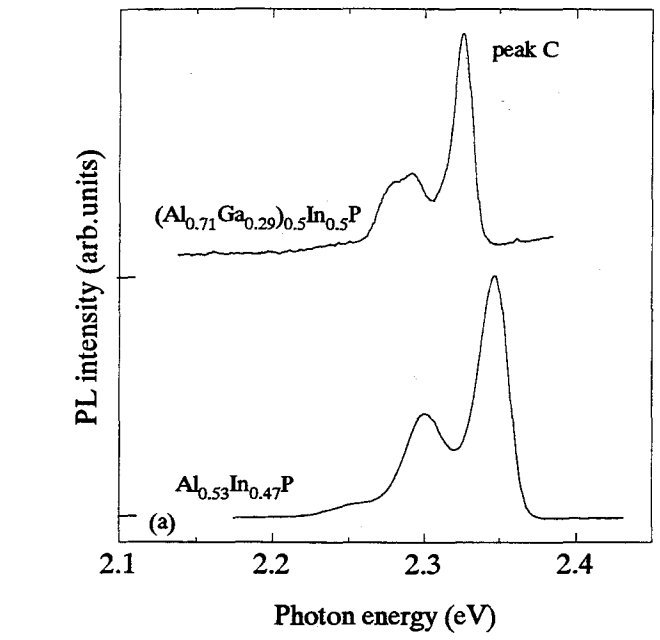
peak C
$(Al_{0.71}Ga_{0.29})_{0.5}In_{0.5}P$
$Al_{0.53}In_{0.47}P$
(a)
PL intensity (arb.units)
2.1
2.2
2.3
2.4
Photon energy (eV)

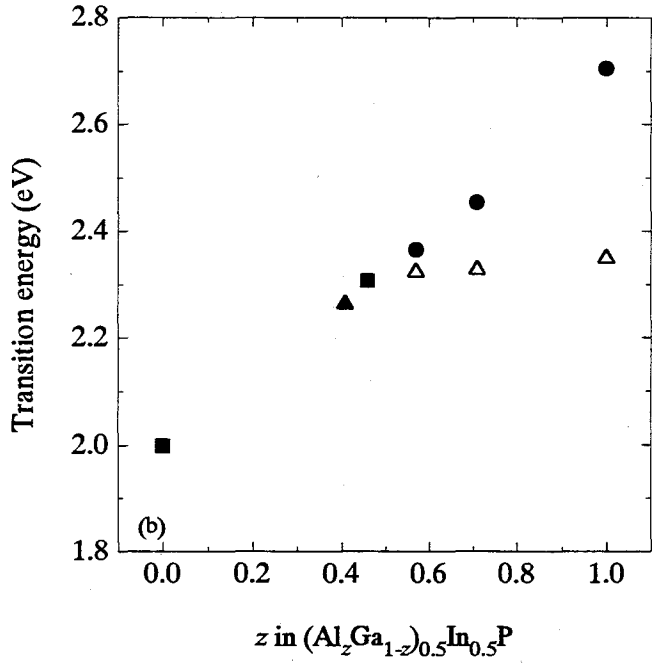
Transition energy (eV)
2.8
2.6
2.4
2.2
2.0
1.8
(b)
0.0
0.2
0.4
0.6
0.8
1.0
z in $(Al_zGa_{1-z})_{0.5}In_{0.5}P$

Fig. 5A.1

Chapter VI

Energy band alignment of the X_c , Γ_c and Γ_v points in the $(Al_{0.71}Ga_{0.29})_{0.5}In_{0.5}P/Al_yIn_{1-y}P$ heterostructures

Abstract

The transition energies at 20 K for Γ_{6c} - Γ_{7v} (electron - heavy hole) ($E_s^{hh}(y)$) and Γ_{6c} - $\Gamma_{6v(2)}$ (electron - light hole) ($E_s^{lh}(y)$) of strained and disordered $Al_yIn_{1-y}P$ ($0.43 \le y \le 0.62$) grown on GaAs substrates are obtained from photoreflectance spectra. I have conducted photoluminescence measurements to observe the X_c to Γ_v transitions in bulk $(Al_zGa_{1-z})_{0.5}In_{0.5}P$ alloys, the $Al_yIn_{1-y}P$ X_c to $(Al_{0.71}Ga_{0.29})_{0.5}In_{0.5}P$ Γ_v transition in $(Al_{0.71}Ga_{0.29})_{0.5}In_{0.5}P/Al_yIn_{1-y}P$ superlattices (y = 0.47 to 0.61), and the X_c to Γ_v or the Γ_c to Γ_v transitions in 20-nm-wide $Al_yIn_{1-y}P$ layers in $(Al_zGa_{1-z})_{0.5}In_{0.5}P$ / $Al_yIn_{1-y}P$ / $(Al_zGa_{1-z})_{0.5}In_{0.5}P$ double heterostructures (y = 0.33 to 0.39, z = 0.7 to 1.0). The relative energy levels of the Γ_c, Γ_v, and X_c points in the $Al_yIn_{1-y}P$ and the $(Al_{0.71}Ga_{0.29})_{0.5}In_{0.5}P$ alloys are obtained from these experimental results. The following are found: (1) for y = 0.47 - 0.61 the energy alignment of Γ points is type I, (2) in the Γ_c - Γ_v energy band alignment for y = 0.53, the share of the band offset at the Γ_c point is 75(±3) %, (3) for y = 0.47 - 0.61 X_c level of $Al_yIn_{1-y}P$ is lower than that of $(Al_{0.71}Ga_{0.29})_{0.5}In_{0.5}P$, and decreases by 0.09 eV as y increases, (4) X_c of $Al_yIn_{1-y}P$ crosses Γ_c at y = 0.340 (±0.008), (5) the Γ_v level of $Al_yIn_{1-y}P$ crosses the Γ_v level of the $(Al_{0.71}Ga_{0.29})_{0.5}In_{0.5}P$ at y = 0.47(±0.01).

6.1 Introduction

For the purpose of developing red-light emitting semiconductor laser diodes (LDs) with higher output power and higher operating temperature, structures for effective carrier confinement in the active region have been investigated. Iga *et al.* proposed a superlattice (SL) structure called multi-quantum barrier (MQB) in cladding layers. [1] MQB is expected to enhance the effective hetero-barrier heights as a result of the electron wave interference. The incorporation of an $Al_{0.5}In_{0.5}P/Ga_{0.5}In_{0.5}P$- MQB into cladding layers of the LD emitting 660 nm wavelength light reduced the threshold current, and increased the output power. [2] An example of the energy band diagram around the quantum well (QW) active region with and without the MQB is schematically drawn in Fig. 6.1(a). The band discontinuities at $Al_{0.53}In_{0.47}P/Ga_{0.52}In_{0.48}P$ heterojunction have been obtained in Chap. V. Another example is incorporating single $Al_yIn_{1-y}P$ barrier layers in the cladding layers. An example of the energy diagram with the barrier layers is drawn in Fig. 6.1(b). These examples utilize $Al_yIn_{1-y}P$ alloys, which has the largest energy gap among the III-V compound semiconductors that can be epitaxially grown on GaAs substrates. The $(Al_zGa_{1-z})_{0.5}In_{0.5}P$ cladding layers in the red-light-emitting laser devices are usually composed of the quaternary alloys with z around 0.7. [3] [4] However, the band alignment of the $(Al_{0.7}Ga_{0.3})_{0.5}In_{0.5}P/Al_yIn_{1-y}P$-hetrojunctiuon is not known yet. Although $(Al_{0.7}Ga_{0.3})_{0.5}In_{0.5}P$ and $Al_{0.5}In_{0.5}P$ have X_c points as the lowest energy levels in their conduction bands, [5] [6] the carrier leak via or to the X_c valley is not studied yet.

There are few studies on the transition energies of $Al_yIn_{1-y}P$ alloys. For unstrained samples grown by modified Bridgeman method Onton and Chicotka studied the dependence of the Γ_{6c} - Γ_{8v} and X_{6c} - Γ_{8v} transition energies of $Al_yIn_{1-y}P$ alloys on the AlP mole fraction y by cathode luminescence (CL) measurement. [7] They found that the transition energy increases linearly with y, and that the Γ_{6c} level crosses the X_{6c} level at y = 0.44 at around 300 K. The Γ_{6c}-Γ_{8v} transition energy (E_{cv}^{Γ}) at 300 K for y = 0.53 is 2.52 eV, which is smaller than the result shown in Chap. IV (2.59eV). Bour *et al.* grew samples by OMVPE at 675 °C in the indirect gap range of y ($0.4 \leq y \leq 0.6$), and studied E_{cv}^{Γ} by PR method. [8] They reported that the dependence of the transition energy on y is not linear. E_{cv}^{Γ} at y = 0.53 (2.43 eV at 300 K) is inconsistent both with 2.52 eV [7] and 2.593 eV obtained in Chap.IV. No report is present concerning the transition energies of strained and disordered $Al_yIn_{1-y}P$ alloys.

6.2 Experimental

The $Al_yIn_{1-y}P$ alloys were grown on the Si doped GaAs substrates. The LRO was prevented by the growth on the substrates with the surface orientation of (100) misoriented 7° toward [011] or (511)A at 710 - 730 °C. The AlP mole fraction in the $Al_yIn_{1-y}P$ layers were controlled by the method in Chap. III.

To obtain the Γ_c-Γ_v transition energies of strained $Al_yIn_{1-y}P$ layers, $(Al_{0.56}Ga_{0.44})_{0.5}In_{0.5}P$ (75nm)/$Al_yIn_{1-y}P$(20nm)/ $(Al_{0.56}Ga_{0.44})_{0.5}In_{0.5}P$(120nm) (y = 0.49, 0.57, 0.60, and 0.62) (type A) and $Al_{0.5}In_{0.5}P$ (75nm) /$Al_yIn_{1-y}P$(20nm)/$Ga_{0.52}In_{0.48}P$(20nm) /$Al_yIn_{1-y}P$ (20nm) /$Al_{0.5}In_{0.5}P$ (120nm) (y = 0.43, 0.45, and 0.47) (type B) structures were grown on 7 ° misoriented substrates and (511)A substrates, respectively. In these structures the strained layers were sandwiched by the unstrained layers so that the strain should not be relaxed. The surface region of samples with thickness of 25 nm was doped to p-type conductivity with Zn to enhance the PR signals. The other layers were undoped. The net carrier concentration of the doped layers was less than 1×10^{17} cm^{-3} as determined by the chemical C-V technique. The net carrier concentration of the undoped layers was found to be equal to or less than 3×10^{15} cm^{-3} of the n-type.

To obtain the X_c - Γ_v transition energies between the neighboring layers of heterostructures or within a strained $Al_yIn_{1-y}P$ layer, undoped $(Al_{0.71}Ga_{0.29})_{0.5}In_{0.5}P$ (23 or 8 nm) / $Al_yIn_{1-y}P$ (24 or 8 nm)-SLs with 20 periods on 7°-off substrates, and undoped $(Al_zGa_{1-z})_{0.5}In_{0.5}P$ (200 nm)/ $Al_yIn_{1-y}P$ (20 nm)/ $(Al_zGa_{1-z})_{0.5}In_{0.5}P$ (200 nm) (z = 0.7, 0.8, and 1.0, y = 0.33, 0.35, 0.36, 0.37, and 0.39) double heterostructures (DH structures) on (511)A substrates were grown.

PR measurements were carried out on type A and B samples to obtain the Γ_c-Γ_v transition energies at temperatures in the range of 20 - 100 K. The enhancement of the band bending due to the doping to the surface layer was not strong to induce the Franz-Kerdysh oscillation in the PR spectrum. PLE measurements were applied on the type B samples at 20 K. The intensity of PLE spectra was corrected for the dependence of the excitation power density on wavelength, which is shown in Fig. 2.8. The X_c to Γ_v transition energies were measured by the PL method at temperatures in the range of 12 K to 100 K. The samples were excited by the 476.5 nm line of the Ar+ laser. The excitation power density of the Ar+ laser was in the range of 0.02 to 6.4 W/cm^2.

6.3 Results and Discussion

6.3.1 Energy band alignment of the $(Al_{0.71}Ga_{0.29})_{0.5}In_{0.5}P/Al_{0.53}In_{0.47}P$ heterostructure

PL measurements were applied to two kinds of the $(Al_{0.71}Ga_{0.29})_{0.5}In_{0.5}P$/ $Al_{0.53}In_{0.47}P$ -SLs with different $(Al_{0.71}Ga_{0.29})_{0.5}In_{0.5}P$ and $Al_{0.53}In_{0.47}P$ thicknesses in one period (sample C: 23 nm and 8 nm and sample D: 8 nm and 24 nm). Figure 6.2 shows the excitation power density dependence of the PL spectra. There are two distinct peaks, and we denote the higher energy peak as peak A and the lower energy peak as peak B. A small broad peak lies on the lower energy side of these main peaks, and I ascribe this to a phonon-assisted transition similar to the small peaks in Fig. 5A.1(a). For both the samples, peak B has an energy of 2.287 eV regardless of the excitation power. However, peak A shifts to higher energies with increasing excitation power, and reaches 2.326 eV in both the samples, which agrees well with the X_c-Γ_v energy of the bulk single layer of the $(Al_{0.71}Ga_{0.29})_{0.5}In_{0.5}P$ alloy (Fig. 5A.1(a)). For sample C, peak A appears even at the lowest excitation power. On the other hand, the intensity of peak A for sample D is too low to be identified at the lowest excitation power. This indicates that carriers easily fill a band in the AlInP layers, and overflows from the band.

The differences in the energy levels of the Γ_c, X_c, and Γ_v points between the $(Al_{0.71}Ga_{0.29})_{0.5}In_{0.5}P$ and $Al_{0.53}In_{0.47}P$ are described as ΔE_c^{Γ}, ΔE_c^{X}, ΔE_v^{Γ}, respectively. When a level of $Al_{0.53}In_{0.47}P$ is higher than the corresponding level of $(Al_{0.71}Ga_{0.29})_{0.5}In_{0.5}P$ for instance, this is called positive for the conduction band and negative for the valence band. There are eight possible band energy alignment schemes from combinations of positive or negative signs at each band offset. These combinations are shown in Table 6-I. Since the energy gap at the Γ point (E_{cv}^{Γ}) of the $Al_{0.53}In_{0.47}P$ is larger than that of the $(Al_{0.71}Ga_{0.29})_{0.5}In_{0.5}P$, two of the candidates ([8] and [6]) are eliminated. Candidates [1], [5], and [4] are eliminated because the energies of the $(Al_{0.71}Ga_{0.29})_{0.5}In_{0.5}P$ X_c - Γ_v transition (peak A) and the $Al_{0.53}In_{0.47}P$ X_c - Γ_v transition are not the smallest ones. Since the Γ_c point energy level of $(Al_zGa_{1-z})_{0.5}In_{0.5}P$ decreases as z increases in the $(Al_zGa_{1-z})_{0.5}In_{0.5}P$ /$Ga_{0.52}In_{0.48}P$ heterostructure (ref.9 and Chap.V), the positive ΔE_v^{Γ} in $(Al_{0.71}Ga_{0.29})_{0.5}In_{0.5}P$ /$Al_{0.53}In_{0.47}P$ is concluded to leave candidates of [3] and [7]. Peak B is identified as the $Al_{0.53}In_{0.47}P$ X_c - $(Al_{0.71}Ga_{0.29})_{0.5}In_{0.5}P$ Γ_v transition. The difference between the energy level of the $(Al_{0.71}Ga_{0.29})_{0.5}In_{0.5}P$ Γ_c and that of the $Al_{0.53}In_{0.47}P$ Γ_v is 2.51 eV from the sum of ΔE_v^{Γ} (60 ±3 meV) and E_{cv}^{Γ} of the AlGaInP (2.454 eV), and is smaller than E_{cv}^{Γ} of $Al_{0.53}In_{0.47}P$ (2.704 eV). Thus, ΔE_c^{Γ} should be positive. Hence, the band alignment of [3] is concluded: type I band energy alignment. This is schematically depicted in Fig. 6.3. ΔE_c^{Γ}, ΔE_c^{X}, and ΔE_v^{Γ} are calculated to be 190 (±6) meV, -39 (±3)

meV, and 60 (±3) meV, respectively, and thus $\Delta E_c^{\Gamma}/\Delta E_{cv}^{\Gamma}$ ($\Delta E_{cv}^{\Gamma} = \Delta E_c^{\Gamma} + \Delta E_v^{\Gamma}$) is 0.75 (±0.03).

The excitation power dependence of the relative PL peak intensities is interpreted as follows. As the excitation power increases, the X_c band of AlInP is filled owing to the small rate of the $Al_{0.53}In_{0.47}P$ X_c - $(Al_{0.71}Ga_{0.29})_{0.5}In_{0.5}P$ Γ_v transition (analogous to the AlInP X_c - GaInP Γ_v transition in Chap. V). The energy of allowed transition increases as the band is filled (analogous to the Burstein-Moss shift). [10] The energy of peak A increases until the AlInP X_c is completely filled and the transition from the AlGaInP X_c eventually becomes dominant. For the sample with thin AlInP layers (sample C), the X_c valley of AlInP is easily filled with electrons, so peak A as well as peak B is produced even at a low excitation power. The sharp peak at 2.29 eV is observed at the highest excitation power because it is probably excitonic in nature.

With the knowledge of the band offsets of the $Ga_{0.52}In_{0.48}P$ / $Al_{0.53}In_{0.47}P$ heterostructure (Chap. V) the present result leads us to a band offset ΔE_c^{Γ} for the $Ga_{0.52}In_{0.48}P/(Al_{0.71}Ga_{0.29})_{0.5}In_{0.5}P$ of 325 (±35) meV. The ΔE_c^{Γ} and $\Delta E_c^{\Gamma}/\Delta E_{cv}^{\Gamma}$ are shown in Fig. 6.4. The value for the $Ga_{0.52}In_{0.48}P/(Al_{0.71}Ga_{0.29})_{0.5}In_{0.5}P$ is consistent with those of $Ga_{0.52}In_{0.48}P/Al_{0.53}In_{0.47}P$ and the result by Liedenbaum *et al.* for the $Ga_{0.5}In_{0.5}P$ $/(Al_{0.6}Ga_{0.4})_{0.5}In_{0.5}P$. [11]

6.3.2 Optical transition energies of the strained $Al_yIn_{1-y}P$ alloys

Figure 6.5(a) is an example of the PR spectra of type B samples with y = 0.43 at 20 K. The PR spectra were fitted to the superposition of several functions of eq.(4-5). The transitions are assumed to be the Γ_{6c} - Γ_{7v} (electron-heavy hole), the Γ_{6c} - $\Gamma_{6v(2)}$ (electron-light hole), and the Γ_{6c} - $\Gamma_{6v(1)}$ (electron-spin-orbit-split hole) transitions in the $Al_{0.43}In_{0.57}P$ layer, and the Γ_{6c} - Γ_{8v} and the Γ_{6c} - Γ_{7v} (electron-spin-orbit-split hole) transitions in the $Al_{0.5}In_{0.5}P$ layer. The obtained transition energies are 2.486 eV (Γ_{6c} - Γ_{7v}), 2.506 eV (Γ_{6c} - $\Gamma_{6v(2)}$), and 2.57 eV (Γ_{6c} - $\Gamma_{6v(1)}$) for $Al_{0.43}In_{0.57}P$ and 2.686 eV (Γ_{6c} - Γ_{8v}) and 2.75 eV (Γ_{6c} - Γ_{7v}) for $Al_{0.5}In_{0.5}P$ as indicated by the arrows in Fig. 6.5(a). The structures shown in the energy range smaller than 2.4 eV is attributed to the energy levels in the QW. The layers of $Al_{0.5}In_{0.5}P$ are slightly lattice mismatched to the substrate ($\Delta a_{\perp}/a_0$ = +0.15 %). This leads to the discrepancy of the Γ_{6c} - Γ_{8v} transition energy from the value for completely lattice matched alloys ($\Delta a^{\perp}/a_0 \leq \pm$ 0.02%) of 2.704 eV. The PLE spectrum is shown for reference in Fig. 6.5(b). The PL intensity was monitored at 620 nm (2.000 eV), where the luminescence from the $Ga_{0.52}In_{0.48}P$ quantum well had the peak intensity. The band edge positions are in good agreement with the transition energies obtained by PR. The Γ_c - Γ_v transition energies of the samples with y = 0.57,

0.60, and 0.62 at 20 K are estimated from the energies measured at 100 K, because the signal to noise ratio was too low at the lower temperature (20 K). The difference between the energy at 20 K and that at 100 K for bulk $Al_{0.53}In_{0.47}P$ (17 meV, see Chap.V) is added to the energies measured at 100 K on the assumption of the parallelism between the temperature dependence of E_{cv}^{Γ} of $Al_{0.53}In_{0.47}P$ and that of $Al_yIn_{1-y}P$. Figure 6.6 shows the dependence of the transition energies on AlP mole fraction y at 20 K. The transition energy varies linearly as y increases. This is in consistent with Onton and Chicotka for unstrained alloys. [7] The dependence of the transition energies at 20 K are expressed by the following functions.

$$E_s^{hh}(y) = 1.488\ (\pm 0.020) + 2.302\ (\pm 0.041) \cdot y \qquad (6\text{-}1)$$

$$E_s^{lh}(y) = 1.738\ (\pm 0.030) + 1.812\ (\pm 0.061) \cdot y \qquad (6\text{-}2)$$

6.3.3 X_c-Γ_v transition energies of the strained $Al_yIn_{1-y}P$ alloys

Figure 6.7(a) shows examples of the PL spectra of $(Al_zGa_{1-z})_{0.5}In_{0.5}P$ (200 nm)/$Al_yIn_{1-y}P$ (20 nm)/ $(Al_zGa_{1-z})_{0.5}In_{0.5}P$ (200 nm) - DH structures; the spectra are for z = 0.7, y = 0.33 (sample E) and z = 0.7, y = 0.35 (sample F) at 12 K. The shape of the spectra for the other samples with y = 0.36, 0.37, and 0.39 and z = 0.7, 0.8, and 1.0 are similar to that of sample F. The spectrum of sample F has two distinct peaks (F_a and F_b). Both of them are accompanied by phonon-assisted transition peaks. The highest energy peak (F_a: 2.326 eV) is assigned to the X_c - Γ_v transition in the $(Al_{0.71}Ga_{0.29})_{0.5}In_{0.5}P$ layer because it has the same energy as the peak for the bulk $(Al_{0.71}Ga_{0.29})_{0.5}In_{0.5}P$ single layer (Fig. 5A.1(a)). There are two candidates for the origin of the lower energy peak (F_b): the X_c - Γ_v transition in $Al_{0.35}In_{0.65}P$ and the $(Al_{0.71}Ga_{0.29})_{0.5}In_{0.5}P$ X_c - $Al_{0.35}In_{0.65}P$ Γ_v transition. In the PL spectra of a series of samples with z of 0.7, 0.8, and 1.0 for the same y of 0.36, it is found that the lower PL peak energies were 2.272 (±0.002) eV for all three samples. The calculation of energy levels in the $Al_yIn_{1-y}P$ well using the square potential well model (Chap.V) showed that the variation in the z value of the neighboring $(Al_zGa_{1-z})_{0.5}In_{0.5}P$ causes the variation of the X_c or the Γ_v level within a few meV. Thus, the constant peak energy for all values of y is consistent with the model of the X_c - Γ_v transition in the $Al_{0.36}In_{0.64}P$ well. With the model of the $(Al_zGa_{1-z})_{0.5}In_{0.5}P$ X_c - $Al_{0.36}In_{0.64}P$ Γ_v transition, the energy level alignment of the $(Al_zGa_{1-z})_{0.5}In_{0.5}P/Al_{0.36}In_{0.64}P$ heterostructures for z = 0.7 and 1.0 is shown in Fig. 6.8. The transition energies of the $(Al_zGa_{1-z})_{0.5}In_{0.5}P$ X_c - $Al_{0.36}In_{0.64}P$ Γ_v for z = 0.7 and 1.0 are shown as E_1 and E_2, respectively. ΔE_v^{Γ} is the band offset between the alloy with z = 0.7 and that with z = 1.0

at the Γ_v point. In this scheme, E_2 is equal to E_1- ΔE_v^{Γ} + (2.347 - 2.326) eV. Since ΔE_v^{Γ} is 60 (±3) meV as calculated before, the PL peak energy should shift by 39 (±5) meV in this model, which was not observed in the experimental result. It is concluded that the observed peak F_b is for the X_c - Γ_v transition in the AlInP well. The energies of the F_b peaks at 12 K for the samples with various y and $z = 0.7$ are plotted with the open circles in Fig. 6.7(b). They are consistent with the X_c-Γ_v transition energy of the bulk $Al_{0.53}In_{0.47}P$.

The temperature dependence of the PL spectrum of sample F is shown in Fig. 6.7(c). As the temperature increases, a new peak appears at 50 K as a shoulder, and it becomes dominant at 100 K. This must be of Γ_c-Γ_v transition nature because phonon-assisted transition peaks are not seen. E_{cv}^{Γ} at 12 K is obtained to be 2.300 eV by the subtraction of the calculated quantization energy of 7 meV and the addition of 17 meV to E_{cv}^{Γ} at 100 K on the assumption of the parallelism between the temperature dependence of E_{cv}^{Γ} of $Al_{0.35}In_{0.65}P$ and that of $Al_{0.53}In_{0.47}P$. This result is plotted with a closed circle in Fig. 6.7(b). Note that peak E_a of sample E in Fig. 6.7(a) is not accompanied by a phonon-assisted transition peak and is about 20 times stronger than the PL peaks of sample F. Therefore, the peak should be of the Γ_c-Γ_v transition nature. The peak energy is plotted with a closed circle in Fig. 6.7(b). The closed circles in the figure agree well with eq.(6-1) shown as the dashed line ($E_{h.h.}^{\Gamma}(y)$). The Γ_c-X_c crossing point is estimated to be 0.340 (± 0.008).

6.3.4 Energy band alignment scheme of the $(Al_{0.71}Ga_{0.29})_{0.5}In_{0.5}P/Al_yIn_{1-y}P$ heterostructures

The PL spectra of $(Al_{0.71}Ga_{0.29})_{0.5}In_{0.5}P$ (23 nm) / $Al_yIn_{1-y}P$ (8 nm) -SLs ($0.47 \leq y \leq 0.61$) are shown in Fig. 6.9(a). As the AlP mole fraction y increases, peak A shifts to lower energy and becomes broader. ΔE_c^X, which is obtained as the difference between 2.326 eV and the energy of peak B, is plotted in Fig. 6.9(b). ΔE_c^X decreases by 0.09 eV as y increases from 0.47 to 0.61, and the X_c level of the $Al_yIn_{1-y}P$ never exceed that of the $(Al_{0.71}Ga_{0.29})_{0.5}In_{0.5}P$ in this range.

Using these results, we can draw the energy level diagram of the $(Al_{0.71}Ga_{0.29})_{0.5}In_{0.5}P$ / $Al_yIn_{1-y}P$ heterostructure as shown in Fig. 6.10 by the following process. The Γ_c level of $Al_yIn_{1-y}P$ alloy is set as the base line, and the relative position of each band is plotted. First, we draw the line for the X_c level of the $Al_yIn_{1-y}P$ alloy using the X_c - Γ_c crossing point in the $Al_yIn_{1-y}P$ and the X_c levels at $y = 0.35$, 0.36, 0.37, 0.39, and 0.53 (▲). Next, the X_c level of the $(Al_{0.71}Ga_{0.29})_{0.5}In_{0.5}P$ layer (□) is plotted using Fig. 6.9(b). Finally, the levels of Γ_c (■) and Γ_v (Δ) of $(Al_{0.71}Ga_{0.29})_{0.5}In_{0.5}P$ are plotted. In this schematic

representation of the relative energy levels, the Γ_v level of the $Al_yIn_{1-y}P$ crosses that of the $(Al_{0.71}Ga_{0.29})_{0.5}In_{0.5}P$ at $y = 0.47$ (± 0.01). Hence, the peak B in the spectrum for $y = 0.47$ in Fig. 6.9(a) is concluded to be the superposition of the spectra of the AlInP X_c - AlGaInP Γ_v and AlInP X_c - AlInP Γ_v transitions. The broad and relatively large intensity peak located at the low energy side of peak B is concluded to be caused by the superposition of phonon-assisted transitions that originate from the AlInP X_c - AlGaInP Γ_v and AlInP X_c - AlInP Γ_v transitions.

When a layer of $Al_yIn_{1-y}P$ ($0.47 \leq y \leq 0.61$) is incorporated into the $(Al_{0.71}Ga_{0.29})_{0.5}In_{0.5}P$ cladding, it serves as a barrier at the Γ point, but not at the X_c point. It is concluded that the Γ_v energy level of $Al_yIn_{1-y}P$ ($y < 0.47$) is lower than that of the $(Al_{0.71}Ga_{0.29})_{0.5}In_{0.5}P$; this layer does not act as a barrier to holes.

Appendix 6 Deformation potentials of the $Al_yIn_{1-y}P$ crystals

The vertex of the valence band at Γ_{8v} of an unstrained zinc blende type crystal consists of a four folded $P_{3/2}$ (J = 3/2, m_J = ±3/2, ±1/2) state. Here J is the total angular momentum quantum number and m_J is the magnetic sub-quantum number. With the biaxial strain in (100) the crystal has the double space group of D_{2d}^*; the Γ_{8v} energy level splits to the heavy hole state (Γ_{7v}) and the light hole state ($\Gamma_{6v(2)}$). These energy states correspond to (J,m_J) = (3/2, ±3/2) and (3/2, ±1/2), respectively. The theoretical formula was studied by Pikus and Bir,[12] where the potential deformation was assumed small enough to be taken as a perturbation, and the invariance of the period of the crystal was also assumed. Since $\Delta a/a$ in my experiment was less than 1.2 %, the perturbation theory is applied. The present strained epitaxial layers have biaxial strain. The shifts due to the strain for Γ_{6c} - Γ_{7v} and Γ_{6c} - $\Gamma_{6v(2)}$ transition energies are described in the following formulae,[13]

$$\Delta E^h(\varepsilon) = \{ - 2V_a (C_{11} - C_{12}) / C_{11} + V_b (C_{11}+2C_{12}) / C_{11} \} \varepsilon, \qquad (6A\text{–}1)$$

$$\Delta E^l(\varepsilon) = \{ - 2 V_a (C_{11} - C_{12}) / C_{11} - V_b (C_{11}+2C_{12}) / C_{11} \} \varepsilon, \qquad (6A\text{–}2)$$

where V_a is the hydrostatic deformation potential which is the sum of the potentials for the valence band and that for the conduction band. V_b is the shear deformation potential for the valence band. The ratio of the elastic stiffnesses C_{12}/C_{11} is obtained from the interpolation between the value of InP and that of AlP(see Table 3-III).

Equations (6-1) and (6-2) are approximated by the sum of the Γ_{6c} - Γ_{8v} transition energy of the unstrained $Al_yIn_{1-y}P$ alloy and the respective energy shift expressed by eqs. (6A-1) and (6A-2). E_{cv}^{Γ}s of unstrained alloys (E_u) are measured at 20 K by PR method on an undoped InP on an n-InP substrate, an undoped disordered $Al_{0.53}In_{0.47}P$ on a GaAs substrate, and an undoped disordered $Al_{0.73}In_{0.27}P$ on an (100) n-$GaAs_{0.61}P_{0.39}$ substrate with the misorientation angle of 2° toward [$0\bar{1}1$]. The result is shown in Fig. 6A.1. E_u at 20 K is expressed as a linear function of y:

$$E_u(y) = 1.418\ (\pm 0.007) + 2.416\ (\pm 0.013) \cdot y \quad \text{(eV)}. \qquad (6A\text{-}3)$$

The slope of the function is larger than that of Onton and Chicotka by 0.19 eV. The experimental formulae of $\Delta E^h(\varepsilon)$ and $\Delta E^l(\varepsilon)$ corresponding to eqs. (6A-1) and (6A-2) were obtained by subtraction of eq.(6A-3) from eqs.(6-1) and (6-2). Here, eqs. (6-1),

(6-2), and (6A-3) were transformed to the function of ε. These two functions were substituted to the next expression of V_a and V_b which are obtained from eqs. (6A-1) and (6A-2)

$$V_a = - C_{11} / 4 (C_{11} - C_{12}) (\Delta E^h (\varepsilon) + \Delta E^l (\varepsilon)) / \varepsilon, \qquad (6A.4)$$

$$V_b = \quad C_{11} / 2 (C_{11} + 2C_{12}) (\Delta E^h (\varepsilon) - \Delta E^l (\varepsilon)) / \varepsilon. \qquad (6A.5)$$

V_a and V_b are found to be -5.23 (±0.55) eV and -1.67 (±0.26) eV, respectively. Since $\Delta E^h(\varepsilon)$ and $\Delta E^l(\varepsilon)$ of $Al_yIn_{1-y}P$ are expressed by linear functions of ε, the deformation potentials of InP is estimated using the values of elastic stiffness of InP (see Table 3-III). The respective values of V_a and V_b at 20 K are found to be 5.88 (±0.59) eV and 1.54 (±0.24) eV. The decreases of $\frac{\partial E_u}{\partial y}, \frac{\partial E_s^{hh}}{\partial y}$, and $\frac{\partial E_s^{lh}}{\partial y}$ as the increase of crystal temperature from 20 to 300 K are estimated from the E_{cv}^{Γ} dependence of ΔE_{lr} shown in Fig. 4A-1. The values of V_a and V_b at 300 K are found to be -5.21 (±0.35) eV and -1.64 (±0.16) eV for $Al_{0.53}In_{0.47}P$, and -5.70 (±0.60) eV and -1.50 (±0.24) eV for InP.

To date, there are several reports on the values of V_a and V_b for GaP and InP around 300 K. These values are listed in Table 6A-I. For V_b the value for InP obtained in this present report agrees with the result of Gavini and Cardona. [14] GaP is found to have almost the same value as InP by Zallen and Paul. [15] For V_a the present value agrees with Zallen and Paul, [16] but differs from the other results. [17] [18] The value of GaP is larger than the values for InP.

References

1) K.Iga, H.Uenohara, and F.Koyama, Electronic Lett. 22 1008 (1986)
2) K.Kishino, A.Kikuchi, Y.Kaneko, and I.Nomura, Appl.Phys.Lett., 58, 1822 (1991)
3) A.Valster, C.J.Van der Poel, M.N.Finke, and M.J.B.Boermans, Electron.Lett., 28, 144 (1992)
4) T.Tanaka, H.Yanagisawa, M.Takimoto, and S.Minagawa, Electron.Lett., 29, 1864 (1993)
5) H.Asahi, Y.Kawamura, and H.Nagai, J.Appl.Phys. 53, 4928 (1982)
6) K.Yamashita, T.Kita, H.Nakayama, and T.Nishino, Phys.Rev.B 23, 15713 (1996)
7) A.Onton and R.J.Chicotka, J.Appl.Phys.41 4205 (1970)
8) D.P.Bour, J.R.Shealy,G.W.Wicks, and W.J.Schaff, Appl.Phys.Lett. 50 615 (1987)
9) M.O.Watanabe and Y.Ohba, Appl.Phys.Lett., 50, 906 (1987)
10) J.I.Pankove, Optical processes in semiconductors, Prentice-Hall Inc., London, 1971
11) C.T.H.F.Liedenbaum, A.Valster, A.L.J.Severens, and G.W.`tHooft, Appl. Phys.Lett. 57, 2698 (1990)
12) G.E.Pikus and G.L.Bir, Sov.Phys.Solid State 1 1502 (1960)
13) H.Asai and K.Oe, J.Appl.Phys. 54 2052 (1983)
14) A.Gavini and M.Cardona, Phys.Rev.B 1 672 (1970)
15) R.Zallen and W. Paul, Phys.Rev. 134 A1628 (1964)
16) R.Zallen and W.Paul, Phys.Rev. 155 703 (1967)
17) A.L.Edwards, H.G.Drickamer, Phys.Rev. 122 1149 (1961)
18) G.D.Pitt, Solid State Commun. 8 1119 (1970)

Table 6-I Signs of band offsets for candidates of band discontinuities.

candidate number	[1]	[2]	[3]	[4]	[5]	[6]	[7]	[8]
ΔE_c^{Γ}	+	+	+	+	−	−	−	−
ΔE_c^{X}	+	+	−	−	+	+	−	−
ΔE_v^{Γ}	+	−	+	−	+	−	+	−

Table A6-I List of the deformation potentials V_a and V_b for InP and GaP.

	$(C_{11}+2C_{12})/3$	$\partial E_{cv}^{\Gamma} / \partial P$ (10^{-12} eV/dyn cm^{-2})	V_a (eV)	V_b (eV)
GaP	0.888 [a]	10.7 [b]	-9.5 [f]	-1.3 [a]
InP	0.725 [a]	4.7 [c]	-3.4 [f]	-1.55 [g]
		8.4 [d]	-6.1 [f]	
		11.0 [e]	-7.9 [f]	

[a] ref.13, [b] ref.15 [c] ref.17 [d] ref.16, [e] ref.18

[f] This value was derived from the relationship of $V_a = -\frac{C_{11}+2C_{12}}{3}\frac{\partial E_{cv}^{\Gamma}}{\partial P}$.

[g] ref.13

Figure captions

Fig. 6.1 Schematic illustration of the band energy diagram around the quantum well active region of a laser device. The carrier leak processes are shown by arrows.
(a) For the structure with and without MQB.
(b) For the structure with AlInP single barrier layers.

Fig. 6.2 Excitation power dependence of PL spectra for $(Al_{0.71}Ga_{0.29})_{0.5}In_{0.5}P$ / $Al_{0.53}In_{0.47}P$ superlattices at 12 K.
(a) Sample C (23 nm/8 nm); the excitation power is 0.07, 0.39, 1.6, 3.5, and 6.4 W/cm^2.
(b) Sample D (8 nm/24 nm); the excitation power is 0.07, 0.39, 1.6, 3.5, and 6.4 W/cm^2.

Fig. 6.3 Band energy alignment of X_c and Γ points for the $(Al_{0.71}Ga_{0.29})_{0.5}In_{0.5}P$ /$Al_{0.53}In_{0.47}P$ heterostructure at 12 - 20 K.

Fig. 6.4 Alloy composition z dependence of the band offset at the Γ_c point for $(Al_zGa_{1-z})_{0.5}In_{0.5}P/Ga_{0.52}In_{0.48}P$.
O: ΔE_c^{Γ}, ●: $\Delta E_c^{\Gamma}/\Delta E_{cv}^{\Gamma}$. The values for $Al_{0.53}In_{0.47}P/Ga_{0.52}In_{0.48}P$ and $(Al_{0.6}Ga_{0.4})_{0.5}In_{0.5}P$ / $Ga_{0.5}In_{0.5}P$ are from Chap. V and Liedenbaum *et al.* (5 K) [10], respectively.

Fig. 6.5 Examples of measurements for Γ_c - Γ_v transition energies.
(a) PR spectrum of $Al_{0.5}In_{0.5}P/Al_{0.43}In_{0.57}P/Ga_{0.52}In_{0.48}P/Al_{0.43}In_{0.57}P/Al_{0.5}In_{0.5}P$ layers on a (511)A GaAs substrate at 20K. The two arrows at higher transition energy are for $Al_{0.5}In_{0.5}P$. The three arrows at the lower energy side are for $Al_{0.43}In_{0.57}P$.
(b) PLE spectrum for the same sample at 20K.

Fig. 6.6 Alloy composition dependence of Γ_c - Γ_v transition energies of $Al_yIn_{1-y}P$ alloys on GaAs substrates at 20 K.
O: the Γ_{6c} - Γ_{7v} (electron-heavy hole) transition, ●: the Γ_{6c} - $\Gamma_{6v(2)}$ (electron-light hole) transition. The samples for y = 0.49, 0.57, 0.60, and 0.62 are on the substrates with the misorientation angle of 7°. The other samples are on

(511)A substrates. The plots for y = 0.57, 0.60, and 0.62 are obtained by adding 17 meV to the data at 100 K. The other plots are the results at 20 K.

Fig. 6.7 PL spectra of $(Al_{0.71}Ga_{0.29})_{0.5}In_{0.5}P$ / $Al_yIn_{1-y}P$ /$(Al_{0.71}Ga_{0.29})_{0.5}In_{0.5}P$-DH structures.
(a) Samples E (y = 0.33) and F (y = 0.35). The measurement temperature is 12 K, and the excitation power is 70 mW/cm^2.
(b) Dependence of the transition energies on the value of y in $Al_yIn_{1-y}P$ alloys.
●: Γ_c-Γ_v transition. ○: X_c- Γ_v transition.
(c) Temperature dependence of PL spectra of sample F.
The excitation power is 150 mW/cm^2.

Fig. 6.8 Example of the band energy alignment of $(Al_zGa_{1-z})_{0.5}In_{0.5}P$ /$Al_{0.36}In_{0.64}P$-DH structures at 12 K (z = 0.7 and 1.0).

Fig. 6.9 (a) PL spectra of $(Al_{0.71}Ga_{0.29})_{0.5}In_{0.5}P/Al_yIn_{1-y}P$ superlattices.
The excitation power is 3.5W/cm^2, and the temperature is 12 K.
(b) ΔE_c^X of $(Al_{0.71}Ga_{0.29})_{0.5}In_{0.5}P/Al_yIn_{1-y}P$ heterostructures at 12 K.

Fig. 6.10 Energy band alignment scheme of the X_c and Γ points for $(Al_{0.71}Ga_{0.29})_{0.5}In_{0.5}P/Al_yIn_{1-y}P$ heterostructures at 12 - 20 K.
●: the heavy hole state of $Al_yIn_{1-y}P$, ○: the light hole state of $Al_yIn_{1-y}P$, △: the Γ_v point of $(Al_{0.71}Ga_{0.29})_{0.5}In_{0.5}P$, □: the X_c point of $(Al_{0.71}Ga_{0.29})_{0.5}In_{0.5}P$, ■: the Γ_c point of $(Al_{0.71}Ga_{0.29})_{0.5}In_{0.5}P$, and ▲: the X_c point of $Al_yIn_{1-y}P$. The lines for E_{cv}^{Γ}s for $Al_yIn_{1-y}P$ are described in eqs.(6-1) and (6-2). The other lines and curves are to guide the reader's eyes.

Fig. 6A.1 AlP mole fraction dependence of the Γ_{6c} - Γ_{8v} transition energy for unstained $Al_yIn_{1-y}P$.
●: present experiment at 20 K, ○: present experiment at 300 K, ■:Onton and Chicotka at 300 K, □: Bour *et al.* at 300 K. The line is the fitted function to the data at 20 K shown in eq.(6A-3).

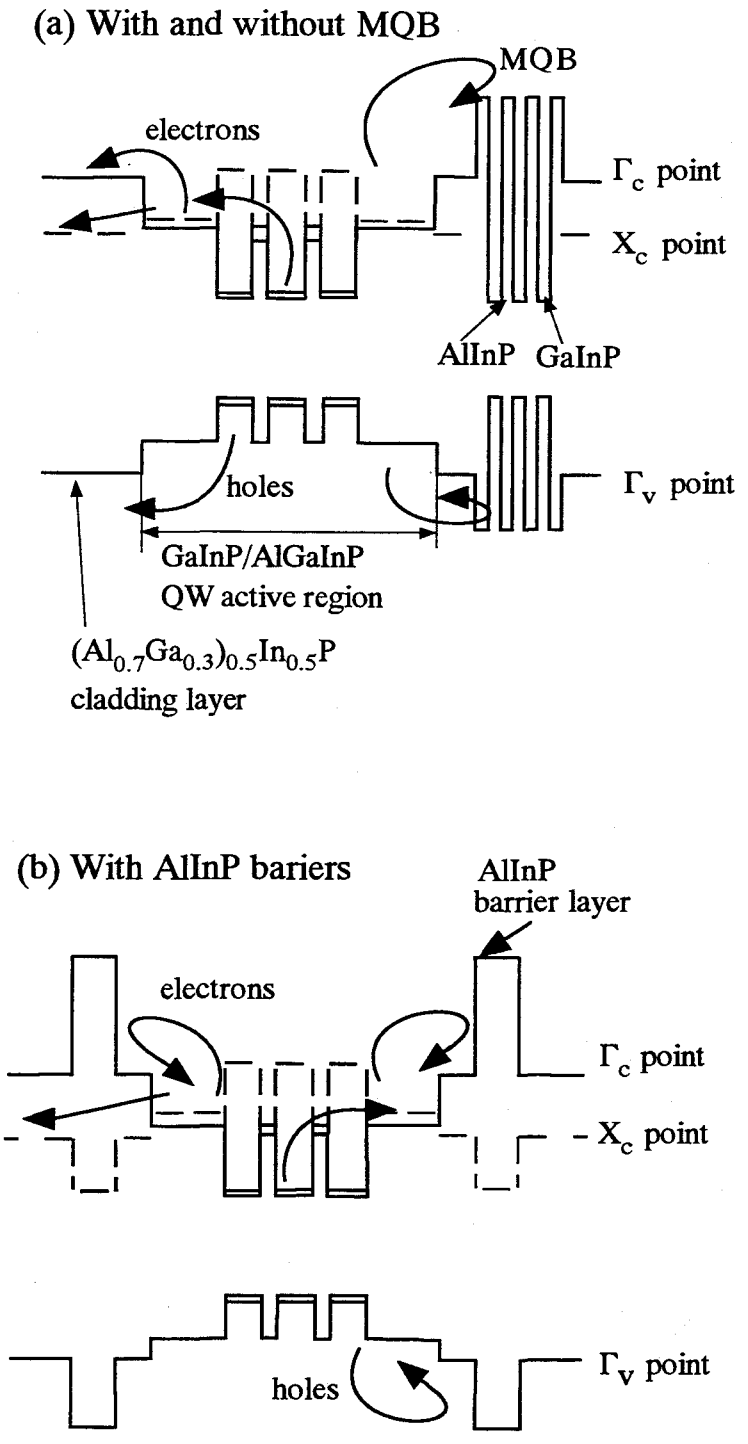
(a) With and without MQB
MQB
electrons
Γ_c point
X_c point
AlInP
GaInP
holes
Γ_v point
GaInP/AlGaInP
QW active region
$(Al_{0.7}Ga_{0.3})_{0.5}In_{0.5}P$
cladding layer
(b) With AlInP bariers
AlInP
barrier layer
electrons
Γ_c point
X_c point
holes
Γ_v point

Fig. 6.1

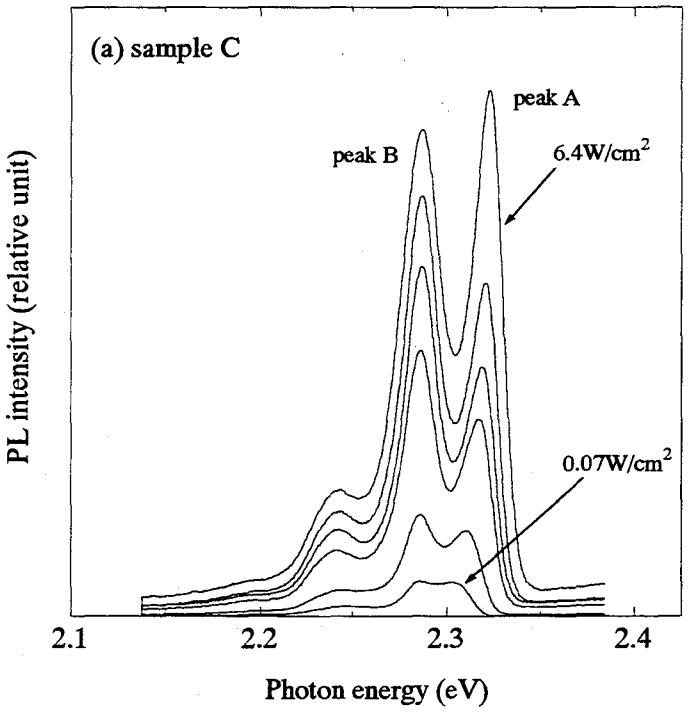
(a) sample C
peak A
peak B
6.4W/cm2
0.07W/cm2
PL intensity (relative unit)
2.1
2.2
2.3
2.4
Photon energy (eV)

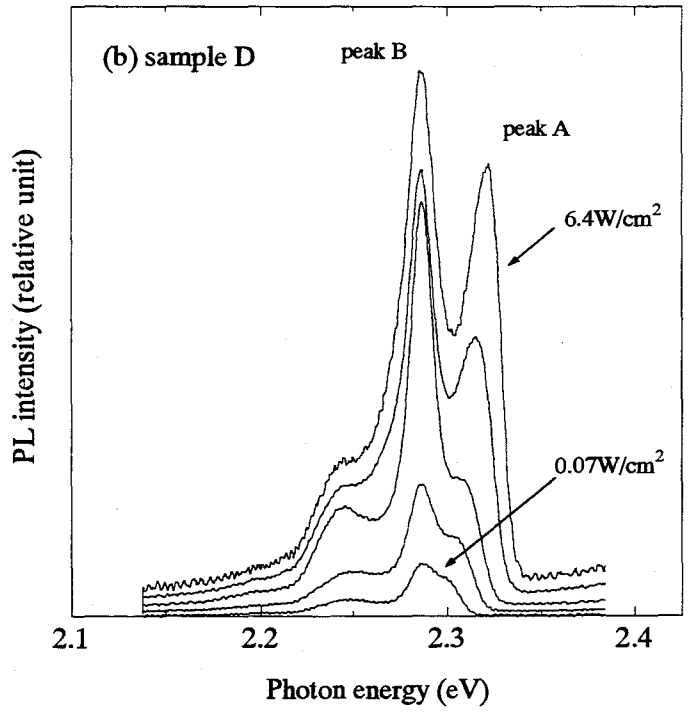
(b) sample D
peak B
peak A
6.4W/cm2
0.07W/cm2
PL intensity (relative unit)
2.1
2.2
2.3
2.4
Photon energy (eV)

Fig. 6.2

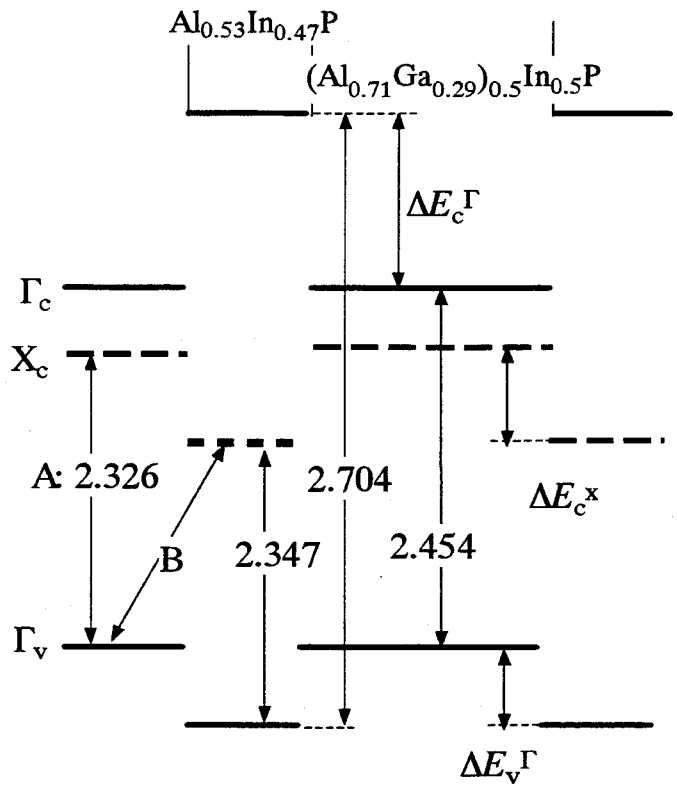
$Al_{0.53}In_{0.47}P$
$(Al_{0.71}Ga_{0.29})_{0.5}In_{0.5}P$
ΔE_c^{Γ}
Γ_c
X_c
A: 2.326
2.704
ΔE_c^{X}
B
2.347
2.454
Γ_v
ΔE_v^{Γ}

Fig. 6.3

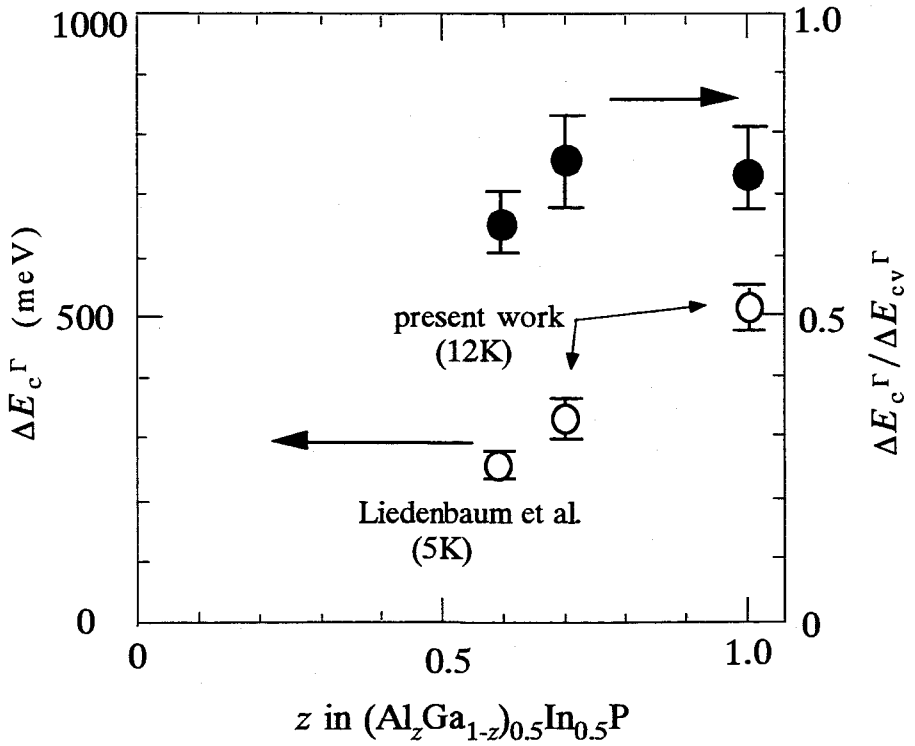
1000
500
0
1.0
0.5
0
0
0.5
1.0
ΔE_c^{Γ} (meV)
$\Delta E_c^{\Gamma} / \Delta E_{cv}^{\Gamma}$
present work
(12K)
Liedenbaum et al.
(5K)
z in $(Al_zGa_{1-z})_{0.5}In_{0.5}P$

Fig. 6.4

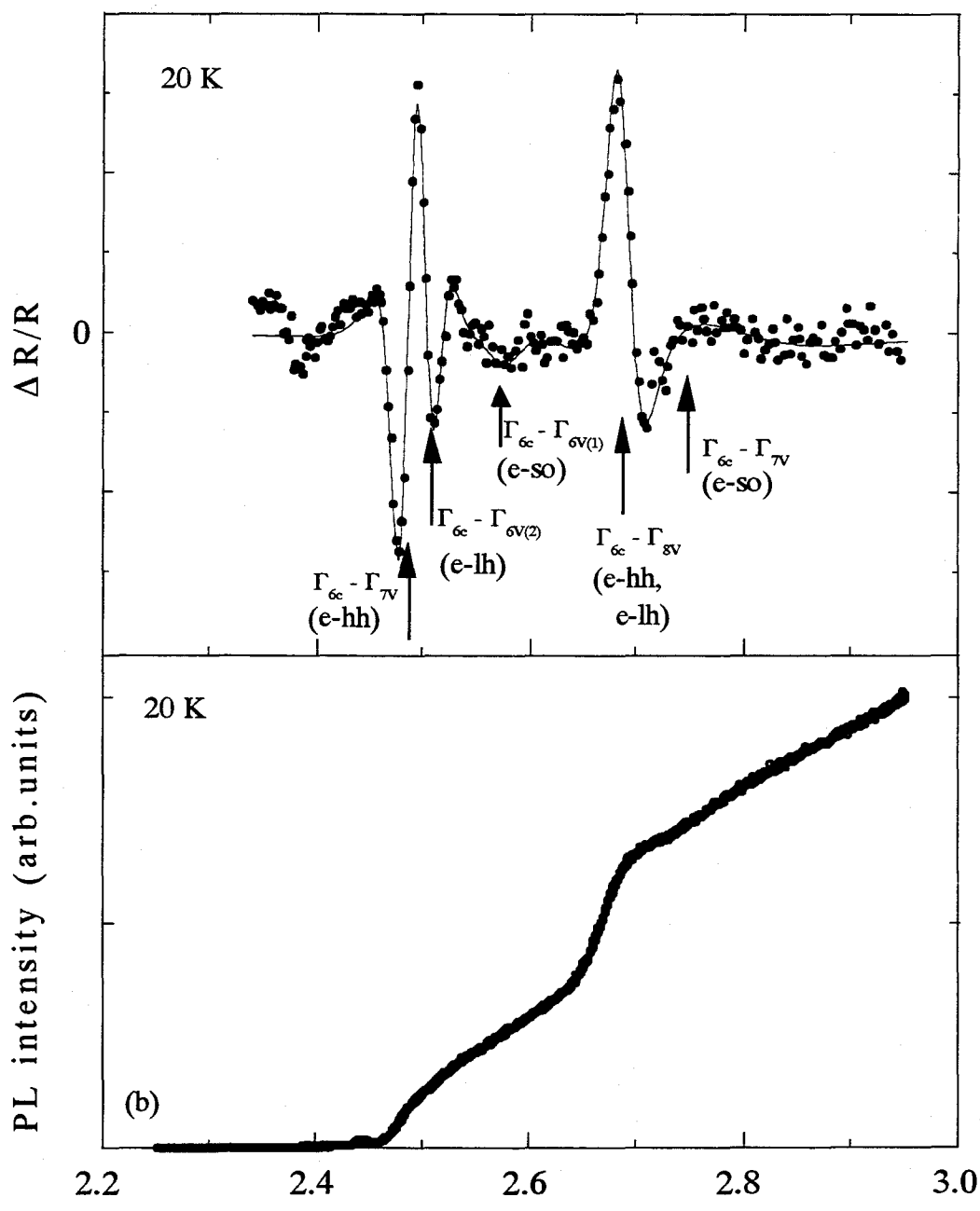
20 K
ΔR/R
0
Γ6c - Γ6V(1)
(e-so)
Γ6c - Γ7V
(e-so)
Γ6c - Γ6V(2)
(e-lh)
Γ6c - Γ8V
(e-hh,
e-lh)
Γ6c - Γ7V
(e-hh)
20 K
PL intensity (arb.units)
(b)
2.2
2.4
2.6
2.8
3.0

Fig. 6.5

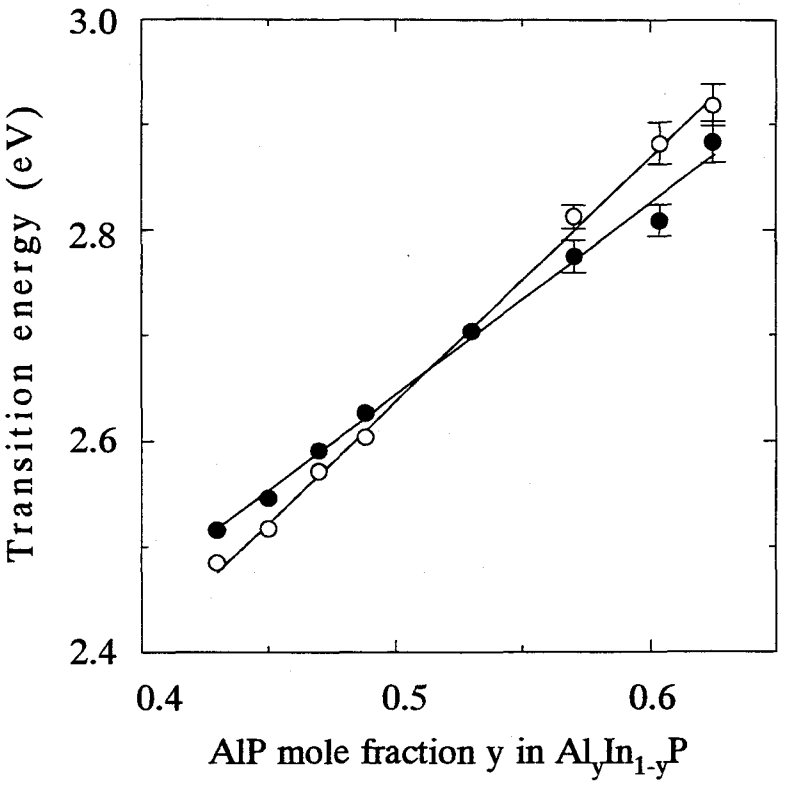
3.0
2.8
2.6
2.4
Transition energy (eV)
0.4
0.5
0.6
AlP mole fraction y in $Al_yIn_{1-y}P$

Fig. 6.6

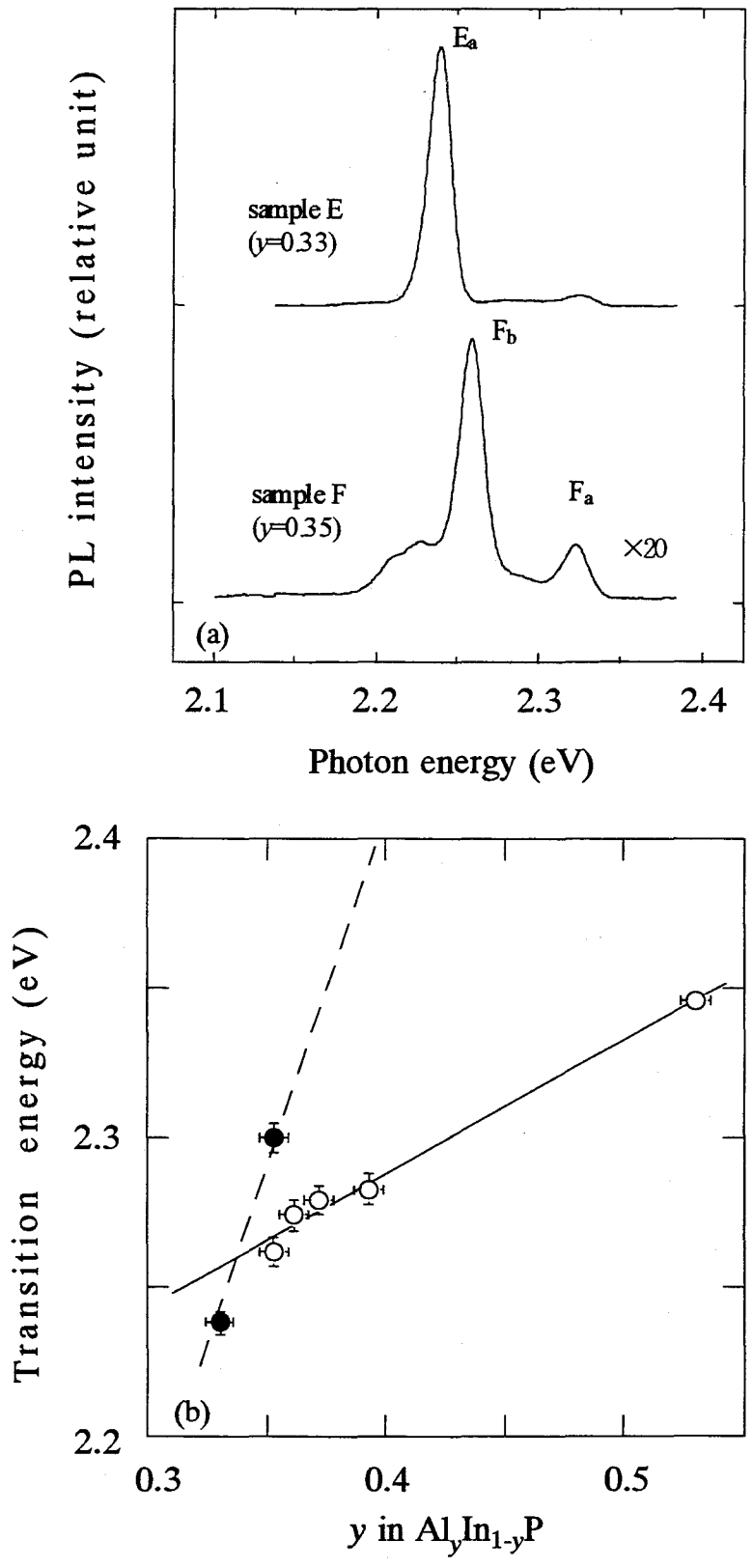
PL intensity (relative unit)
E_a
sample E
(y=0.33)
F_b
sample F
(y=0.35)
F_a
×20
(a)
2.1
2.2
2.3
2.4
Photon energy (eV)
Transition energy (eV)
2.4
2.3
2.2
(b)
0.3
0.4
0.5
y in $Al_yIn_{1-y}P$

Fig. 6.7

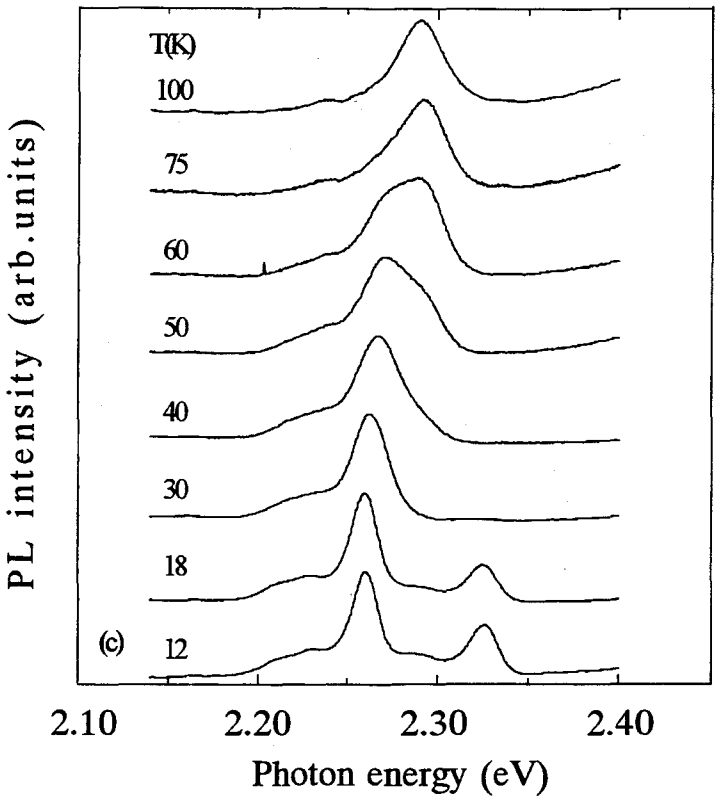
T(K)
100
75
60
50
40
30
18
12
(c)
PL intensity (arb.units)
2.10
2.20
2.30
2.40
Photon energy (eV)

Fig. 6.7

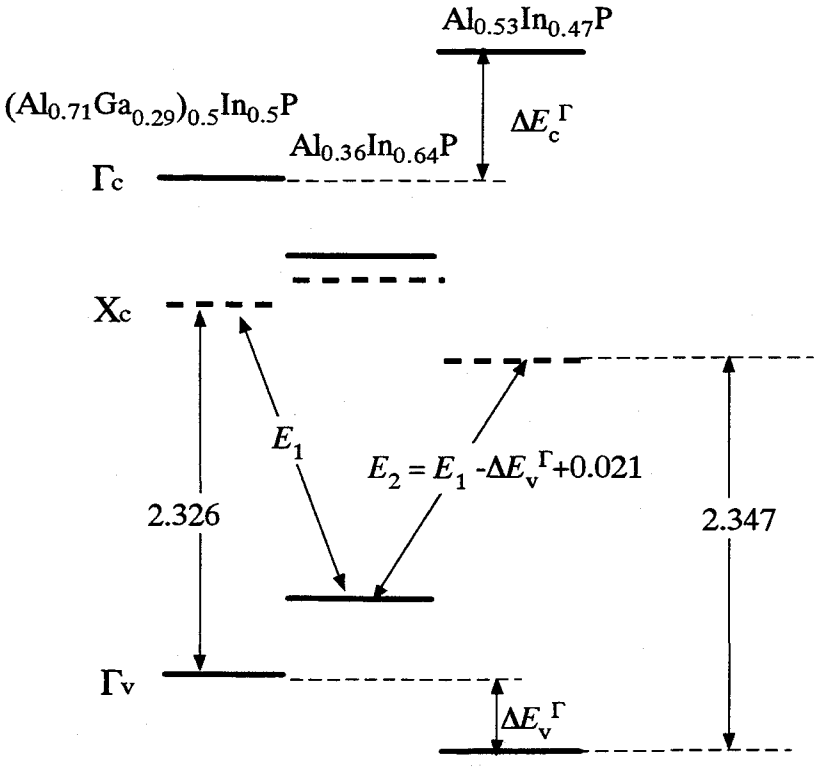
$Al_{0.53}In_{0.47}P$
$(Al_{0.71}Ga_{0.29})_{0.5}In_{0.5}P$
$Al_{0.36}In_{0.64}P$
ΔE_c^{Γ}
Γ_c
X_c
E_1
$E_2 = E_1 - \Delta E_v^{\Gamma} + 0.021$
2.326
2.347
Γ_v
ΔE_v^{Γ}

Fig. 6.8

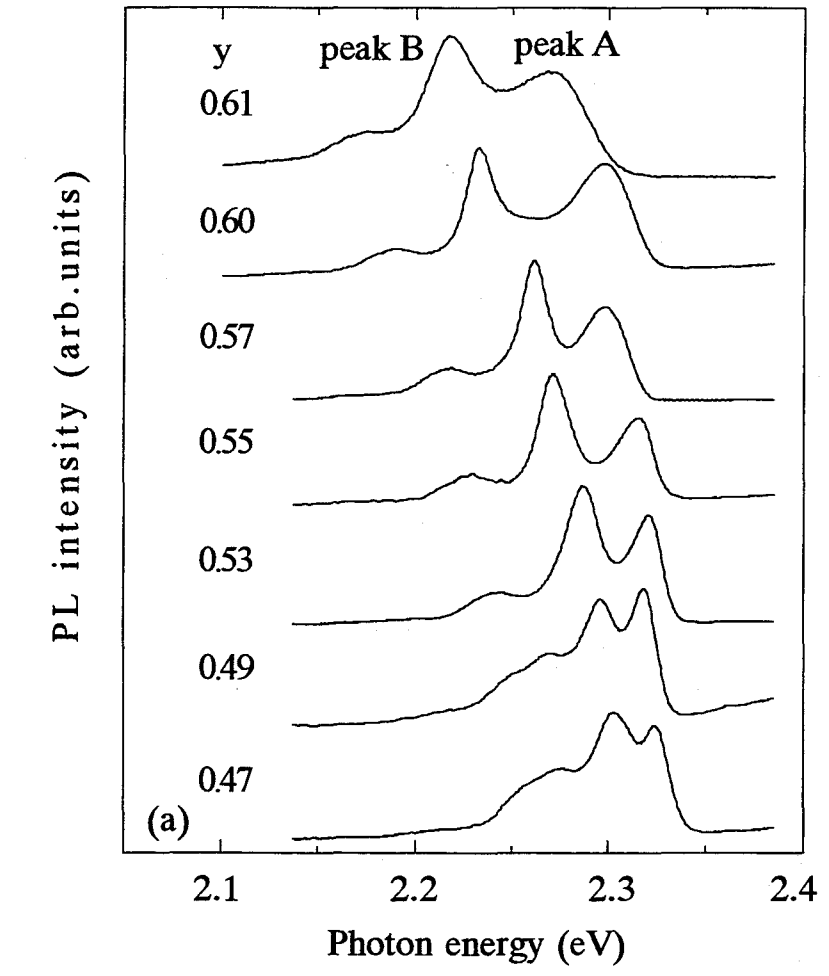
y
peak B
peak A
0.61
0.60
0.57
0.55
0.53
0.49
0.47
(a)
PL intensity (arb.units)
2.1
2.2
2.3
2.4
Photon energy (eV)

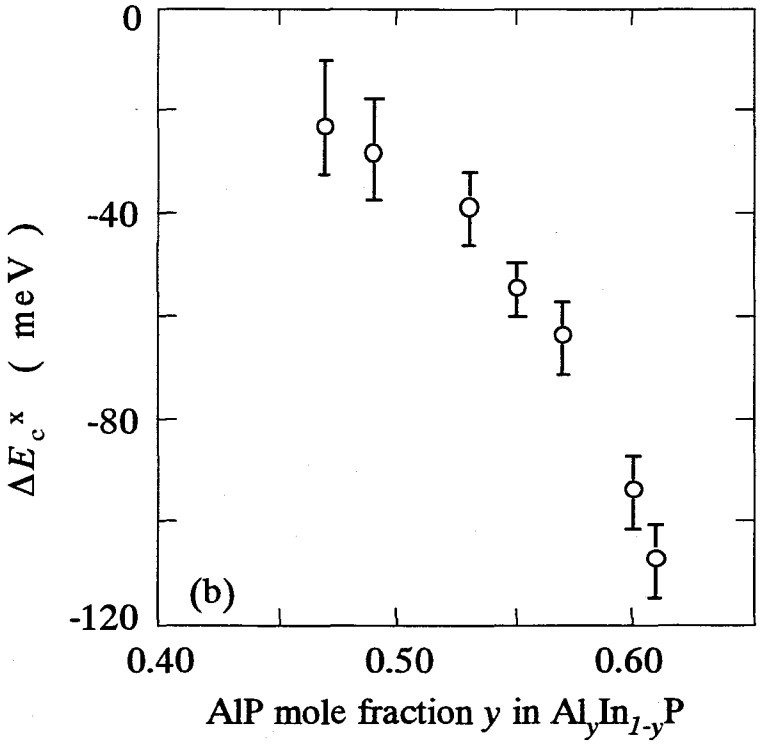
0
-40
-80
-120
(b)
0.40
0.50
0.60
$\Delta E_c^{\ x}$ (meV)
AlP mole fraction y in $Al_yIn_{1-y}P$

Fig. 6.9

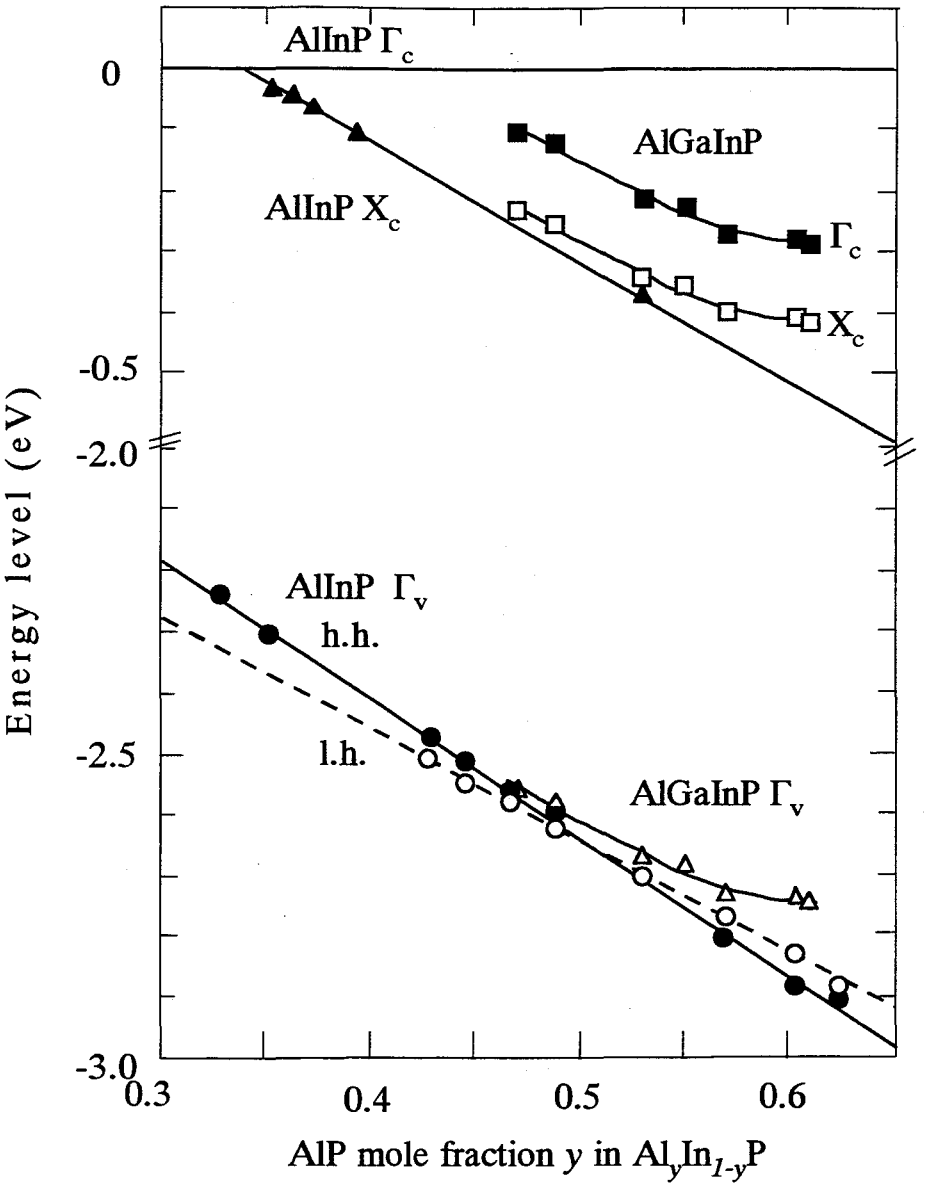
AlInP Γ_c
0
AlGaInP
AlInP X_c
Γ_c
X_c
-0.5
-2.0
AlInP Γ_v
h.h.
l.h.
-2.5
AlGaInP Γ_v
-3.0
0.3
0.4
0.5
0.6
Energy level (eV)
AlP mole fraction y in $Al_yIn_{1-y}P$

Fig. 6.10

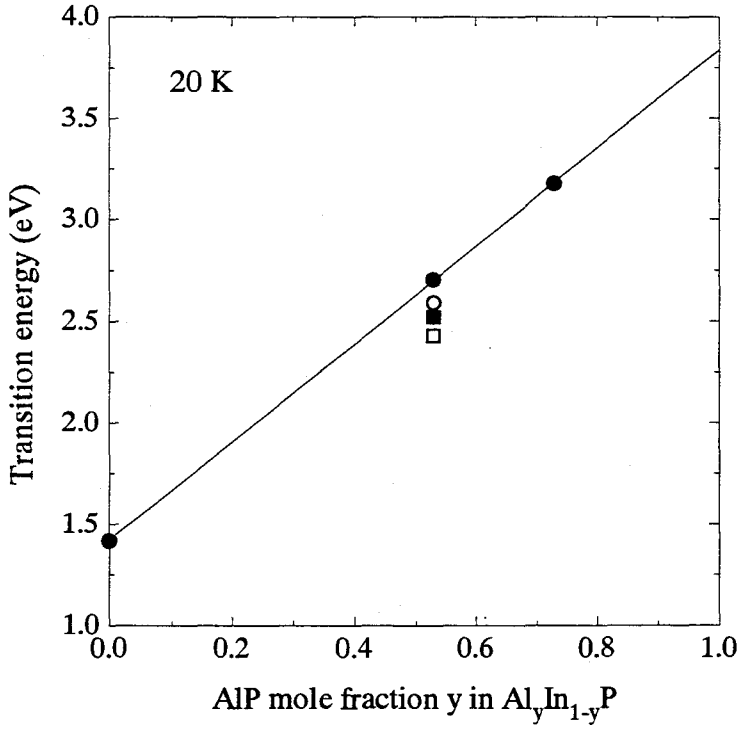
20 K
Transition energy (eV)
AlP mole fraction y in $Al_yIn_{1-y}P$
4.0
3.5
3.0
2.5
2.0
1.5
1.0
0.0
0.2
0.4
0.6
0.8
1.0

Fig. 6A.1

Chapter VII

Temperature dependence of the photoluminescence intensity from the AlGaInP/GaInP-quantum well structures

Abstract

The photoluminescence (PL) spectra of Al(Ga)InP/GaInP-quantum well structures by continuous excitation condition have been measured in the temperature range of 10 - 450 K. Carriers have been generated only in the wells with a constant rate at all the temperatures. The temperature dependence of the PL intensity has been fitted by a model function: Besides the radiative recombination carrier extinction is caused by two processes with respective threshold energies; the first gives a slight decrease in 10 - 200 K, and the second gives a rapid decrease at higher temperatures. The higher threshold energies are consistent with the barrier hights in the energy alignment schemes of these heterostructures. For the quantum wells sandwiched by the $Al_yIn_{1-y}P$ (y = 0.47, 0.53, or 0.60) barrier layers as the Γ_c - Γ_v transition energy of $Al_yIn_{1-y}P$ increases, the carrier leak to the quaternary layers is reduced; i.e., the barrier layers produce effective larger band offsets.

7.1 Introduction

The efficiency of radiative recombination of carriers or the carrier confinement characteristics in quantum wells (QWs) are reflected in the temperature dependence of the photoluminescence (PL) intensity, and it has been investigated by many workers. Studies on bulk-ordered AlGaInP and GaInP showed the existence of localized energy states.[1)-3)] The non-radiative carrier extinction processes were studied for AlGaAs/GaAs-QWs by Gurioli *et al.*, [4)] for InGaAs/GaAs-QWs by Bacher *et al.*,[5)] and for AlGaInP/GaInP-QWs by Michler *et al.*.[6)] These studies are based on the PL measurement with continuous excitation or the time resolved (TR) PL measurement subsequent to short pulse excitation. In these studies the non-radiative carrier extinction is attributed to the leak from QWs to barrier layers. In the experiments with continuous excitation the carriers were generated in the barrier layers as well as in the well layers.[3)4)] The temperature dependence of the excitation efficiency was not taken into consideration. In all the studies mentioned above the alloys were of direct transition nature, and only the Γ valley (well) - Γ valley (barrier) transition was involved. The AlP mole fraction of cladding layers in AlGaInP red-light-emitting laser diodes is around the crossover of the Γ_c and X_c points or higher,[7) 8)] so that the carriers in the QW layers may leak into the X_c valleys of the cladding layers (Chap.V and VI). To date, there is few reports on the X_c-Γ_c carrier transition phenomenon for the AlGaInP alloys. In Chaps.V and VI I have examined the energy band alignment schemes at the Γ_c, Γ_v, and X_c points for disordered $Al_{0.53}In_{0.47}P/Ga_{0.52}In_{0.48}P$ and disordered $Al_yIn_{1-y}P/(Al_{0.71}Ga_{0.29})_{0.5}In_{0.5}P$ ($0.47 \leq y \leq 0.62$) heterostructures, respectively. On the basis of these band alignment schemes both for the X_c and Γ points, in this chapter the temperature dependence of the PL intensities for Al(Ga)InP/ GaInP/Al(Ga)InP QWs is investigated.

7.2 Experimental

I grew the undoped samples by the MOVPE system. The generation of an LRO structure was prevented by using the GaAs substrates with a (511)A surface orientation and a growth temperature of 720°C. The net carrier concentration measured by the chemical capacitance-voltage technique was 2×10^{15} cm^{-3} of the n-type.

Two kinds of samples were prepared. Samples A and B had a single-barrier structure and samples C, D, E, and F had double-barrier structures (separate confinement heterostructure (SCH) with quantum well active layers). The energy band alignment (at

12 - 20 K) and thickness of the layers in these samples are illustrated in Fig. 7.1. The structure of sample A is $(Al_{0.56}Ga_{0.44})_{0.5}In_{0.5}P$ /[$Ga_{0.37}In_{0.63}P$/ $(Al_{0.56}Ga_{0.44})_{0.5}In_{0.5}P$-triple-quantum-wells (TQWs)]/$(Al_{0.56}Ga_{0.44})_{0.5}In_{0.5}P$, and that of sample B is $Al_{0.53}In_{0.47}P$/ [$Ga_{0.52}In_{0.48}P$/$Al_{0.53}In_{0.47}P$-TQWs]/$Al_{0.53}In_{0.47}P$. In sample A, the alloy composition of the barrier layers is near the crossing point of the Γ_c and the X_c points as indicated in Fig. 1.3. In sample B, the barriers have an indirect energy gap at all the measurement temperatures (10 - 450 K). The structures of the double-barrier samples are as follows. Sample C consists of $(Al_{0.71}Ga_{0.29})_{0.5}In_{0.5}P$/[$(Al_{0.56}Ga_{0.44})_{0.5}In_{0.5}P$/$Ga_{0.37}In_{0.63}P$-TQWs]/$(Al_{0.71}Ga_{0.29})_{0.5}$ $In_{0.5}P$. Samples D, E, and F have 6-nm $Al_yIn_{1-y}P$ barrier layers with different alloy compositions: $(Al_{0.71}Ga_{0.29})_{0.5}In_{0.5}P$/$Al_yIn_{1-y}P$/[$(Al_{0.56}Ga_{0.44})_{0.5}In_{0.5}P$/$Ga_{0.37}In_{0.63}P$-TQW]/ $Al_yIn_{1-y}P$/$(Al_{0.71}Ga_{0.29})_{0.5}In_{0.5}P$. The AlP mole fraction y in the $Al_yIn_{1-y}P$ layers is 0.47 for sample D, 0.53 for sample E, and 0.60 for sample F. The well width is 10 nm for all the samples. The band offsets shown in Fig. 7.1 are based on the previous chapters and Liedenbaum *et al.*[9], and numerical values are given in Table 7-I. As the temperature increases from 20 K to 300 K (refs.10, 11, and Fig. 4.4) the total band offset ΔE_{cv}^{Γ} ($\Delta E_c^{\Gamma}+\Delta E_v^{\Gamma}$) decreases by about 25 meV, and ΔE_{cv}^{X} ($\Delta E_c^{X}+\Delta E_v^{\Gamma}$) increases by about 100 meV.

For sample B the 515-nm line (2.41 eV) of the Ar^+ laser was used to excite only the $Ga_{0.52}In_{0.48}P$ QW layers, and for samples A, C, D, E, and F the 633-nm line (1.96 eV) of the He-Ne laser was used to excite only the $Ga_{0.37}In_{0.63}P$ QW layers. I chopped the excitation beams at 280 Hz; the pulse duration was about 1.5 ms. The laser power in front of the cryostat was 420 μW at 10 - 20 K. The generated carrier density is estimated to be the order of 10^{12} - 10^{13} cm^{-3} with the carrier life time of 1- 10 ns [6] and the absorption coefficient of $5\times10^4 cm^{-1}$. [12] The excitation light was incident on a 600-μm-diameter region of the samples. An example of the temperature dependence of the PL spectra (for sample C) is shown in Fig. 7.2. The PL intensities drop completely to the base line before reaching the energy 1.96 eV of the excitation line.

By adjusting the excitation beam power I obtained the PL spectra with a constant carrier generation rate for all the temperature range. The procedure is: Sample C is taken as an example. The temperature dependence of the carrier generation efficiency by the laser beam was estimated from the PLE spectrum at low temperature. Figure 7.3(a) shows the PLE spectrum at 20 K, where the monitored wavelength is 659 nm (1.881 eV). The inset shows the PL spectrum at 12 K. (See Fig. 7. 2) The peaks of the electron-heavy hole transition and that of the electron-light hole transition are denoted with "hh" and "lh", respectively. The sharp peak located at the lower energy side of hh is due to the excitation beam scattered from the sample at the monitored wavelength.

The PL intensity of the PLE signal at this low temperature is assumed to be proportional to the number of carriers generated. The transition energies E_{cv}^{Γ} in the ranges of 10 - 300 K and 300 - 450 K were determined using the photoreflectance (PR) method and PL method, respectively. Figure 7.3(b) shows the result, where the energy gap at 12 K is taken as the base line and the relative decrease in the transition energy is plotted. It is assumed that, as the temperature increases, the PLE profile shifts to lower energy according to the decrease in the transition energy without deformation except for the absorption edge.[13] Since E_{cv}^{Γ} decreases by 135 meV as the temperature increases from 12 to 400 K, the excitation energy may be regarded to shift, in effect, to a higher one by 135 meV, as shown by the doted line. The carrier generation efficiency at 400 K is thus estimated to be about twice that at 20 K. The power density of the excitation beam at each temperature was adjusted to be inversely proportional to the PLE intensity in Fig. 7.3(a). The PL intensity was obtained as the total number of photons in a spectrum (the area under the peak ; see Fig. 7.2). The wavelength dependence of the reciprocal dispersion of the monochromator was about 3% in the measured wavelength range, hence this effect was neglected. The obtained temperature dependence of the PL intensity is shown in Fig. 7.4. At low temperatures, the PL intensities for all the samples are stable, but above 300 K they decrease rapidly.

7.3 Results and discussion

7.3.1 Model function of the temperature dependence of the PL intensity

The temperature dependence is analyzed by using rate equations for the density of electron-hole pairs. In the PL spectra at high temperature 400 K, PL intensity vanishes at the energy about 100 - 200 meV higher than the peak energy, indicating no carriers in higher energy states. This result indicates that although there are many states in the GaInP wells, the carrier leak takes place directly from the low-energy states in the QWs to the states in the barrier or cladding layers, not by the ladder-like processes via the upper levels in the wells. A two-level model is used: the bottom of the quantum wells (level 1) and the bottom of the barrier or cladding layers (level 2). The elementary processes taken into consideration are (1) electron-hole recombination with radiation which is observed in PL measurements, (2) the excitation from localized states and the subsequent non-radiative recombination or the recombination via deep levels, and (3) excitation or deexcitation from the states in the QWs, barrier, or cladding layers. The rate equations are

$$\frac{d\delta n_1}{dt} = -A_1{}^0\,\delta n_1 - A_1{}^1\delta n_1 - F_{12}\,\delta n_1 + F_{21}\,\delta n_2 + L_1. \tag{7-1}$$

$$\frac{d\delta n_2}{dt} = -A_2{}^0\,\delta n_2 - A_2{}^1\delta n_2 - F_{21}\,\delta n_2 + F_{12}\,\delta n_1 - F_2{}^0\delta n_2 + L_2. \tag{7-2}$$

Here, δn_1 and δn_2 are the densities of electron-hole pairs in level 1 and 2, respectively. A_i^0 (i = 1, 2) is the radiative recombination probability for an electron-hole pair in state i. A_i^1 is the non-radiative recombination rate. F_{ij} is the rate of a transition from state i to state j; for example, F_{12} is for carrier leak from quantum wells (i = 1) to barrier or cladding layers (j = 2). F_2^0 is for the carrier leak from the cladding or barrier layer to the GaAs substrate. The carrier injection from the substrate to the barrier or cladding layer is neglected. L_i is the generation rate of electron-hole pairs in state i by the laser irradiation.

In my experiment, L_2 = 0 because of the selective excitation in the wells, and $\frac{d\delta n_1}{dt} = \frac{d\delta n_2}{dt} = 0$ under the stationary condition. The back diffusion of carriers emitted into barrier or cladding layers ($F_{21}\,\delta n_2$) is neglected ($\delta n_1 >> \delta n_2$). Thus the PL intensity is expressed as

$$I_{PL} \propto A_1{}^0 \cdot \delta n_1$$

$$= \frac{1}{1 + \frac{A_1{}^1}{A_1{}^0} + \frac{F_{12}}{A_1{}^0}} L_1. \tag{7-3}$$

The potential energy for localization is given as the difference between the PL peak energy and the hh peak energy in the PLE spectra (~ 10 meV in Fig. 7.3). The localization energy and the total band offset between the well layers and the barrier or cladding layers are assumed to be the threshold energies for the carrier extinction processes, and are denoted by E_{11} and E_{12}, respectively. With the assumption that $A_1{}^0$ is independent of temperature, the following expressions are adopted.

$$\frac{A_1{}^1}{A_1{}^0} = G_{11} \cdot \exp(-E_{11} / k_b T) \tag{7-4}$$

$$\frac{F_{12}}{A_1{}^0} = G_{12} \cdot \exp\,(-E_{12} / k_b T) \tag{7-5}$$

By substituting eqs.(7-4) and (7-5) into eq.(7-3) we obtain the following formula.

$$I_{PL}(T) = \frac{I_0}{1 + \sum_{i}^{2} G_{1i} \exp(-E_{1i} / k_b T)}, \qquad (7\text{-}6)$$

where I_0 is the PL intensity at 0 K.

The result of the fitting is shown in Fig. 7.4. The best fit values of E_{11} and G_{11} are listed in Table 7-II. The ambiguity in E_{11} is 3 - 10 meV. The best fit parameters E_{12} and G_{12} are shown in Fig. 7.5.

We now discuss the validity of our assumption that A_1^0 is constant against temperature. With use of the energy dependence of the matrix element of the electron-hole recombination[14] the temperature dependence of A_1^0 was calculated as due to the enhancement of diffusion of carriers in the **k**-space with the increase in temperature. Here, step functions are adopted as density of states of QWs. For the $(Al_{0.56}Ga_{0.44})_{0.5}In_{0.5}P$ /$Ga_{0.37}In_{0.63}P$ - QW the ratio of the probability at a temperature T to that at 400 K is found to be 1.03 at T = 300 K, 1.06 at 200 K and 1.19 at 100 K. For $Al_{0.53}In_{0.47}P$/ $Ga_{0.52}In_{0.48}P$ - QW the ratio is found to be 1.03 at 300K, 1.13 at 200 K, and 1.26 at 100 K. The change is too small to affect our experiment (Fig. 7.4). A_1^0 may be affected by carrier localization which may take place at temperatures lower than 150 K. For a $Ga_{0.52}In_{0.48}P$(1.4μm)/$Al_{0.53}In_{0.47}P$(120nm)/GaAs structure, which is known to have smaller potential fluctuation, the temperature dependence of I_{PL} is found to be the same with that of sample B in this temperature range. This fact suggests that the effect is rather minor. In my present experiment, I_{PL} is constant in the range of 10 - 50 K for all samples and of 150 - 275 K for sample B and sample F, which has the highest barriers. These facts support that A_1^0 is independent of temperature in these temperature ranges.

7.3.2 Small decrease in the PL intensity in the 10 - 200 K range

The obtained E_{11} (8 - 20 meV) are consistent with the energy difference between the PL peak and the hh peak (8 - 10 meV).

For sample B the decrease in the PL intensity at low temperatures or G_{11} is larger than those for other samples. It is known that alloys with higher AlP mole fraction tend to have higher density of nonradiative recombination centers.[15] This fact may explain the large decrease: larger non-radiative transition rates of the carriers that are free from

localization.

The temperature dependence of the PL intensity has a part almost constant in the temperature range of 175 - 275 K. This indicates that above 175 K the excitation of carriers from the localized states to free states takes place almost completely.

7.3.3 Relation between the best fit parameters E_{12} and G_{12} and the band energy alignment

Figure 7.5 shows the parameters E_{12} and G_{12} obtained from the fitting. For sample A, the effective band offset E_{12} is 500 (±50) meV. Table 7-I shows that the total band offsets between the wells and barriers are 500 meV for the Γ_c-Γ_v energy gap and 425 meV for the X_c-Γ_v energy gap at 12 - 20 K.

For sample B, the total band offsets between the wells and barriers are 680 meV for Γ_c-Γ_v and 325 meV for X_c-Γ_v. The obtained best fit parameter E_{12} of 545 (±50) meV is between these two values. In Chap. V photoluminescence of the X_c (AlInP) - Γ_v (GaInP) transition in an AlInP/GaInP(2 nm)/AlInP QW structure was observed. These two results suggest that the carrier leak from Γ_c(wells) to X_c (barriers) is comparable with that from Γ_c(wells) to Γ_c (barriers) at high temperatures. The carrier leak processes in samples A and B are schematically illustrated in Fig. 7.6(a). Transition rates are expressed qualitatively by the thickness of the arrows.

For sample C, the largest band offset at the Γ point is 570 meV: the band offset between the $Ga_{0.37}In_{0.63}P$ and $(Al_{0.71}Ga_{0.29})_{0.5}In_{0.5}P$ layers. The sum of the band offsets at the X_c and Γ_v points between the $Ga_{0.37}In_{0.63}P$ and $(Al_{0.71}Ga_{0.29})_{0.5}In_{0.5}P$ layers is 435 meV. The best fit parameter 540 (+50,−10) meV agrees with the band offset of the $Ga_{0.37}In_{0.63}P/(Al_{0.71}Ga_{0.29})_{0.5}In_{0.5}P$ layer within the experimental uncertainty.

In sample D, the band offset between the $Al_{0.47}In_{0.53}P$ and the $(Al_{0.71}Ga_{0.29})_{0.5}In_{0.5}P$ layers is almost zero at the Γ_v point and 110 meV at the Γ_c point. The X_c energy level in the $Al_{0.47}In_{0.53}P$ layer is located lower than that in the $(Al_{0.71}Ga_{0.29})_{0.5}In_{0.5}P$ layer by 20 meV. The barrier heights at the Γ point for samples E and F are higher than that of sample C by 250 and 370 meV, respectively. The obtained E_{12} values are qualitatively consistent with the y dependence of E_{cv}^{Γ} of the $Al_yIn_{1-y}P$ alloy or of the band offsets between the $Al_yIn_{1-y}P$ layers and the QW layers. The quantitative disagreements may be ascribed to the carrier leakage to the X_c states or tunneling through the thin AlInP layers. The G_{12}s for samples E and F are larger than those for the other samples. This is ascribed partly to tunneling too. A schematic illustration of the dominant carrier leak processes in this sample group is shown in Fig. 7.6(b). These carrier leak processes from the bottom of QWs to barrier or cladding layers may take place with the multi-phonon absorption. In

fact the multi-phonon processes are observed in Si or Ge. [16) 17)]

From the larger intensities of sample E and F in the range of 300 - 400 K or their larger E_{12}, it is concluded that although $Al_yIn_{1-y}P$ layers have the X_c point as the lowest energy level in the conduction band, the layers with y of 0.53 and 0.60 work as effective barriers for carrier confinement.

References

1) K. Yamashita, T. Kita, H. Nakayama, and T. Nishino, Phys. Rev.B, 53, 15713 (1995)
2) F. A. J. M. Drissen, G. J. Bauhuis, S. M. Olsthoorn, and L. J. Giling, Phys. Rev. B 48, 7889 (1993)
3) K.Yamashita, T.Kita, H.Nakayama, and T.Nishino, Phys.Rev.B, 55, 4411(1997)
4) M. Gurioli, A. Vinattieri, M. Colocci, C. Deparis, J. Massies, G. Neu, A. Bosacchi, and S. Franchi, Phys. Rev. B 44, 3115 (1991)
5) G. Bacher, H. Schweizer, J. Kovac, A. Forchel, H. Nickel, W. Schlapp, and R. Losch, Phys. Rev. B 43, 9312 (1991)
6) P. Michler, A. Hangleiter, M. Moser, M. Geiger, and F. Scholtz, Phys. Rev. B 46, 7280 (1992)
7) A.Valster, C.J.Van der Poel, M.N.Finke, and M.J.B.Boermans, Electron.Lett., 28, 144 (1992)
8) T.Tanaka, H.Yanagisawa, M.Takimoto, and S.Minagawa, Electron.Lett., 29, 1864 (1993)
9) C. T. H. F. Liedenbaum, A. Valster, A. L. G. J. Severens, and G. W. 'tHooft, Appl. Phys. Lett. 57, 2698 (1990)
10) A. Onton and R. J. Chicotka, J. Appl. Phys. 41,4205 (1970)
11) R. J. Nelson and N. Holonyak, Jr., Phys. Chem. Solids 37, 629 (1975)
12) M.Moser, C.Geng, E.Lach, I.Queisser, F.Scholz, H.Schweizer, and A.Drönen, J.Cryst.Growth 124, 133 (1992)
13) H. Iwamura, H. Kobayashi, and H. Okamoto, Jpn. J. Appl. Phys. 23, L795 (1984)
14) M.Yamanishi and I.Suemune, Jpn.J.Appl.Phys. 23, L35 (1984)
15) K.Sugiura, K.Domen, M.Sygawara, C.Anayama, M.Kondo, T.Tanahashi, and K.Nakajima, J.Appl.Phys. 70, 4946,(1991)
16) P.Y.Yu and M.Cardona, "Fundamentals of semiconductors", Springer, Berlin, 1995
17) J.I.Pankove, "Optical processes in semiconductors", Prentice-Hall, London, 1971

Table 7-I Band offsets (in meV) at the heterojunctions and sum of the band offsets at 12 - 20 K for samples A - F.

sample name	A	B	C	D	E	F
ΔE^{Γ}_{c}	325	495	400	510	590	620
ΔE^{X}_{c}	250	140	265	240	225	170
ΔE^{Γ}_{v}	175	185	170	170	230	320
$\Delta E^{\Gamma}_{c}+\Delta E^{\Gamma}_{v}$	500	680	570	680	820	940
$\Delta E^{X}_{c}+\Delta E^{\Gamma}_{v}$	425	325	435	410	455	490

Table 7-II Best fit parameters of E_{11} and G_{11}.

sample	A	B	C	D	E	F
E_{11} (meV)	12	20	15	8	12	20
G_{11}	3.6×10^{-1}	3.9	3.9×10^{-1}	1.6×10^{-1}	5.6×10^{-1}	2.5×10^{-1}

Figure captions

Fig. 7.1 Band energy alignment of the QW structures; (a) sample A, (b) sample B, (c) sample C, and (d) sample E. The schemes for samples D and F are similar to that of E. The thickness of a cladding layer is 200 nm for all the samples. The solid and dashed lines are the band extremes at the Γ points and at the X_c point, respectively.

Fig. 7.2 PL spectra for sample C. The crystal temperature is varied from 12 to 400 K. The maximum intensity is normalized to the same value for all temperatures.

Fig. 7.3 Variation in excitation efficiency with an increase in temperature.
(a) PLE spectra for sample C measured at 20 K. The photoluminescence intensity is monitored at the photon energy of 1.881 eV. The PL spectrum at 12 K is shown in the inset. The relative excitation position shifts from 1.96 eV to 2.09 eV as crystal temperature increases from 20 to 400 K. (b) Decrease in the Γ_c-Γ_v transition energy with temperature.

Fig. 7.4 Dependence of integrated PL intensity on temperature.
A PL intensity is calculated as the total number of photons in a PL spectrum. The solid curves are the respective best fit functions using eq.(7-6).

Fig. 7.5 Best fit parameters E_{12} and G_{12} for the carrier leak process.
The effective barrier heights E_{12} for sample A, B, and C agree well with the band energy alignment schemes shown in Table 7-I. E_{12}s for sample C, D, E, and F have qualitative agreement with the y dependence of E_{cv}^{Γ} for $Al_yIn_{1-y}P$.

Fig. 7.6 Schematic illustrations of the dominant carrier leak processes.
The thicker the arrow, the larger the transition rate.
(a) For single barrier structures (sample A and B).
(b) For double barrier structures (sample C, D, E, and F).

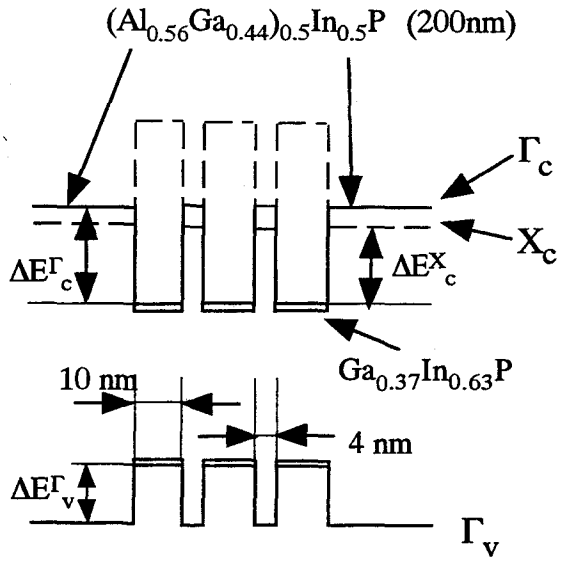

(a) Sample A

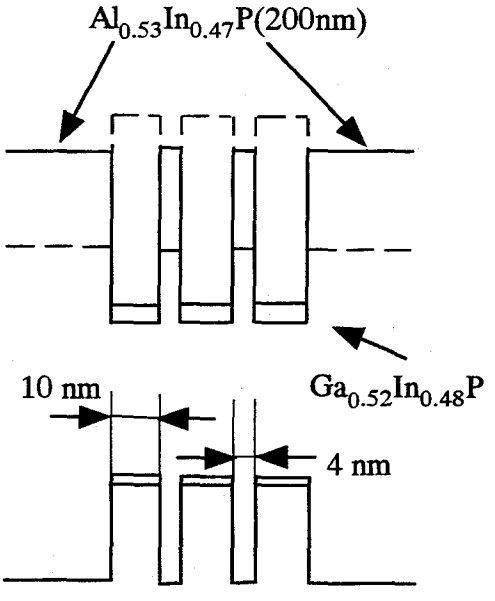

(b) Sample B

Fig. 7.1(a), (b)

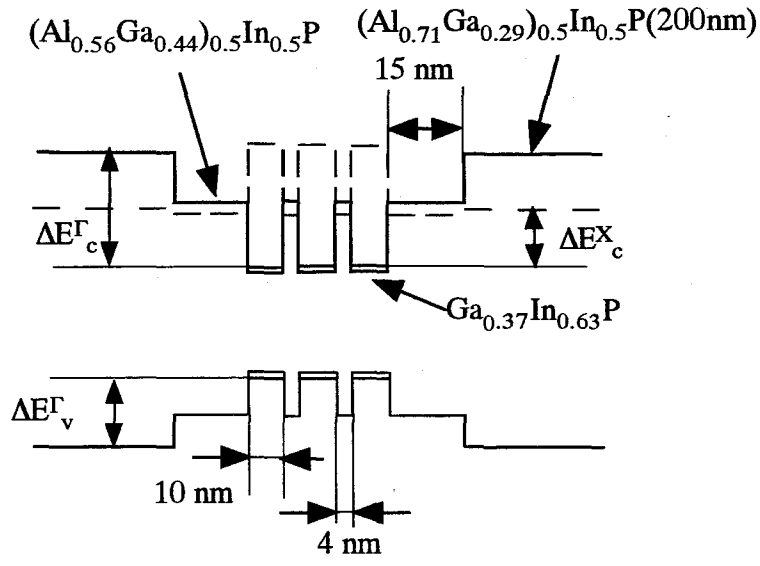

(c) Sample C

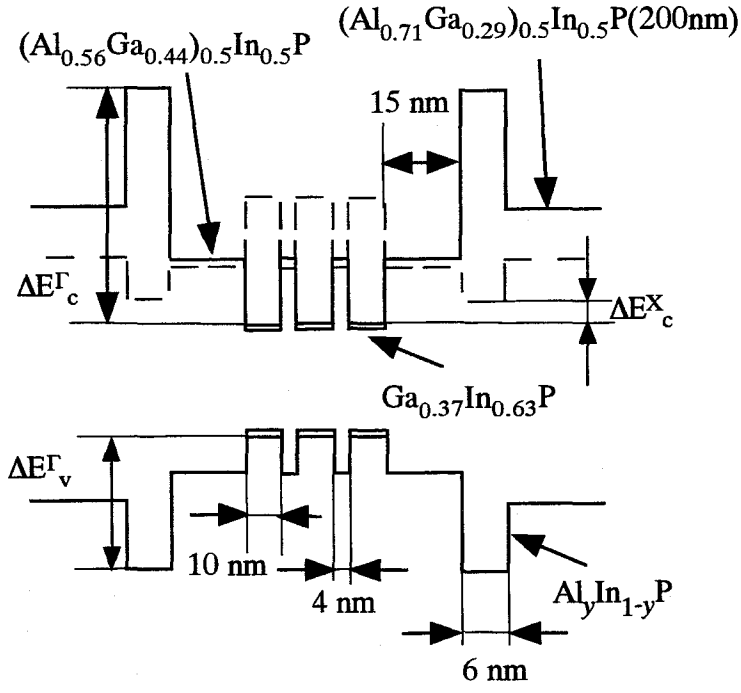

(d) Sample D, E, F

Fig. 7.1(c), (d)

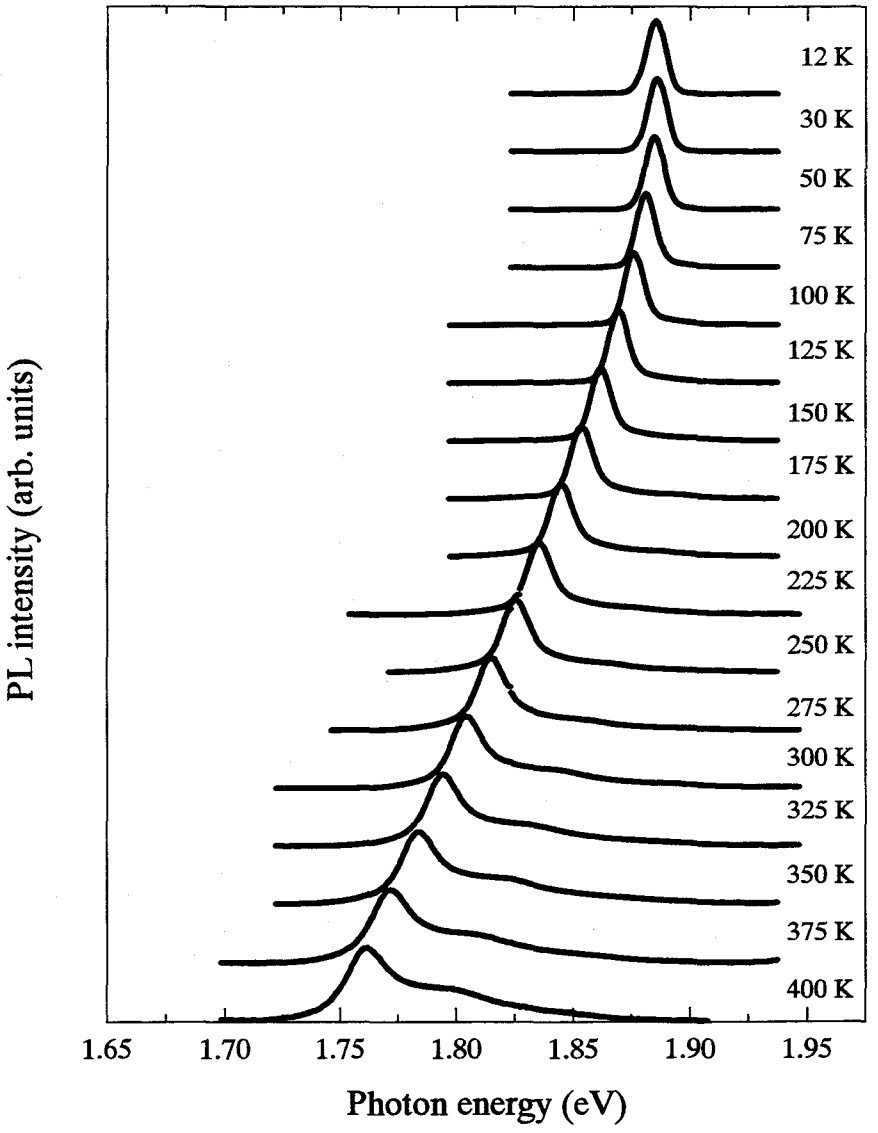
12 K
30 K
50 K
75 K
100 K
125 K
150 K
175 K
200 K
225 K
250 K
275 K
300 K
325 K
350 K
375 K
400 K
PL intensity (arb. units)
1.65
1.70
1.75
1.80
1.85
1.90
1.95
Photon energy (eV)

Fig. 7.2

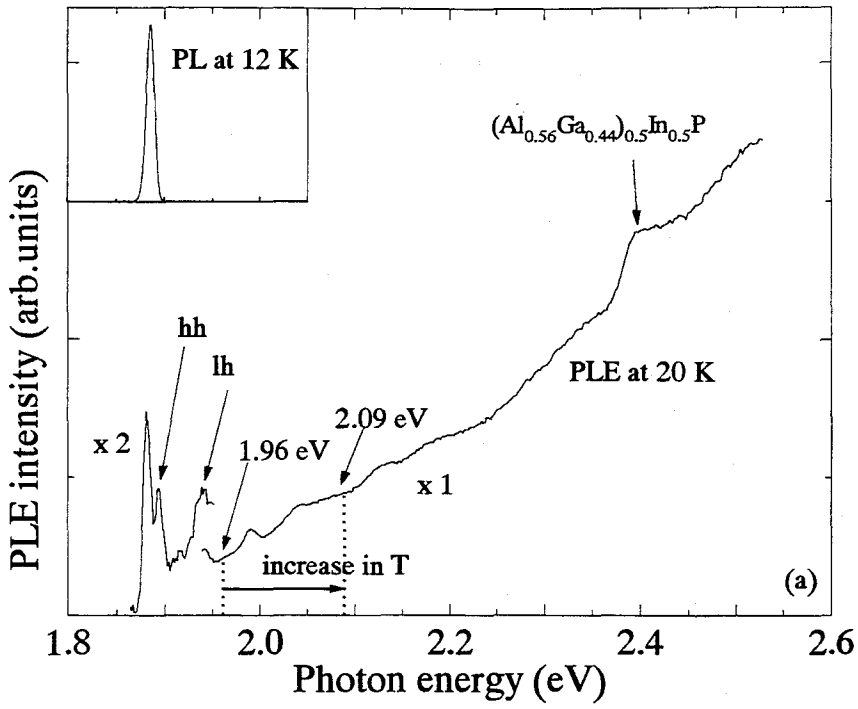
PL at 12 K
$(Al_{0.56}Ga_{0.44})_{0.5}In_{0.5}P$
PLE at 20 K
hh
lh
2.09 eV
1.96 eV
x 2
x 1
increase in T
(a)
PLE intensity (arb.units)
1.8
2.0
2.2
2.4
2.6
Photon energy (eV)

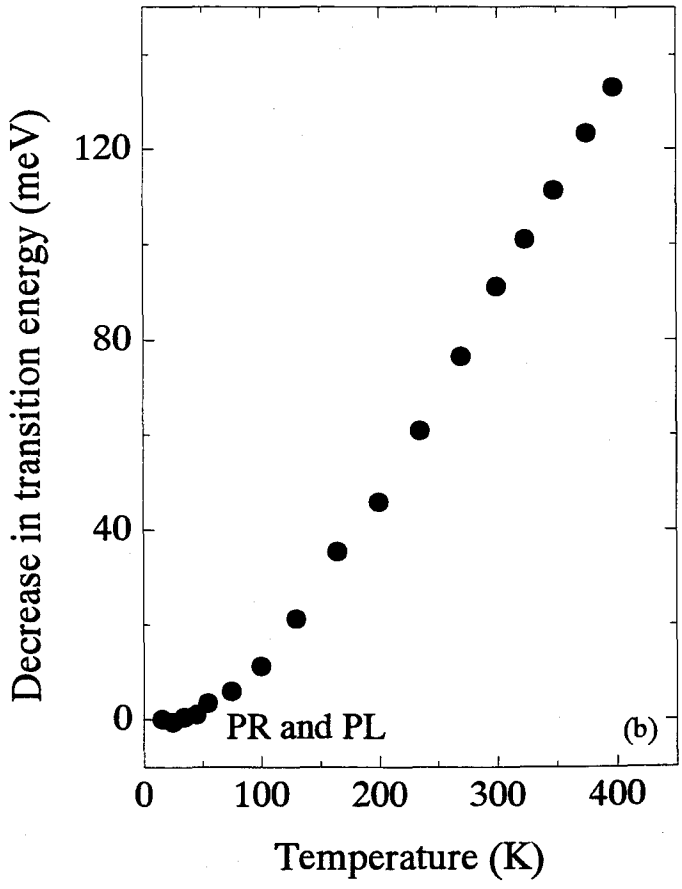
Decrease in transition energy (meV)
120
80
40
0
PR and PL
(b)
0
100
200
300
400
Temperature (K)

Fig. 7.3

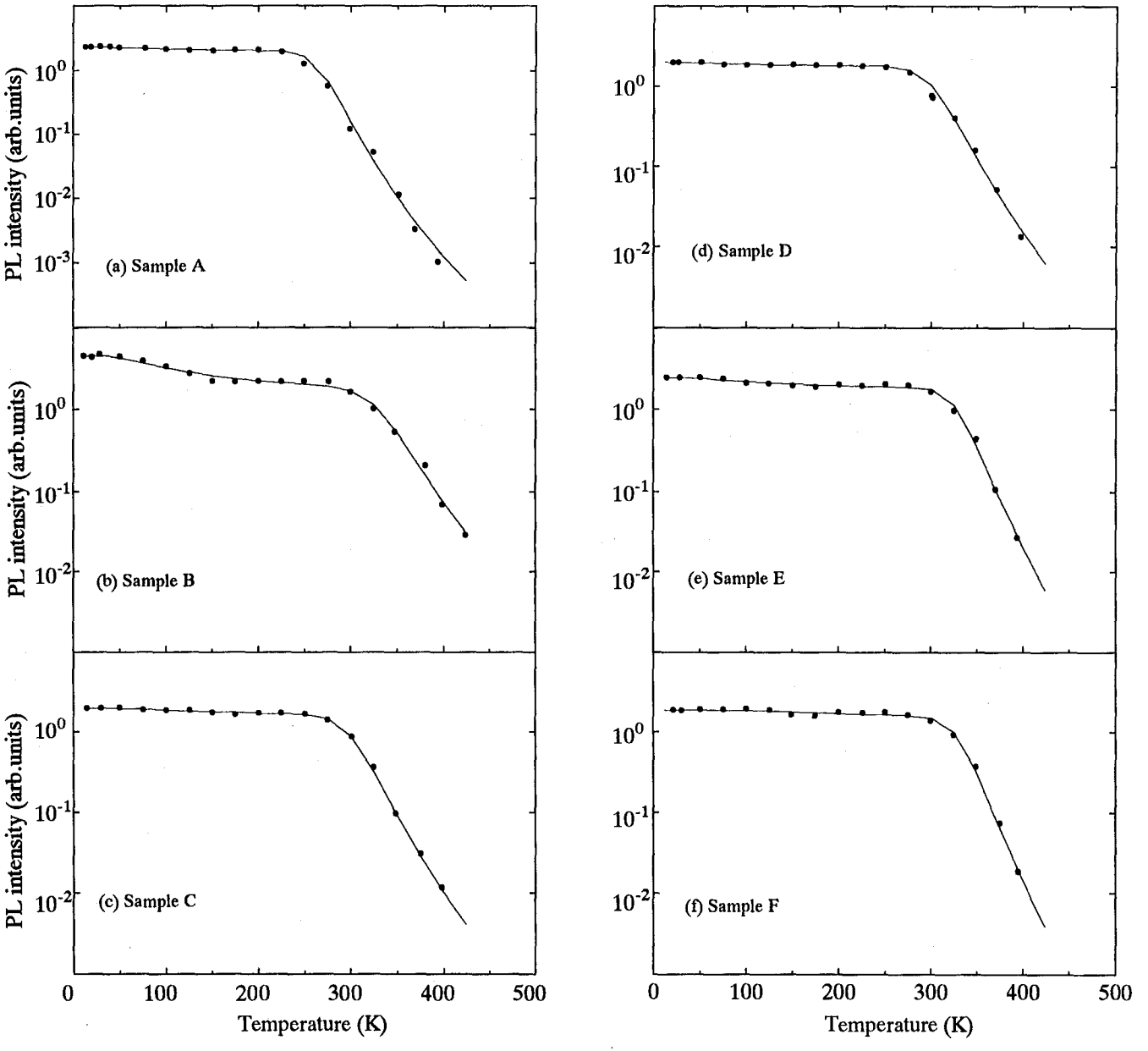
PL intensity (arb.units)
(a) Sample A
(b) Sample B
(c) Sample C
(d) Sample D
(e) Sample E
(f) Sample F
Temperature (K)
0
100
200
300
400
500

Fig. 7.4

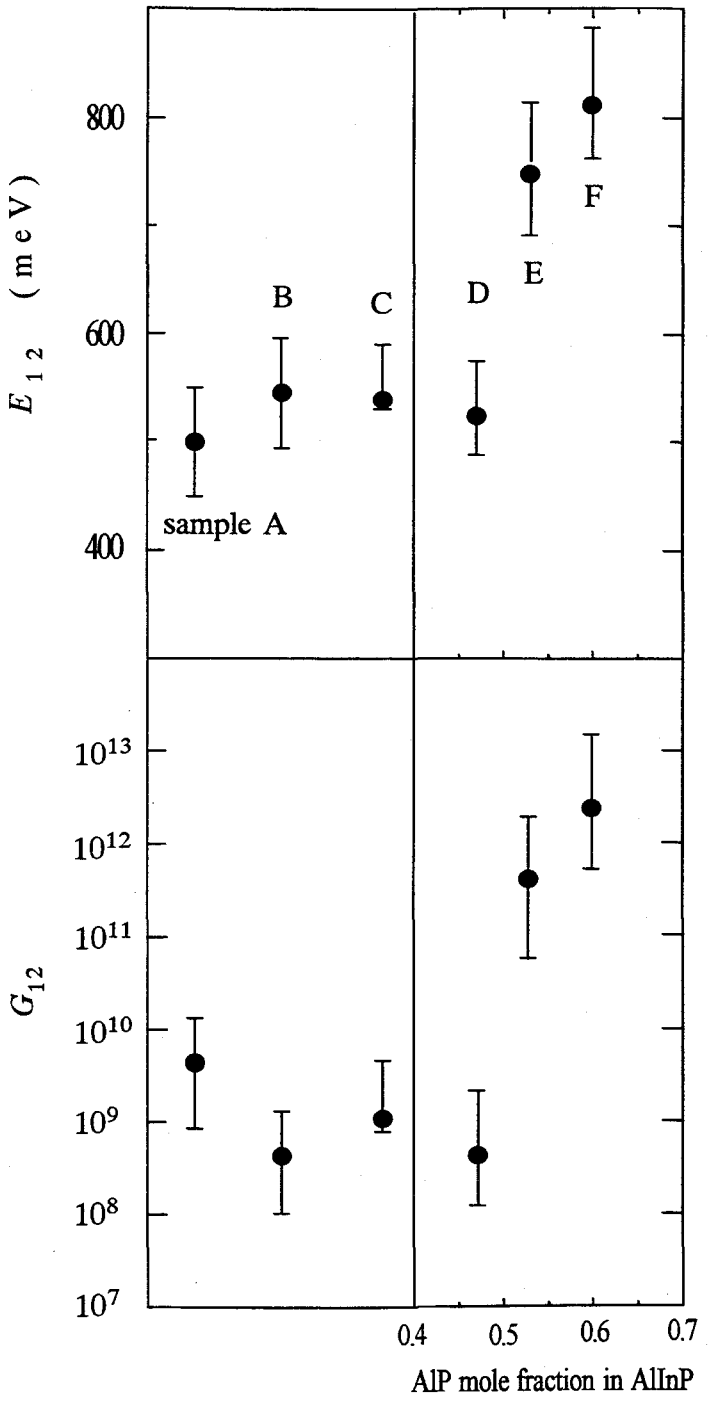
800
600
400
E_{12} (meV)
sample A
B
C
D
E
F
10^{13}
10^{12}
10^{11}
10^{10}
10^{9}
10^{8}
10^{7}
G_{12}
0.4
0.5
0.6
0.7
AlP mole fraction in AlInP

Fig. 7.5

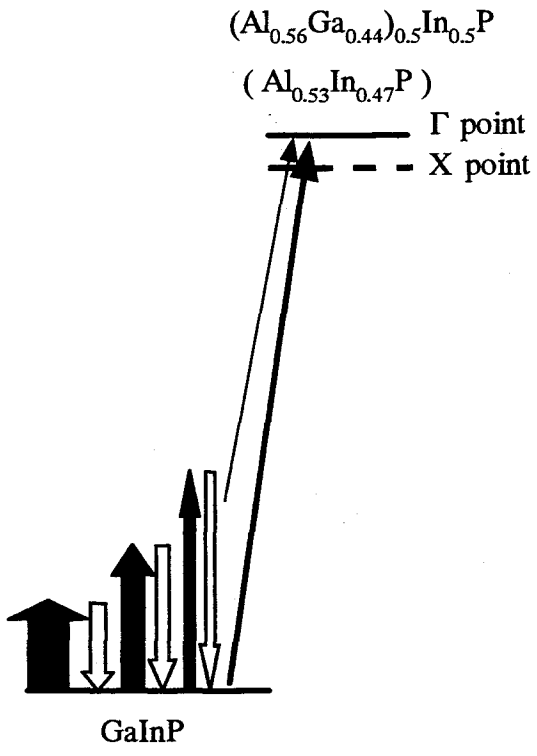

(a) Single-barrier structure

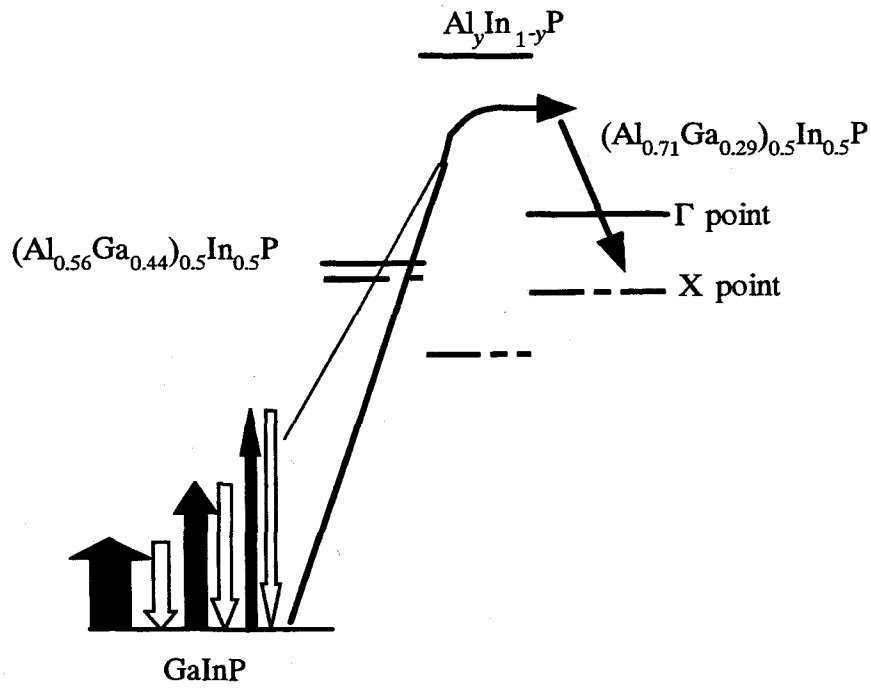

(b) Double-barrier structures

Fig. 7.6